

DESIGN STUDIES ON RF POWER COUPLERS FOR ACCELERATOR CAVITIES

By

Rajesh Kumar

(ENGG01200804017)

Bhabha Atomic Research Centre, Mumbai

A thesis submitted to the

Board of Studies in Engineering Sciences

In partial fulfillment of requirements

For the degree of

DOCTOR OF PHILOSOPHY

of

HOMI BHABHA NATIONAL INSTITUTE

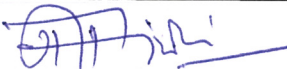
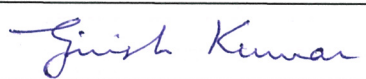
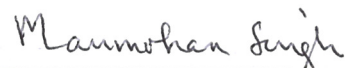
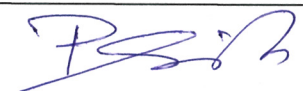

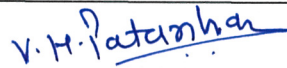




October 2015

Homi Bhabha National Institute

Recommendations of the Viva Voce Board

As members of the Viva-Voce Board, we certify that we have read the dissertation prepared by Mr. Rajesh Kumar entitled “**Design Studies on RF Power Couplers for Accelerator Cavities**” and recommend that it may be accepted as fulfilling the dissertation requirement for the Degree of Doctor of Philosophy.

		Signature	Date
Chairman –	Dr. A. P. Tiwari		20.10.15
Guide-	Prof. Girish Kumar		20.10.2015
Co-Guide-	Dr. M .S. Bhatia		20.10.2015
Tech. Advisor-	Dr. P. Singh		20.10.2015
Member 1-	Dr. A.K. Bhattacharjee		20.10.15
Member 2-	Dr. V.H. Patankar		20.10.2015
Member 3-	Dr. D.C. Kar		20.10.15
Member 4-	Prof. A.R. Harish		20 Oct 2015

Final approval and acceptance of this dissertation is contingent upon the candidate's submission of the final copies of the dissertation to HBNI.

I hereby certify that I have read this dissertation prepared under my direction and recommend that it may be accepted as fulfilling the dissertation requirement.

Date: 20.10.2015

Place: BARC, Mumbai


Guide/Convener

STATEMENT BY THE AUTHOR

This dissertation has been submitted in partial fulfilment of requirements for an advanced degree at Homi Bhabha National Institute (HBNI) and is deposited in the Library to be made available to borrowers under rules of the HBNI. Brief quotations from this dissertation are allowable without special permission, provided that accurate acknowledgement of source is made. Requests for permission for extended quotation from or reproduction of this manuscript in whole or in part may be granted by the Competent Authority of HBNI when in his or her judgment the proposed use of the material is in the interests of scholarship. In all other instances, however, permission must be obtained from the author.

Rajesh Kumar

DECLARATION

I, hereby declare that the investigation presented in the thesis has been carried out by me.
The work is original and has not been submitted earlier as a whole or in part for a degree /
diploma at this or any other Institution / University.

Rajesh Kumar

List of Publications arising from the thesis

Journal Publications:

1. Rajesh Kumar, “**A novel method for variable coupling using iris rotation in RF couplers**”, *Nuclear Instruments and Methods in Physics Research A*, Vol. 600, 534-537 (2009)
2. Rajesh Kumar, P.Singh, Divya Unnikrishanan and Girish Kumar, “**A tunable waveguide to cavity coupler for high power accelerator cavities**”, *Nuclear Instruments and Methods in Physics Research A*, Vol. 664, 203-213 (2012)
3. Rajesh Kumar, P. Singh, M.S Bhatia and Girish Kumar, “**Analytical Method for coupling calculations of rotated iris coupled resonator cavity**”, *Progress In Electromagnetics Research B*, Vol. 44, 223-239 (2012)
4. Rajesh Kumar, P. Singh, Pratigya Mathur and Girish Kumar, “**Comparative electromagnetic analysis of ridge waveguide couplers for accelerator cavities**”, *Nuclear Instruments and Methods in Physics Research A*, Vol. 736, 99-106 (2014)
5. SVLS Rao, Piyush Jain, Rajni Pande, Shweta Roy, Jose Mathew, Rajesh Kumar, Manjiri Pande, S. Krishnagopal and P. Singh, “**Design, development and acceleration trials of radio-frequency quadrupole**”, *Review of Scientific Instruments*, Vol. 85, No. 4, (2014)

Conference Publications:

1. Rajesh Kumar, P. Jain, S.V.L.S Rao, Manish Kumar, P.K Biswas, S.B Jawale and P.Singh, “**High power RF Coupler development for LEHIPA**”, *Indian Particle accelerator conference (INPAC-2009), -RRCAT-Indore Jan.-2009*
2. Rajesh Kumar, G.N Singh and P Singh, “**Development of 350 MHz quarter wave coaxial resonator for power coupler testing**”, *IEEE Applied Electromagnetic conference –IEEE-AEMC09 Dec 14-16-2009, Kolkata, India*
3. Rajesh Kumar, P. Singh and L.M. Joshi, “**Development of under-cut type RF window for 50 kW Power coupler**”, *IEEE Applied Electromagnetic conference – IEEE-AEMC11, Dec 18-21, 2011 Kolkata, India*

4. Rajesh Kumar and P. Singh, “**Coupled RF-Thermal analysis of high power couplers for accelerator cavities**”, *COMSOL Conference, Oct. 17-18, Bangalore, India*
5. G. Kumar, P. Mathur, G. Joshi, R. Kumar and B V Ramarao, "**Design and Development of RF Components for Linear Accelerators**", *National Symp. on Nuclear Instrumentation (NSNI), Mumbai, pp. 4-5, Nov. 2013*
6. Shrikrishna Gupta, SVLS Rao, Rajesh Kumar, Piyush Jain, Jose Mathew, Jose Mentos, Sandeep Shrotriya, Sonal Sharma, Niranjana Patel, Shweta Roy, Rajni Pande, Arindam Basu, S.K Singh, Arun Agarwal, Manjiri Pande, S. Krishnagopal and P. Singh , “**RF Conditioning and beam experiments on 400 keV RFQ Accelerator at BARC**”, *IEEE XXVI Int. Symp. on Discharges and Electrical Insulation in vacuum, Sep. 28-Oct. 3, 2014, Mumbai, India*

Rajesh Kumar

DEDICATIONS

Dedicated to my parents

ACKNOWLEDGEMENTS

I hereby acknowledge the encouragement and excellent guidance received from my Guide Prof. Girish Kumar, Co-Guide Prof. M.S. Bhatia and Technology Advisor Dr. P. Singh. I am thankful to my doctoral committee chairman Dr. A.P. Tiwari and members Dr. S.V.G. Ravindranath and Dr. A.K. Bhattacharjee for their useful suggestions and motivation during this work. I also acknowledge the kind help from Dr. L.M. Joshi from CEERI Pilani in coaxial coupler development. I am thankful to Dr. S.R. Jain, BARC for encouraging me towards research work. Thanks are also due to Shri G.N. Singh, Shri. Montes Jose, Shri Arun Agarwal, Dr. S.V.L.S. Rao and other colleagues at IADD, BARC for their involvement in different aspects of coupler development. I also thank the reviewers for their useful suggestions. I am thankful to Shri. P.V. Bhagwat, Head IADD for his keen interest in the work. This work would not have been possible without the love and support from my wife Vandana, and son Arnav. I am also fortunate to have blessings of my parents and other family members. I am deeply grateful to BARC for providing me the opportunity to carry out my research work.

Table of contents

Abstract.....	xi
List of Abbreviations	xii
List of Symbols	xv
List of Figures	xvi
List of Tables	xxvi

CHAPTERS	Page no.
1. Introduction	01
1.1 Coaxial and waveguide couplers	03
1.2 Electric and magnetic field coupling	05
1.3 Superconducting and warm RF couplers	06
1.4 Equivalent circuit for coupler cavity system	07
1.5 Coupling coefficient of coupler cavity system	10
1.6 Coupling coefficient measurements.....	12
1.7 Literature Survey	12
1.8 Organization of thesis.....	21

2. Design procedure for high power RF couplers	22
2.1 Introduction	22
2.2 External Q calculations	22
2.2.1 External Q calculations from Pascal Balleyguier technique	24
2.2.2 External Q calculations from CST Microwave Studio.	24
2.3 EM field distribution inside coupler.	25
2.4 Cavity frequency and field perturbation.	26
2.5 RF Loss calculations and thermal analysis	28
2.6 Multipacting analysis	31
2.7 Fabrication and testing aspects.	32
2.8 Summary	34
3. Coupling variation by iris rotation in RF couplers	35
3.1 Introduction	35
3.2 EM simulations for rotated iris coupled cavity	35
3.2.1 Simulation model and scaling procedure	37
3.2.2 Coupling coefficient variation with iris length.	38
3.2.3 Coupling coefficient variation with iris width.	40
3.2.4 Scaling of coupling coefficient with different iris sizes	40
3.3 Proposed technique for tuning of coupling coefficient	43
3.4 Analytical expressions, prototyping and RF measurements	44
3.4.1 Theory of coupling calculations for rotated iris	47
3.4.1.1 Magnetic polarizability of oriented iris.	48
3.4.1.2 Analytical expressions for External Q.	50
3.4.1.3 Special Cases.	56
3.4.2 EM design of rotated iris and S band cavity.	59
3.4.3 Measurements for External Q and coupling.	64
3.4.4 Practical aspects of rotated iris coupler	66
3.4.4.1 Increasing the coupling for given iris depth.	66
3.4.4.2 RF losses and resonant frequency variation.	70

3.4.4.3 EM fields in rotatable iris.....	72
3.5 Summary	75
4. High power ridge waveguide couplers	77
4.1 Introduction	77
4.2 Description of ridge waveguide coupler	78
4.2.1 EM simulations of quarter wave matching section	79
4.2.2 Dependence of return loss on dimensional tolerances	81
4.3 Proposed tuning scheme for ridge waveguide couplers	85
4.4 Tuner optimization for coupler dimension errors	89
4.5 Tuner studies on iris coupler with cavity coupling	98
4.5.1 Tuning studies for individual coupler dimensions	101
4.5.2 Studies for dimensional errors on all coupler dimensions.....	102
4.6 Comparison with tapered ridge waveguide coupler	104
4.6.1 Introduction	104
4.6.2 Comparative analysis of waveguide transitions	104
4.6.2.1 Studies for return loss and frequency variation.....	107
4.6.2.2 Dimensional variations on all coupler dimensions.....	112
4.6.2.3 Transmission phase and insertion loss.....	113
4.6.3 Comparison of return loss bandwidth.....	115
4.6.4 Electric and magnetic field distributions.....	115
4.6.5 Comparison of multipacting behavior	116
4.6.6 Conclusions for comparative analysis	120
4.7 Prototyping and RF characterization of straight ridge coupler.....	120
4.7.1 Introduction	120
4.7.2 Studies on the EM field and Return loss	121
4.7.3 Fabrication and RF measurements	125
4.8 Thermal aspects of Coupler design.....	131
4.9 Summary.....	132
5. Development of coaxial RF couplers and RF test bench	134
5.1 Introduction	134

5.2 Coaxial coupler with under-cut type window	135
5.2.1 Existing coaxial window designs	135
5.2.2 Proposed coaxial window design	136
5.2.2.1 Electromagnetic design of RF window.....	136
5.2.2.2 Fabrication and vacuum testing.....	139
5.3 Coaxial coupler with stub loading.....	141
5.4 Test cavity design.....	143
5.4.1 Theory of couplers connected to a cavity.....	143
5.4.2 Electromagnetic design of cavity	145
5.4.3 RF measurements on a fabricated cavity.....	148
5.4.3.1 Measurements with 15 mm end gap.....	148
5.4.3.2 Tuning of the cavity with end tuners.....	150
5.5 High power conditioning of couplers.....	151
5.6 Summary	157
6. Conclusions and Future directions	158
6.1 Conclusions	158
6.2 Future directions.....	160
References	161

Abstract

RF power couplers are one of the most important parts of RF based particle accelerators as they need to couple RF power from the amplifier to the cavity without any reflections. The coupler and iris dimensions are important in obtaining the desired coupling. It is difficult to tune the coupling coefficient in waveguide couplers as compared to coaxial loop or probe couplers. The conventional tuning techniques using three stub tuners or EH tuners are not preferred at high powers because they result in standing waves over a larger section of line as additional tuning component in RF line is required. The tuning in such couplers is generally done by post fabrication iris machining.

In order to overcome this problem, a novel tuning scheme based upon iris rotation is proposed for waveguide-cavity couplers. The proposed analytical expressions for coupling calculations agree well with full wave simulations and measurements.

A detailed analysis of straight ridge coupler is carried out and tuners are proposed to relax the dimensional tolerances. These tuners can also be used for coupling tuning.

Though, the straight ridge and tapered ridge waveguide coupler designs have been used in accelerator cavities, a comparison of these designs is not available. Hence, a tapered ridge waveguide coupler is optimized and compared with straight ridge waveguide.

As the coaxial couplers provide the flexibility of coupling tuning, two coaxial loop coupler assemblies with under-cut window and stub loaded window are designed and developed for 50 kW, 350 MHz applications for their use in cavity conditioning and beam acceleration from RFQ cavity. A test cavity is also developed for RF conditioning of these couplers.

List of Abbreviations

ADS	Accelerator Driven System
APAC	Asian Particle Accelerator Conference
APT	Accelerator Production of Tritium
BARC	Bhabha Atomic Research Centre
CERN	European Organization for Nuclear Research
CESR	Cornell Electron-positron Storage Ring
CSNS	China Spallation Neutron Source
CST-MWS	Computer Simulation Technologies- Microwave Studio
DTL	Drift Tube Linac
EPAC	European Particle Accelerator Conference
ERL	Energy Recovery Linac
ETP	Electronic Tough Pitch
FEL	Free Electron Laser
FEM	Finite Element Method
HERA	Hadron Electron Ring Accelerator
IPAC	International Particle Accelerator Conference

IPHI	French High Intensity Proton Injector
KOMAC	Korea Multi- Purpose Accelerator Complex
LEDA	Low Energy Demonstration Accelerator
LEHIPA	Low Energy High Intensity Proton Accelerator
LEP	Large Electron Positron Collider
LHC	Large Hadron Collider
LINAC	Linear Accelerator
NC	Normal Conducting
OFE	Oxygen Free Electronic
PAC	Particle Accelerator Conference
PEFP	Proton Engineering Frontier Project
PEP	Positron Electron Project
RF	Radio Frequency
RFQ	Radio Frequency Quadrupole
SC	Super Condcuting
SNS	Spallation Neutron Source
SW	Standing Wave

TRASCO	TRAsmutazione di SCORie
TRISTAN	Transposable Ring Intersecting Storage Accelerator in Nippon
VNA	Vector Network Analyzer

List of Symbols

α	Attenuation constant
β	Coupling coefficient
Γ	Reflection coefficient
λ	Wavelength
\mathbf{E}	Electric field intensity *
\mathbf{H}	Magnetic field intensity*
k_o	Free space propagation constant
Q_{ext}	External quality factor
Q_o	Intrinsic quality factor
Z_o	Characteristic impedance

* \mathbf{E} and \mathbf{H} fields are vector fields represented as complex vectors where sinusoidal time dependence ($e^{j\omega t}$) is implied. E and H (non bold face) representation is used for the magnitude of complex vector fields.

List of Figures

Fig. 1.1	Design choices for RF couplers	04
Fig. 1.2	Schematic of (a) probe coupled cavity with coaxial input; (b) loop coupled Cavity with coaxial input; (c) probe coupled cavity with waveguide input and (d) iris coupled cavity with waveguide.....	05
Fig. 1.3	Evolution of EM fields in (a) end iris coupled cavity and (b) in side coupled cavity.....	06
Fig. 1.4	Evolution of EM fields in (a) probe coupled cavity and (b) in loop coupled cavity.....	07
Fig. 1.5	Coupling coefficient tuning techniques in waveguide and coaxial couplers.....	14
Fig. 1.6	Different window designs for (a) coaxial and (b) waveguide geometry along with a choke type window.....	18
Fig. 1.7	Typical waveguide to coaxial transition based coupler for (a) room temperature cavity and (b) for SC cavity.....	19
Fig. 1.8	Waveguide to coaxial type couplers connected to test cavity for RF conditioning.....	20
Fig. 2.1	A cavity connected to (a) open ended and (b) a shorted waveguide.....	23
Fig. 2.2	CST- MWS model of (1/4 th) RFQ connected to ridge waveguide.....	25

Fig. 2.3	Simulated coupling coefficient of RFQ to ridge waveguide coupling through a rectangular iris	25
Fig. 2.4	Plot of (a) E field in ridge waveguide and (b) view of meshing near the rounded corners.....	27
Fig. 2.5	Schematic view of coaxial coupler with thermal straps at 15 K and 125 K.....	30
Fig. 2.6	Simulations of temperature variation along the coupler for different 15 K thermal strap positions.....	30
Fig. 2.7	View of (a) location of initial electrons and (b) simulated electron trajectories inside ridge waveguide	33
Fig. 2.8	Coaxial coupler parts (a) before brazing and (b) after brazing	34
Fig. 3.1	Schematic of iris coupled cavity.....	36
Fig. 3.2	Cross-section view of rectangular waveguide and iris.....	38
Fig. 3.3	Simulation model of waveguide to cavity coupled system.....	38
Fig. 3.4	Variation of coupling coefficient with length of iris (width= 10 cm).....	39
Fig. 3.5	Variation of coupling coefficient (a) with width of iris (length = 20 cm).....	39
Fig. 3.6	Variation of coupling coefficient with iris width for different iris lengths.....	40
Fig. 3.7	Variation of coupling coefficient with width of iris (length = 10 cm).....	42

Fig. 3.8	Cross section of iris in two different positions of 0 degree and 45 degrees.....	42
Fig. 3.9	Coupling coefficient variation with iris rotation for iris of size $l = 20$ cm and $w = 10$ cm.....	44
Fig. 3.10	Coupling coefficient variation with iris rotation for iris of size $l = 10$ cm and $w = 10$ cm	45
Fig. 3.11	Schematic of iris coupled waveguide-cavity system.....	48
Fig. 3.12	Cross-section of incoming waveguide and rotated iris (in x-y and u-v coordinate system respectively).....	49
Fig. 3.13	Magnetic field and iris orientation for (a) longitudinal polarizability and (b) transverse polarizability	50
Fig. 3.14	Cut-view of simulation model for iris coupled cavity	58
Fig. 3.15	Simulated arrow plots of (a) Electric field and (b) Magnetic field in the rotated iris.....	60
Fig. 3.16	CST simulation results for (a) External Q (b) coupling coefficient for different iris shapes.....	62
Fig. 3.17	Comparison of CST simulation results with theoretically calculated values for different iris shapes	63

Fig. 3.18	The pictures of (a) Iris cylinder with rectangular iris and (b) cavity connected to VNA through WR340- N Type adapter and auxiliary port for transmission measurements	64
Fig. 3.19	Variation of (a) External Q (b) coupling coefficient of simulated, measured, and proposed analytical results for different rotation angle of rectangular iris	67
Fig. 3.20	Iris shapes considered (a) rectangular iris; (b) dog-bone shaped iris and (c) rectangular ridge type iris	68
Fig. 3.21	Coupling coefficient variation for (a) rectangular ridge and dog-bone shaped iris and (b) for rectangular iris	70
Fig. 3.22	RF loss and cavity resonant frequency variation with iris length of rectangular iris	71
Fig. 3.23	Variation of RF losses and resonant frequency with iris rotation for different iris shapes.....	72
Fig. 3.24	Electric field in the (a) rotated iris without corner rounding and (b) Magnetic field in the rotated iris without corner rounding	74
Fig. 4.1	Model of ridge waveguide coupler view from (a) WR2300 input port and (b) output ridge waveguide port	79
Fig. 4.2	Ridge waveguide coupler's (a) top view; (b) cross-section view; (c) 3D simulation model and (d) S_{11} parameters plot of coupler	80

Fig. 4.3	Plot of (a) return loss at design frequency and (b) minimum return loss frequency for end gap and central gap; (c) return loss for central section length, central ridge width, central overall width and height and (d) variation of minimum return loss frequency for central ridge dimensions.....	83
Fig. 4.4	Plot of (a) return loss at design frequency and (b) corresponding minimum return loss frequency	84
Fig. 4.5	Arrow plots of (a) Electric and (b) magnetic field on simulated coupler.....	86
Fig. 4.6	Simulation model for (a) two cylindrical tuners on central ridge waveguide section and (b) mesh view on cut-plane of simulation model	86
Fig. 4.7	Variation of (a) frequency of return loss minima and (b) S_{11} parameter at 352.2 MHz with tuner depth.....	88
Fig. 4.8	Tuning results for (a) Return loss and (b) frequency values for before and after tuning for end gap changes; (c) return loss and (d) frequency values for before and after tuning for central gap changes.....	91
Fig. 4.9	Tuning results for (a) return loss and (b) frequency values before and after tuning for Set 1 of dimensional changes; (c) return loss and (d) frequency values before and after tuning for Set 2 of dimensional changes	97
Fig. 4.10	RF Coupler connected to the pill box cavity through an iris.....	98

Fig. 4.11	Equivalent circuit of ridge waveguide coupler connected to a cavity	99
Fig. 4.12	Tuning results for (a) Q_{ext} with T_e Tuner movement up to the coupler surface; (b) Q_{ext} variation with T_e Tuner movement into the central gap from coupler surface; (c) Q_{ext} variation with T_m Tuner movement and (d) resonant frequency variation of coupled system with T_e and T_m Tuner movement.....	100
Fig. 4.13	Tapered ridge waveguide coupler's (a) top view and cross-sectional view; (b) CST MWS simulation model of coupler; (c) side view of coupler and (d) S_{11} parameters plot obtained from simulations for optimized geometry.....	105
Fig. 4.14	CST MWS simulation model of straight coupler and (b) simulation model of tapered coupler with meshing.....	107
Fig. 4.15	Plots of (a) return loss at design frequency (of 352.2 MHz) with end gap changes and (b) frequency variation corresponding minimum return loss.....	108
Fig. 4.16	Plots of (a) return loss at design frequency (of 352.2 MHz) with central gap changes and (b) frequency variation corresponding minimum return loss.....	109
Fig. 4.17	Plots of (a) return loss at design frequency (of 352.2 MHz) with central ridge width changes and (b) frequency variation corresponding to minimum return loss.....	110
Fig. 4.18	Plots of (a) return loss at design frequency (of 352.2 MHz) with central ridge length changes and (b) frequency variation corresponding minimum return loss.....	110

Fig. 4.19	Plots of (a) return loss at design frequency (of 352.2 MHz) with WR 2300 width changes and (b) frequency variation corresponding minimum return loss	111
Fig. 4.20	Plots of (a) return loss at design frequency (of 352.2 MHz) with WR 2300 height changes and (b) frequency variation corresponding minimum return loss.....	112
Fig. 4.21	Transmission phase plots (a) at design frequency with end gap changes and (b) corresponding variation of transmission phase with central gap changes ...	114
Fig. 4.22	Transmission phase at design frequency for central ridge length changes.....	114
Fig. 4.23	Return loss plots for straight ridge coupler and tapered ridge coupler	116
Fig. 4.24	Simulated arrow plots of (a) electric field and (b) magnetic field for tapered ridge coupler.....	117
Fig. 4.25	Variation of (a) electric field (V/m) and (b) magnetic field intensity (A/m) along the coupler length for tapered and straight ridge coupler	118
Fig. 4.26	Schematic of two couplers connected for RF measurements.....	121
Fig. 4.27	CST-MWS model of (a) couplers connected to each other and (b) S parameter plots for the couplers	122
Fig. 4.28	Field plots along the center line of couplers for (a) electric field at frequencies of minimum return loss and at desired frequency of 352.2 MHz and (b) corresponding plots for magnetic field along the length.....	123
Fig. 4.29	S parameter plots for ridge transitions connected back to back	124

Fig. 4.30	EM field magnitude plots before and after tuning for (a) electric field (V/m) at 352.2 MHz and (b) corresponding magnetic field in A/m along length.....	125
Fig. 4.31	Ridge waveguide transitions (a) viewed from input and output end and (b) transitions connected to network analyzer with WR2300 to N type adapters	127
Fig. 4.32	Simulations and measurements for (a) effect of tuner ‘Te ₁ ’ movement on first return loss minima frequency ‘f ₁ ’ and (b) effect of tuner ‘Te ₁ ’ movement on second return loss minima frequency ‘f ₂ ’	127
Fig. 4.33	Return loss plots obtained with VNA for (a) before tuning and (b) after tuning.....	129
Fig. 4.34	Temperature distribution on end ridge waveguide with uniform cooling on outer surfaces.....	131
Fig. 4.35	Temperature distribution on complete couple assembly.....	132
Fig. 5.1	Cut view of simulation model showing chokes on inner conductor	136
Fig. 5.2	Cut view of simulation model with cuts on inner conductor	137
Fig. 5.3	S parameters of RF window after matching under-cut on inner conductor.....	137
Fig. 5.4	Temperature profile on the coupler for 10 kW input power.....	138
Fig. 5.5	Cut view of CST model for External Q simulation	139

Fig. 5.6	View of (a) RF window and coupler from input side and (b) Loop coupler placed vertically	140
Fig. 5.7	RF window and coupler connected to test cavity for vacuum leak checking ...	140
Fig. 5.8	CST Microwave Studio model of (a) coaxial stub loaded coupler; (b) cut view of the coupler assembly; (c) simulated return loss and transmission loss of the optimized coupler geometry and (d) variation of return loss with stub length...	142
Fig. 5.9	Different coupler parts brazed separately and (b) Complete coupler assembly after brazing.....	143
Fig. 5.10	Schematic of coupler test bench	144
Fig. 5.11	Cut view of simulation model showing inner conductor and loop couplers	146
Fig. 5.12	Electric field plot on a cut section of the cavity	148
Fig. 5.13	Fabricated quarter wave resonator connected to VNA for RF measurements	149
Fig. 5.14	Simulated and measured values of resonance frequency with tuner outward movement	151
Fig. 5.15	Return loss measurements on coupler connected to the cavity	152
Fig. 5.16	RF Coupler and window assembly being tested up-to 3.5 kW.....	154
Fig. 5.17	RF conditioning of couplers at 50 kW peak power with 1% duty cycle.....	155

Fig. 5.18	RF Coupler connected to the RFQ cavity for beam experiments	157
------------------	---	-----

List of Tables

Table 1.1	List of high RF Power couplers for various accelerator facilities.....	16
Table 1.2	List of RF Power couplers for room temperature accelerators	17
Table 2.1	Convergence of Peak electric field with mesh size	28
Table 3.1	Variation of coupling coefficient, RF loss, E and H fields for different iris shapes.....	73
Table 4.1	Dimensions of optimized coupler parameters	81
Table 4.2	Tuning results for return loss and frequency with end gap variation	92
Table 4.3	Tuning results for return loss and frequency with central ridge gap variation	93
Table 4.4	Details of dimensional variations on all coupler dimensions (Set 1)	94
Table 4.5	Details of dimensional variations on all coupler dimensions (Set 2)	95
Table 4.6	Tuning details for dimensional variations on all coupler dimensions	96
Table 4.7	Tuning details for end gap dimensional shifts	102
Table 4.8	Tuning details for central gap dimensional shifts	102
Table 4.9	Q_{ext} Tuning results for coupled system.....	103

Table 4.10 Dimensions of the optimized tapered and straight ridge transitions106

Table 4.11 Comparison for dimensional changes on all coupler dimensions
.....113

Table 4.12 Comparison of multipacting power levels119

Table 4.13 Dimensions and tolerances of fabricated couplers.....126

Table 4.14 Summary of simulated and measured values of frequency, return loss and tuner
depth130

Table 5.1 Dimensions of quarter wave test cavity147

Table 5.2 Measured and simulated results for different end gaps of quarter wave test
cavity.....149

CHAPTER-1

INTRODUCTION

Charged particle accelerators with increasing energies have been used as a probe to investigate the atomic nucleus and elementary particles. These accelerators utilize high electric fields to accelerate the charge particles. They have evolved from early twentieth century Cockroft Walton and Van de Graaff DC accelerators to RF linear accelerators (RF Linacs), cyclotrons, synchrotrons and to the modern day collider rings. The evolution of these accelerator topologies have been governed by the requirement of highest achievable particle energy with minimum space requirements. Particle accelerators (like protons, electrons or ions) find applications in fundamental nuclear research as well as in industrial, agriculture and medical fields. Some examples are sterilization, food preservation, isotope production and radio therapy. Apart from this, several high current proton accelerator projects for various applications like Accelerator Driven system (ADS) and Spallation Neutron Source (SNS) are under design and development worldwide.

Radio Frequency (RF) based charged particle accelerators are being used for high energy acceleration because DC accelerators have practical limitations beyond 25 MV. RF based accelerators can be linear or circular type. In linear RF accelerators, multiple sections of enclosed metallic structures (i.e. RF cavity or resonator) are connected to each other in linear fashion. In order to reduce the accelerator size, circular accelerators (like cyclotrons or synchrotrons) use magnetic field to keep accelerated particles in circular orbit. In superconducting RF cavities,

very high electric field gradients (> 30 MV/m) are possible. Because of this, the overall length of RF Linac becomes less for the given energy.

High current and high energy (>10 mA current and 1 GeV energy) proton accelerators are required for emerging applications like ADS and Spallation Neutron Sources. There are only few existing high current proton RF Linac facilities like LEDA [1] and SNS [2] which have been already demonstrated or are under operation worldwide. However, there are many ongoing proton accelerator projects like KOMAC [3], TRASCO [4], IPHI [5], Project X [6], LINAC 4 at CERN [7], Indian ADS [8], ESS [9], CSNS [10], etc.

RF particle accelerators use high frequency resonant cavities for particle acceleration. The required EM mode for particle acceleration is excited in the cavity by the RF Power Coupler, which couples the power from amplifier and waveguide system (generally TE_{10} mode) to the cavity mode (eg. TM_{010} mode). The RF coupler is designed for minimum power reflections because the reflected power can damage the high power amplifiers. Even if the amplifier is protected by a circulator, the reflected power ends up in the circulator load and is wasted. Moreover, the reflected power results in higher electric and magnetic fields on the RF transmission system.

RF power couplers are one of the most important parts of RF based particle accelerators as they need to couple the power from the amplifier to the cavity without any reflections. Though, modern day particle accelerators use superconducting cavities, their injector part (up to 20 MeV for a 1 GeV proton accelerator) still uses room temperature cavities. This is because beam bunching and shaping is done at low energies resulting in beam losses which are unacceptable to superconducting cavities. Also, at low energies, lower particle velocity requires

larger wavelength (i.e. lower RF frequency) to obtain practical gap lengths for particle acceleration. Hence, cavities like Radio Frequency Quadrupole (RFQ) or Drift Tube Linac (DTL) are used in low energy region. These cavities are room temperature cavities and require very high power. Waveguide couplers are suitable for coupling power to these cavities because of their high power handling capability.

RF coupler transforms the cavity impedance to source impedance and provides impedance matching. It also protects the cavity vacuum from air side of incoming RF transfer lines. RF coupler is a general term, which can include fundamental power couplers, higher order mode couplers, directional couplers or even power dividers. However, this thesis is focused on fundamental power couplers for room temperature (warm) accelerator cavities.

1.1 COAXIAL AND WAVEGUIDE COUPLERS

There are many possible coupler topologies as shown in Fig. 1.1. Couplers can be waveguide, coaxial or hybrid type i.e. waveguide to coaxial type. They can be further classified based upon type of coupling i.e. side wall iris or end wall iris type, loop type or probe type. RF window is a dielectric barrier which is generally made with high purity alumina disc or cylinder. RF window is generally integrated to coupler assemblies, though it can also be a stand-alone component. Schematics of various coupler topologies are shown in Fig. 1.2. RF window is integrated in coupler assembly except in Fig. 1.2(d), where it can be added as a stand-alone component. Depending on the input RF system, the power coupler can be either a waveguide type, coaxial type or hybrid type consisting of waveguide to coaxial transition. Waveguide type couplers can be further classified as end iris coupled [11] and side iris coupled [12]. Coaxial couplers can be either loop type or probe type.

All these coupler types provide either electric or magnetic coupling. The couplers are also distinguished on the basis of cavity temperature and conductivity i.e. superconducting or room temperature couplers. RF power couplers can feed power to standing wave or traveling wave cavities.

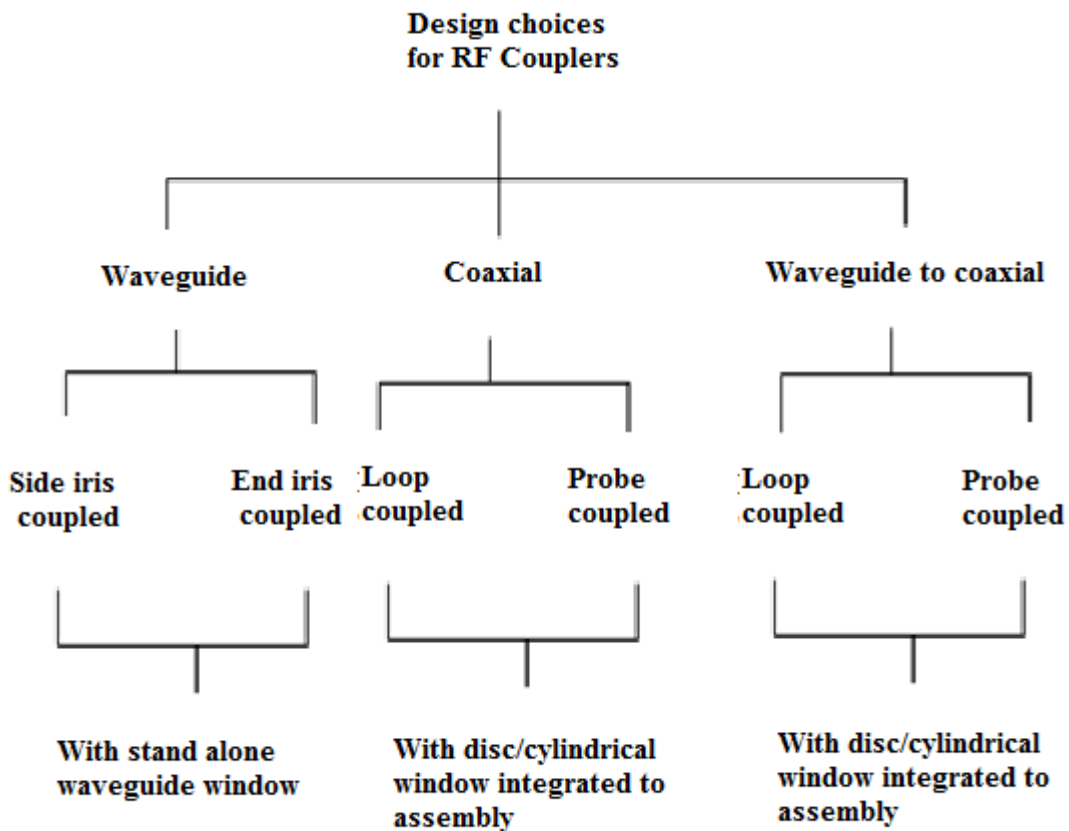


Fig. 1.1 Design choices for RF couplers.

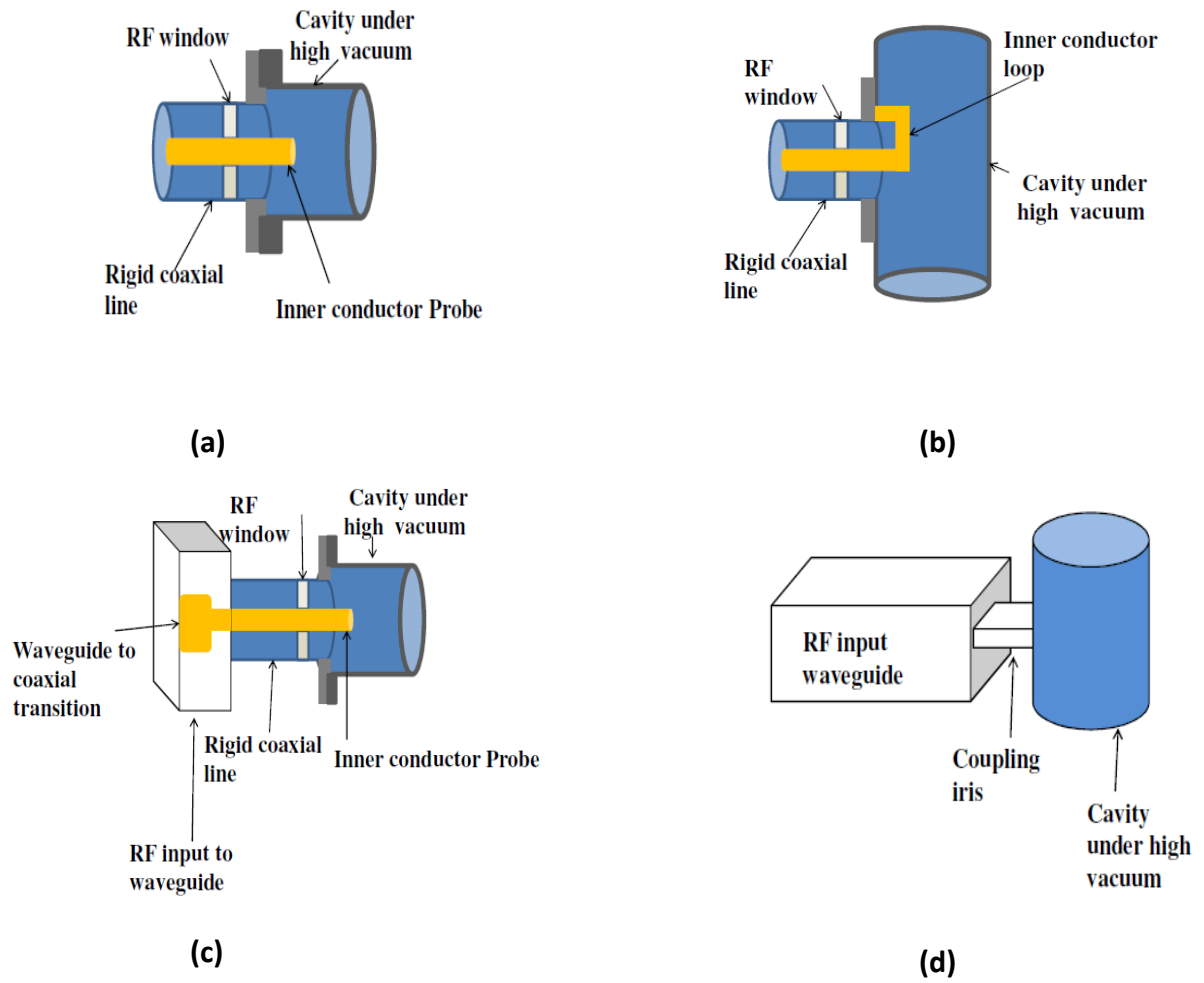


Fig. 1.2 Schematic of (a) probe coupled cavity with coaxial input; (b) loop coupled cavity with coaxial input; (c) probe coupled cavity with waveguide input and (d) iris coupled cavity with waveguide input.

1.2 ELECTRIC AND MAGNETIC COUPLING

An excellent description of different coupling topologies along with electric and magnetic field patterns is given in [13]. These are reproduced in Figs. 1.3 and 1.4. In Fig. 1.3(a), TE_{10} mode of incoming rectangular waveguide is coupled through an end wall iris to TM_{010} mode of cylindrical cavity. An iris in the side of wall of incoming waveguide is used in Fig. 1.3(b).

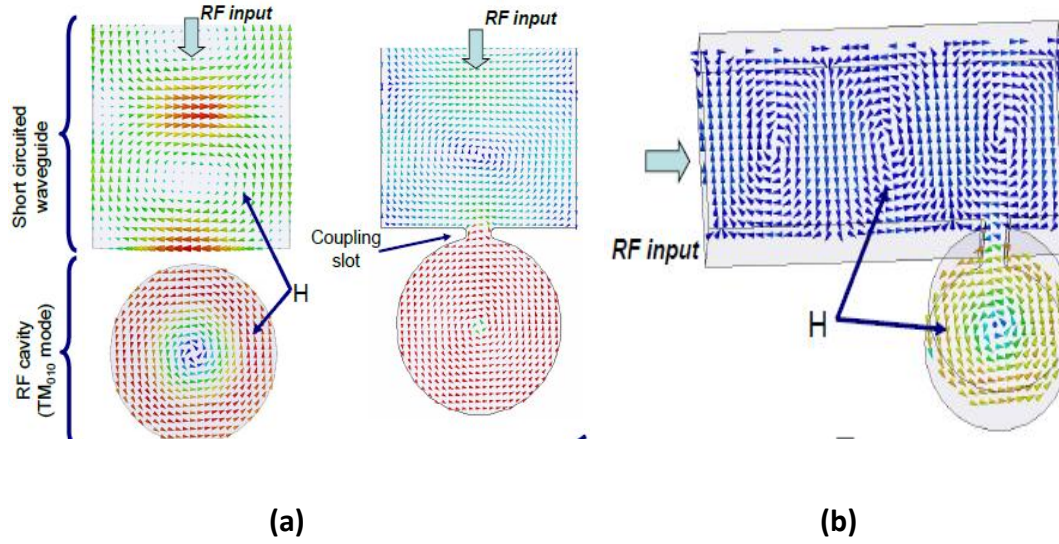


Fig. 1.3 Evolution of EM fields in (a) end iris coupled cavity and (b) side coupled cavity [13].

In Fig. 1.4, coupling from incoming coaxial line to TM_{010} mode of cavity is considered. The dimension of coupling iris, area of coupling loop and length of the probe determines the strength of coupling and is optimized during design stages.

1.3 SUPERCONDUCTING AND WARM RF COUPLERS

As the technology for superconducting (SC) cavities has sufficiently matured [14], many of the modern high energy proton RF Linac projects have opted for SC cavities. However, as discussed earlier, low energy injector part still consists of warm cavities. The injector part consists of RFQ cavities, which generally operate at room temperature. In modern accelerators like Project X [6], superconductivity will be introduced after 2.5 MeV. Hence, a lot of progress has taken place in the technology development of power couplers for both SC and warm or room temperature cavities.

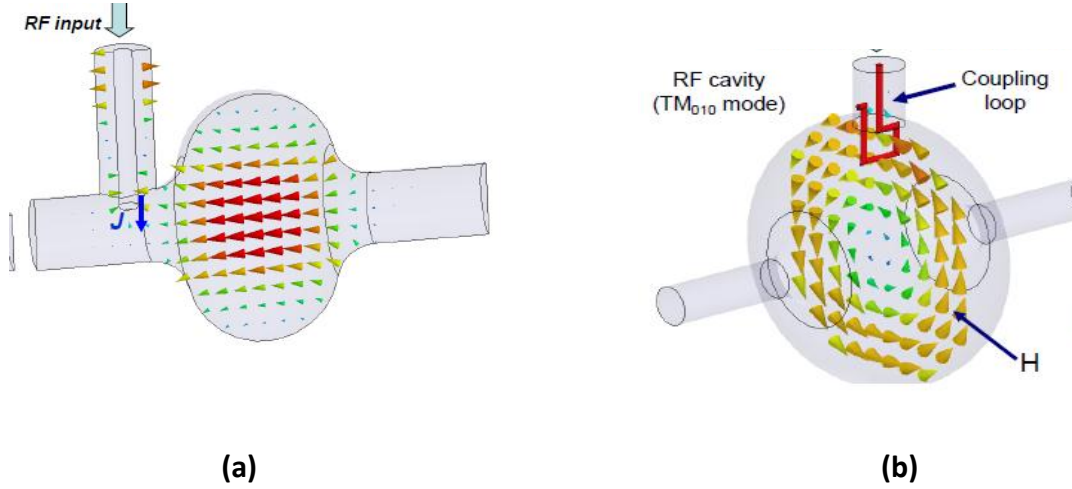


Fig. 1.4 Evolution of EM fields in (a) probe coupled cavity and (b) in loop coupled cavity [13].

The typical SC coupler assembly involves pumping port, windows, coupling adjustment mechanism, bias for multipacting suppression, view port and bellows. A typical waveguide to coaxial type coupler for a warm cavity involves cooling lines, a door knob transition and RF window. The SC couplers generally require more features like bellows, thermal straps, etc. as compared to warm couplers.

1.4 EQUIVALENT CIRCUIT FOR COUPLED CAVITY SYSTEM

The equivalent circuit of a cavity resonator can be represented as a parallel resonant circuit. The coupler acts as a transformer, which transforms or matches the resonator impedance to incoming RF line's characteristic impedance.

The transformer converts the cavity side impedance to an equivalent primary side impedance. If 'n' is the transformer turn ratio and 'R' is the cavity impedance at resonance, the input impedance ' Z_{in} ' at resonance will be:

$$Z_{in} = \frac{R}{n^2} \quad (1.1)$$

Coupling coefficient ' β ' is defined as the ratio of cavity impedance at resonance to the characteristic impedance of incoming line. It is given as:

$$\beta = \frac{Z_{in}}{Z_o} = \frac{R}{Z_o n^2} \quad (1.2)$$

A system is over-coupled if $\beta > 1$, critically coupled if $\beta = 1$ and under coupled if $\beta < 1$ [15].

The reflection coefficient ' Γ ' at coupler cavity interface is given as:

$$\Gamma = \frac{Z_{in} - Z_o}{Z_{in} + Z_o} \quad (1.3)$$

For a critically coupled cavity, the reflection coefficient is zero implying that no power is reflected.

Alternate definition of coupling coefficient is given as the ratio of intrinsic quality factor ' Q_o ' to the external quality factor ' Q_{ext} '. It can be written as:

$$\beta = \frac{Q_o}{Q_{ext}} \quad (1.4)$$

where, Q_o is given as:

$$Q_o = \omega_o \frac{U}{P_o} \quad (1.5)$$

The Q_{ext} is given as:

$$Q_{ext} = \omega_o \frac{U}{P_{rad}} \quad (1.6)$$

where ' ω_o ' is the resonance frequency in radians, ' U ' is energy stored in the cavity, ' P_o ' is the power dissipated in the cavity and ' P_{rad} ' is the power radiated from the cavity.

From eqns (1.4) to (1.6), coupling coefficient can be written as:

$$\beta = \frac{P_{rad}}{P_o} \quad (1.7)$$

In a beam loaded cavity, if 'P_b' is beam power and 'P_c' is cavity power, the cavity quality factor decreases because beam power also gets added to cavity loss. Hence, system is designed to be over-coupled without beam so that it becomes critically coupled with beam. The required optimal coupling for beam loaded cavity is given as [14,16]:

$$\beta_o = 1 + \frac{P_b}{P_c} \quad (1.8)$$

The optimum coupling coefficient definition is valid only if the generator frequency is equal to the resonator frequency. The detuning angle is used as a measure of frequency shift and is given as:

$$\tan\psi = -2Q_L\delta \quad (1.9a)$$

where 'ψ' is detuning angle, 'Q_L' is loaded quality factor and 'δ' is normalized frequency shift. The value of 'δ' is given as the ratio of frequency difference from the resonance (ω-ω_o) to the resonance frequency 'ω_o', i.e.

$$\delta = \frac{(\omega - \omega_o)}{\omega_o} \quad (1.9b)$$

It is important to detune the cavity by a certain optimum value so that it presents a real impedance i.e. its current and voltage are in phase. The beam current enters at synchronous phase 'Φ' w.r.t. cavity voltage. Because of this, cavity detuning is required to get real impedance (or minimum reflection) even at optimum coupling value given in eqn. (1.8). The required detuning is given as [16]:

$$\tan\psi = -\frac{(\beta_o-1)}{\beta_o+1} \tan\phi \quad (1.10)$$

1.5 COUPLING COEFFICIENT OF COUPLER-CAVITY SYSTEM

Analytical expressions for waveguide to cavity coupling have been derived by J. Gao using Bethe's small hole theory [11,12]. Coupling coefficient for an end coupled cavity with an elliptical iris is given as [11].

$$\beta = \frac{\Gamma_{10} k_o Z_o \pi^2 \exp^{-2\alpha d} l^6 e_o^4 H^2}{9ab[K(e_o) - E(e_o)]^2 P_o} \quad (1.11a)$$

where ' Z_o ' is the wave impedance of incoming rectangular waveguide, ' k_o ' is the free space propagation constant, ' λ ' is the free space wavelength, ' Γ_{10} ' is the propagation constant of fundamental waveguide mode (TE₁₀), l_1 is semi-major axis of ellipse and l_2 is semi-minor axis. $K(e_o)$ and $E(e_o)$ are elliptic integrals of first and second order, respectively. The eccentricity ' e_o ' is given as:

$$e_o = \sqrt{1 - \frac{l_2^2}{l_1^2}} \quad (1.11b)$$

$$Z_o = 120\pi \quad (1.11c)$$

$$k_o = \frac{2\pi}{\lambda} \quad (1.11d)$$

$$\Gamma_{10} = k_o \sqrt{1 - \left(\frac{\lambda}{2a}\right)^2} \quad (1.11e)$$

$$\alpha = k_o \sqrt{\left(\frac{\lambda}{\lambda_c}\right)^2 - 1} \quad (1.11f)$$

where ' λ_c ' is the cut-off wavelength in the iris region, ' d ' is the depth of the iris and ' H ' is the magnetic field (parallel to major axis) on the cavity when aperture is replaced by a metal surface. The input waveguide's width is ' a ' and its height is ' b '. For elliptical iris, if l_2 is kept constant and l_1 is varied over a length so that other factors in eqn. (1.11) do not vary considerably, then β varies as l_1^6 or S^6 where S is the area of the elliptic aperture ($= \pi l_1 l_2$) [11].

These expressions are quite useful in understanding the dependence of coupling coefficient on iris and waveguide parameters. The coupling coefficient shows a similar dependence for side coupled waveguide [12].

Useful scaling laws can be obtained from eqn. (1.11). For example, it can be observed from eqn. (1.11a) that coupling coefficient varies as square of cavity magnetic field ' H ' at iris location if other factors are constant. A scaling law can be obtained from these observations as [16]:

$$\beta = \beta_{model} \frac{Q}{Q_{model}} \frac{H^2}{H_{model}^2} \quad (1.12)$$

Here, it is important to note that stored energy is considered to be 1 Joule in both cases. Coupling coefficient also scales with iris length ' l ' as discussed earlier (approximately varies as l^6). The dependence on iris depth ($\exp^{-2\alpha d}$) is exponential. For an iris of dog-bone shape, an analytical expression is discussed in [16].

1.6 COUPLING COEFFICIENT MEASUREMENTS

Coupling coefficient of coupler-cavity system is generally measured with a vector network analyzer (VNA). The reflection characteristics at coupler port are observed on Smith chart to calculate the coupling coefficient. Impedance of resonant circuit varies with frequency and its plot makes a circle on Smith chart. Its intersection with real axis is given as coupling coefficient [15]. This method is not suitable for under coupled systems because of weak coupling. In such cases, transmission method is used. In this method, a small pick up port is introduced to measure transmission characteristics of coupler under study [17]. In this measurement, intrinsic quality factor measurement is also needed to calculate the coupling coefficient. The ‘ Q_o ’ is generally calculated from 3dB bandwidth (BW) as:

$$Q_L = \frac{f_o}{BW} \quad (1.13)$$

$$Q_L = \frac{Q_o}{1+\beta_1+\beta_2} \quad (1.14)$$

In this Q_o measurement, β_1 is negligible whereas β_2 is the known coupling of auxiliary (pick up port). The details of this method are given in Section 3.4.3.

1.7 LITERATURE SURVEY

RF couplers may need coupling adjustment in the following cases:

- Quality factor of the fabricated cavity is different than the simulated value.
- Change in the dimensions of the coupling iris because of fabrication tolerances.

- Ridge waveguide couplers with the requirement of high dimensional tolerance (eg. ± 50 microns in 1.55 mm iris of 352 MHz ridge waveguide coupler after brazing). This is required to keep the return loss better than -20 dB.
- Different test scenarios where multiple cavity sections are attached to single coupler.
- Beam loading and over-coupling requirements for meeting the bandwidth requirements in high Q superconducting structures.

Coaxial couplers provide the flexibility of coupling coefficient tuning as coupling can be changed by rotating the loop or moving the probe. In waveguide couplers, post fabrication iris machining can be used to increase the coupling [11-12]. However, it cannot be used to decrease it. In side coupled waveguide couplers, movable short is required to provide the coupling variation. These techniques are shown in Fig. 1.5. The other existing techniques require either an extra post or a movable short. In end coupled waveguide couplers, coupling can be changed by providing an extra post [18]. The traditional method of three stub tuning is also used in some couplers [19] but its use is limited to low power systems as reflected waves exist over the entire length between three stub tuner and cavity. Similarly, impedance matching elements like EH tuners are useful in low power systems only and not preferred in high power systems. This is because they result in standing waves over a larger region comprising of RF window and coupler. Considering these facts, it was considered important to research alternate ways to change the coupling coefficient in waveguide couplers without introducing an extra element.

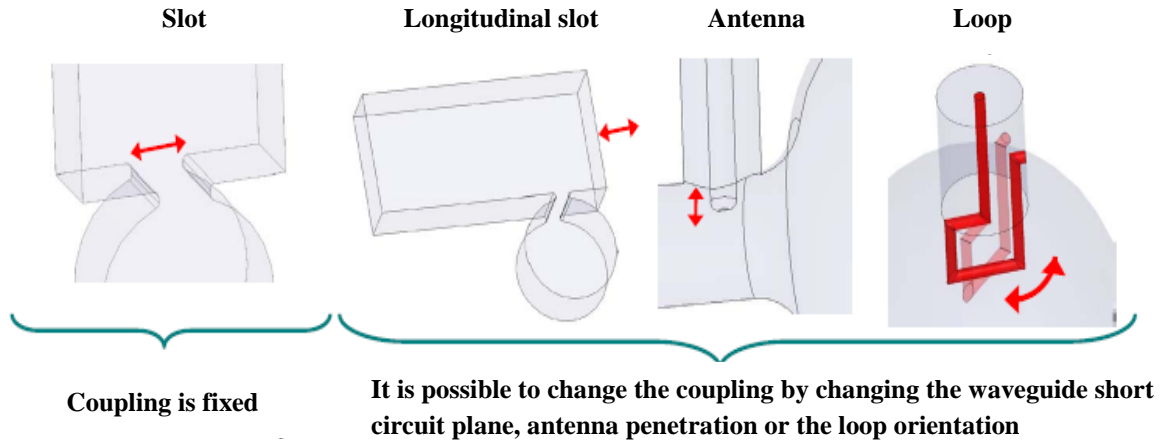


Fig. 1.5 Coupling coefficient tuning techniques in waveguide and coaxial couplers [13].

The coupler assembly is made up of several parts like RF window, cooling system, coupling adjustment system, biasing for multipacting suppression, etc. RF window is critical part of a coupler as it protects the cavity vacuum. It is prone to multipacting and overheating related damage during testing and operation. The development of RF window requires vacuum leak tight alumina to metal brazed joints. The couplers are generally conditioned on a test stand which consists of a test cavity with coupler ports for feeding and extracting the RF power. Some of the related coupler developments are discussed in [20-25].

A lot of progress has taken place in the technology development for high power CW couplers. RF power couplers working in the range of 350 to 1300 MHz and CW ratings exceeding hundreds of kilowatts have been reported for various accelerator facilities around the world [26-27]. Some of the SC cavity based facilities employing these high power CW couplers are given in [28-44]. A brief description of these couplers is given in Table 1.1. This table is an updated version of tables given in [23] and [26]. The high power couplers for room temperature cavities are reported in [45-54]. The highest power level used per coupler so far is 1 MW CW at

700 MHz for APT coupler [41]. This coupler is waveguide to coaxial type with variable probe coupling. Status of these high power warm cavity couplers is given in Table 1.2. Most of these facilities have adopted ridge waveguide technology for RFQ and DTL cavities operating at room temperatures. Maximum CW power obtained during testing is 300 kW for LEDA couplers [45]. Though ridge waveguide coupler designs are simpler than waveguide to coaxial couplers, they are found to be very sensitive to dimensional tolerances.

In all the waveguide coupler designs discussed in Table 1.1 and 1.2, the required coupling coefficient is obtained by post fabrication iris machining [45-49], [54] or by a waveguide short [50]. All high power waveguide couplers listed in Table 2 use a standalone waveguide window to protect cavity vacuum from the incoming waveguide line. As the power levels are high, a separate window is designed independently of coupler and iris part. These windows are available commercially because of standard waveguide size. However, the waveguide transition and iris dimensions are dependent on the type of accelerator cavity. Hence, the waveguide coupler transition and iris are designed and developed as per the specific impedance matching and size requirements of the accelerator cavity. Apart from the flexibility of coupling coefficient adjustments, couplers with waveguide to coaxial transitions can have disc type or cylindrical type window designs integrated to the coupler assembly.

The RF window is generally made up of high purity alumina. The coupler vacuum parts are made up of OFE Copper or copper coated stainless steel. RF window in coaxial couplers can be a coaxial disc, conical type, capacitive loaded or cylindrical as shown in Fig. 1.6

Table 1.1 List of high RF Power couplers for various accelerator facilities.

Facility	Freq. (MHz)	Coupler Type	RF window	Qext	Max. Power (kW)	Comments
LEP2 [28-30]	352	Coax. Fixed	Cyl.	2×10^5	Test: 565 Oper.: 100	Traveling wave With $\Gamma=0.6$
LHC [29, 31]	400	Coax. variable with 60 mm stroke	Cyl.	2×10^4 to 3.5×10^5	Test: 500 Oper. : 300	Traveling wave Standing wave
PEP-II B Factory [32]	476	WG. Fixed	WG disc	-	Test: 270	Traveling wave
HERA [33-34]	500	Coax. Fixed	Cyl.	1.3×10^5	Test: 300 Oper.: 65	Traveling wave
CESR [35-36]	500	WG. Fixed	WG. Berillia discs	2×10^5	Test: 250 : 125 Oper.: 155	Traveling wave Standing wave Beam Test
CESR [37]	500	WG. Fixed	WG. Disc	2×10^5	Test: 450 : 360 Oper.: 300	Traveling wave Forward Power Beam Test
TRISTAN [38]	509	Coax. Fixed	Coax. Disc	1×10^6	Test: 200 : Oper.: 70	Traveling wave
KEK-B [39-40]	509	Coax. Fixed	Coax. Disc	7×10^4	Test: 800 : 300 Oper.: 380	Traveling wave Standing wave
APT [41]	700	Coax. Variable (± 5 mm stroke)	Coax. Disc	2×10^5 to 6×10^5	Test: 1000 : 850	Traveling wave Standing wave
JLAB-FEL [42]	1500	WG. Fixed	WG. Disc	2×10^6	Test: 50 Oper.: 35	Very low ΔT
Cornell- ERL Injector [43]	1300	Coax. Variable with (± 15 mm stroke)	Cyl. (cold and warm)	9×10^4 to 8×10^5	Test: 61	
Cornell- ERL RF Gun [44]	704	Coax. Fixed	Coax. disc	4×10^4	Test: 125 Oper : 125	Traveling wave Standing wave

Table 1.2 List of RF Power couplers for room temperature accelerators.

Facility	Freq. (MHz)	Coupler Type	RF window	Duty Cycle	Max. Power (kW)	Comments
LEDA [45]	350	Ridge waveguide (tapered) with fixed iris coupling	Separate	CW	300	Traveling wave
PEFP-RFQ [46]	352.1	Ridge waveguide (tapered) with fixed iris coupling	Separate	24%	280	Traveling wave
PEFP-DTL [47]	352.1	Ridge waveguide (tapered) with fixed iris coupling	Separate	8%	800	Traveling wave
IPHI [48]	352.2	Ridge waveguide (tapered) with fixed iris coupling	Separate	CW	The design to be used for LINAC- 4 also. (500)	
LINAC4- RFQ, CERN [49]	352.2	Ridge waveguide (tapered) with fixed iris coupling	Separate	.1% (10%)*	500	Based upon IPHI design
LINAC4- DTL, CERN [50]	352.2	Waveguide side coupled with short	Separate	.1% (10%*)	750	Based upon IPHI design
TRASCO [51]	352.2	WG-Coax.	Cyl.	CW	100	Traveling wave
SNS (for RFQ) [52]	402.5	Coax.	disc	6%	100	Traveling wave
SNS (new design for RFQ) [53]	402.5	WG-Coax	disc	6%	450	Traveling wave
SNS (for DTL) [54]	402.5	Ridge waveguide	Separate	8%	2500	Traveling wave

*Maximum design value

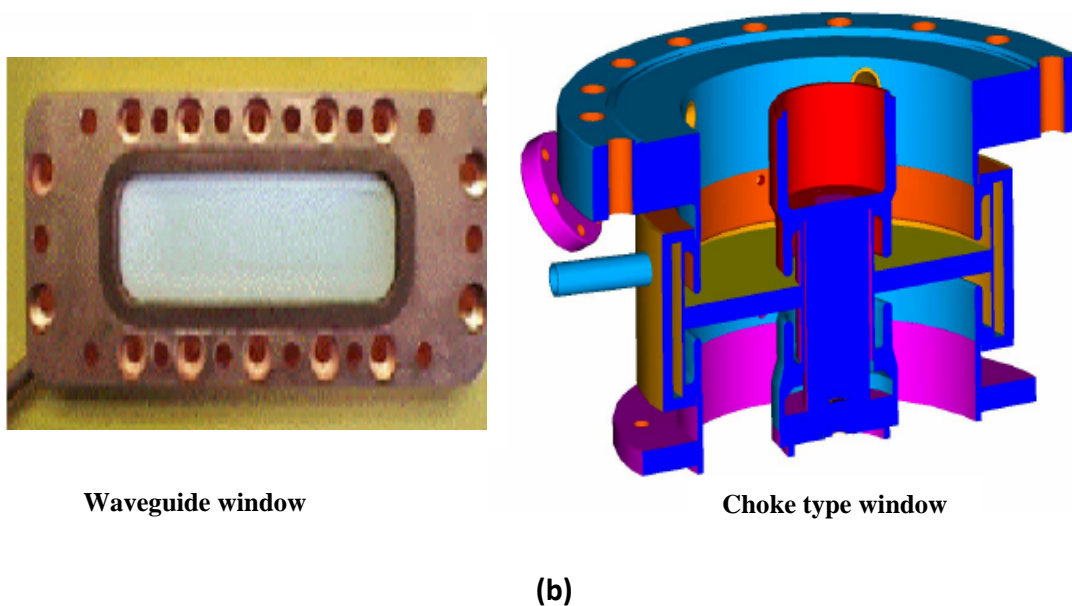
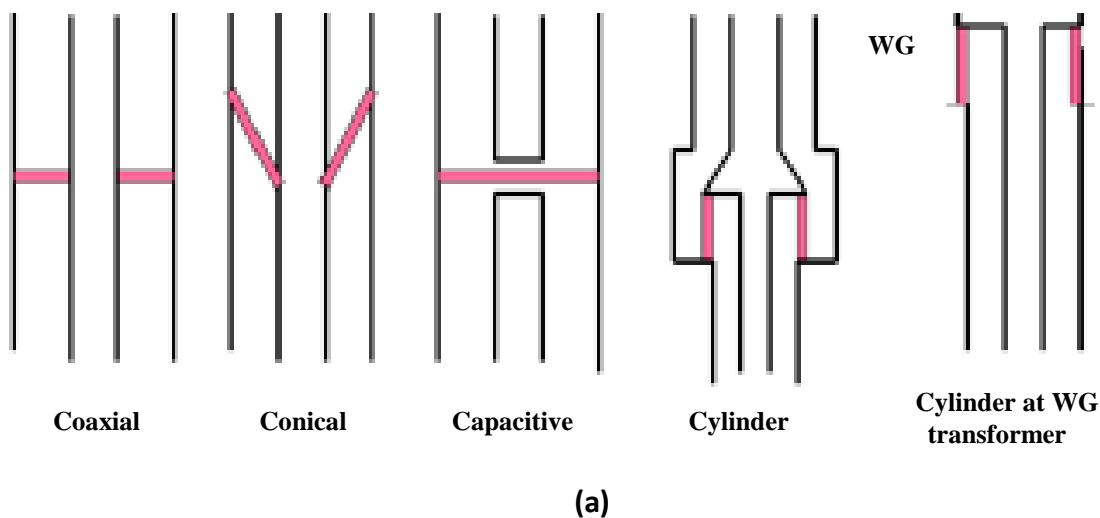


Fig. 1.6 Different window designs for (a) coaxial [13] and (b) waveguide geometry along with a choke type window [20].

A waveguide window is shown in Fig. 1.6(b) along with a choke type window in coaxial geometry. These window designs are used in high power RF couplers. A typical coupler assembly for a room temperature cavity is shown in Fig. 1.7(a). It uses a door-knob type waveguide to coaxial transition. Inner and outer conductors of coaxial parts are provided with

coolant channels. RF power coupler designs for SC cavities are more complex as compared to room temperature cavities. This is because of additional requirements of cleanliness, static and dynamic heat load analysis etc. A typical RF coupler assembly for a SC cavity is shown in Fig. 1.7(b). The coupler consists of waveguide to coaxial transition, disc type RF window, thermal straps for thermal management, detectors for arcing, vacuum, field emission, etc. It consists of two windows to separate the cavity side vacuum from room temperature side. Adjustable bellows are used in these couplers to take care of thermo-structural changes during cavity cool down. A movable inner conductor is used to obtain variable coupling.

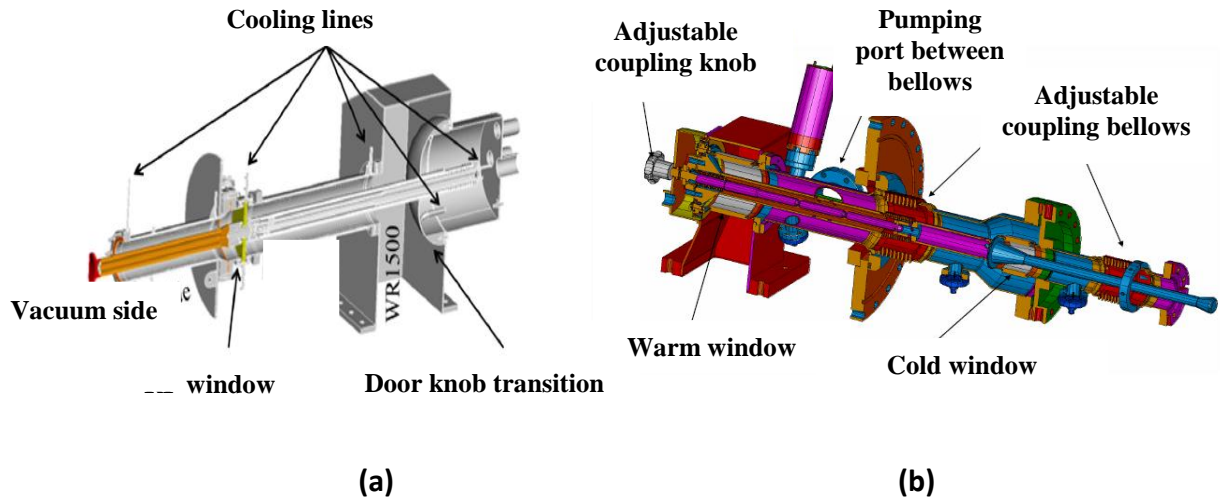


Fig. 1.7 Typical waveguide to coaxial transition based coupler for (a) room temperature cavity [27] and (b) for SC cavities [44].

The couplers are conditioned to the required power levels on test cavities before using them to feed power to accelerator cavities. The RF power is increased slowly at low duty cycle (generally less than .1%) to reach at the desired peak power. The duty cycle is increased in steps and conditioning is done up to the required power level and duty cycle. The reflected power,

vacuum and arc signals are monitored and kept below a set-point in order to avoid damage to coupler surface during RF conditioning. The RF conditioning set-ups for room temperature couplers are designed to test up to two couplers together as shown in Fig. 1.8. RF power is fed at the input coupler and is taken out from the output coupler. The output coupler is connected to a high power load to dissipate the power.



Fig. 1.8 Waveguide to coaxial type couplers connected to test cavity for RF conditioning [25].

The RF testing of couplers for SC cavities is done on a horizontal test stand which provides the necessary cryogenic environment for cavities. Such couplers can also be tested at room temperature in standing wave mode by reflecting the power. High current cavities without beam provide a mismatched load to couplers at cryogenic temperatures. Such couplers need coupling adjustment so that full power can be transmitted to the cavity during testing. The RF conditioning time of couplers may be reduced by baking and using multipacting suppression coating on coupler parts.

1.8 ORGANIZATION OF THESIS

Chapter 2 introduces the basic design procedure for a power coupler design. This procedure involves EM modeling using full wave solvers for RF matching, coupling coefficient, fields, RF losses and heating. The same procedure is followed in this thesis for designing and developing the proposed RF couplers. Commercial EM solver CST Microwave Studio [55] is used for RF analysis of the couplers. The RF characterization is carried out using a Vector Network Analyzer (VNA).

In Chapter 3, an alternative method is proposed for coupling variation by iris rotation in waveguide to cavity couplers. This method does not require iris machining. The effectiveness of the method is demonstrated by fabricating a prototype S-band cavity. Analytical formulations for coupling calculations in rotated iris are also carried out.

In Chapter 4, a detailed analysis is carried out on ridge waveguide couplers to study their dimensional tolerances for return loss and frequency variation. Tuners are proposed to relax this dependence. Also, two different types of ridge waveguide transitions (stepped and tapered) are compared for high power coupler applications.

Chapter 5 describes the design of two different type of coaxial couplers with integrated windows, which are developed for conditioning and feeding power to the RFQ cavity of a deuteron accelerator. A RF test cavity is also developed for the RF coupler testing. Finally, Chapter 6 concludes this thesis and also provides the ‘Future Directions’ in the area of RF power couplers.

CHAPTER-2

DESIGN PROCEDURE FOR HIGH POWER RF COUPLERS

2.1 INTRODUCTION

High power coupler design involves calculations for RF coupling, peak fields, RF losses, thermal and multipacting analysis. Mechanical design and fabrication aspects are important factors in the successful development of high power couplers. There are many review papers which explain the important design and technical issues of coupler development [13, 26, 27]. Considering the computational power of full wave EM solvers, it is important to discuss the key design steps involving computer aided design. The techniques proposed in the thesis for iris rotation and relaxing the dimensional tolerances have been analyzed by EM simulations on CST Microwave Studio (CST-MWS) [55]. This numerical solver is based on finite integration time domain technique and it solves the Maxwell equations in three dimensional structures. The ridge waveguide coupler, coaxial couplers and test cavity designs are optimized using CST-MWS. RF measurements for return loss and coupling coefficient are carried out using a Vector Network Analyzer.

2.2 EXTERNAL Q CALCULATIONS

The coupling coefficient of a power coupler to the cavity determines the reflected power from coupler-cavity interface. The control of fields in superconducting cavities becomes challenging

because of their high Q_o and low bandwidth. Hence, these cavities are generally over-coupled to obtain required loaded bandwidth. The coupling coefficient (β) can be obtained as:

$$\beta = \frac{Q_o}{Q_{ext}} \quad (2.1)$$

The value of Q_o can be obtained from analytical calculations for simple geometries. However, as accelerator cavities are complex structures, numerical electromagnetic solvers are used for Q_o calculations. The techniques proposed by Kroll Yu [56] and Pascal Balleyguier [57] can be used with numerical solvers for calculating Q_{ext} .

Pascal Balleyguier technique [57] is quite simple and useful for a broad range of Q_{ext} values. In a waveguide coupled cavity system as shown in Fig. 2.1, Q_1 and Q_2 values can be obtained for the open and shorted cavity respectively as given in [57]:

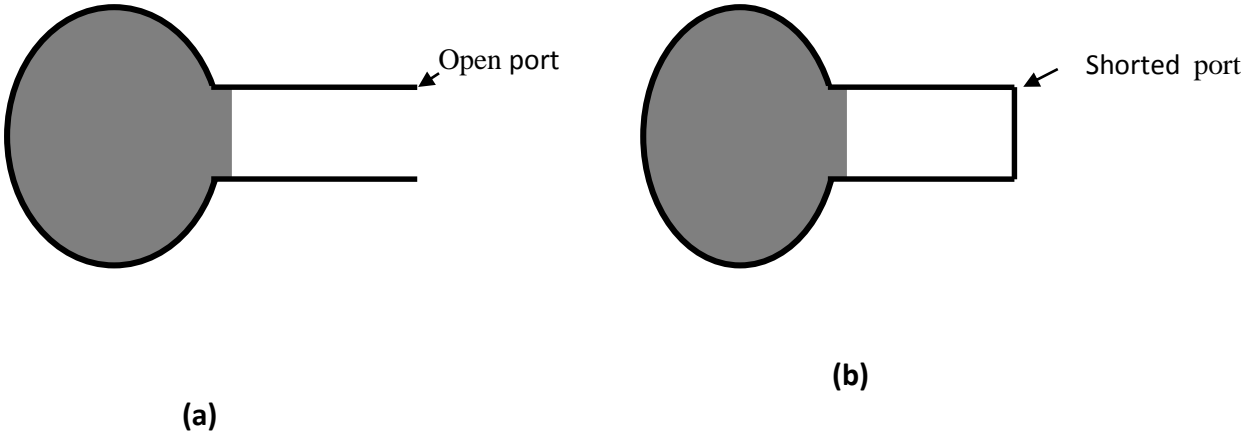


Fig. 2.1 A cavity connected to (a) open ended and (b) shorted waveguide.

$$Q_1 = \frac{\omega \iiint E^2 dV_{cavity}}{c \iint E^2 dS} \quad (2.2)$$

$$Q_2 = \frac{\omega \iiint H^2 dV_{cavity}}{c \iint H^2 dS} \quad (2.3)$$

$$Q_{ext} = Q_1 + Q_2 \quad (2.4)$$

Once the Q_{ext} value is obtained by using eqns. (2.2) to (2.4), coupling coefficient can be obtained from eqn. (2.1). The eqns. (2.2) and (2.3) consider the fields for open and shorted waveguide respectively. The surface of integration is the cross-section of incoming waveguide.

2.2.1 External Q calculation from Pascal Balleyguier Technique

In this technique, the Q_{ext} is calculated by taking two Eigen Mode solver runs. The first solver run is with perfect electric boundary and other with perfect magnetic boundary at waveguide input port. From eqn. (2.4), Q_{ext} can be written as:

$$Q_{ext} = \frac{\omega}{c} \left[\frac{\iiint_{cavity} E^2 dv}{\iint_{refplane} E^2 ds} + \frac{\iiint_{cavity} H^2 dv}{\iint_{refplane} H^2 ds} \right] \quad (2.5)$$

The first term in the bracket is calculated by using the magnetic boundary and the second term by using an electric boundary. Though, the length of the wave guide is arbitrary, a wavelength long waveguide is sufficient for simulations..

2.2.2 External Q calculation from CST Microwave studio

Suitable symmetry conditions are applied to reduce the computational effort while simulating the RFQ cavity and waveguide. The 1/4th model of RFQ with an iris and ridge waveguide using CST-MWS is shown in Fig. 2.2. The value of Q_{ext} comes out to be almost same by using Pascal Balleyguier method and CST-MWS [58]. Since Pascal Balleyguier method needs only two solver runs for the Q_{ext} calculation, it is very useful in calculating the Q_{ext} . The variation of

coupling coefficient with iris length is obtained with different runs of CST-MWS and is shown in Fig. 2.3. This is required while optimizing the iris dimensions for desired coupling.

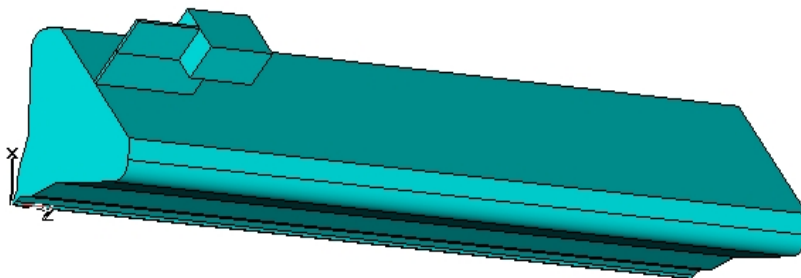


Fig. 2.2 CST- MWS model of (1/4 th) RFQ connected to ridge waveguide.

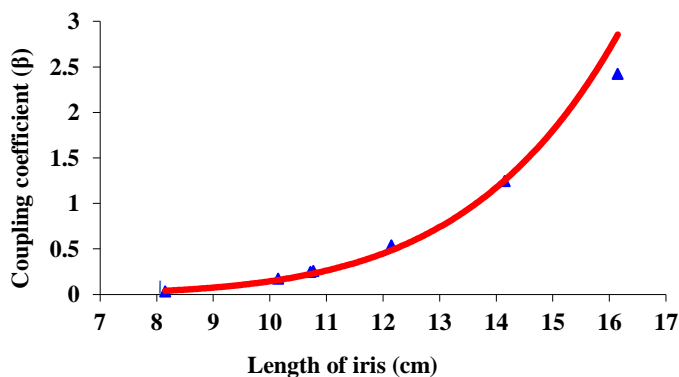


Fig. 2.3 Simulated coupling coefficient of RFQ to ridge waveguide coupling through a rectangular iris.

2.3 EM FIELD DISTRIBUTION INSIDE COUPLER

As discussed earlier, the power from incoming waveguide is coupled by an iris to the cavity whereas the coupling in coaxial couplers is achieved with either a probe (i.e., electric coupling) or loop (i.e., magnetic coupling). The whole coupler assembly is subjected to high electric and magnetic fields because of high power requirements. Hence, it is important to have reasonable

estimate of peak electric and magnetic fields inside the coupler assembly. Electric and magnetic field concentrations near sharp corners need special attention during design stages. High electric fields in the dielectric window region can cause dielectric heating in the window whereas high magnetic fields near the metal surfaces produce RF loss on metal parts.

As the electromagnetic solvers are used in the design stages, one should be careful with the meshing near the sharp points. The meshing should be fine enough so that simulated field values are close to actual values. As an example, let us consider a ridge wave guide with corner rounding. We can see from Fig. 2.4 (a) that there is more concentration of fields near the corners of ridges. The peak electric field at rounded corner was also studied for different mesh densities. Fig. 2.4 (b) shows a typical meshing near ridge corner in $1/4^{\text{th}}$ model of ridge waveguide. A denser mesh is used at the rounded corners. The convergence behavior of field values with and without corner rounding is given in Table 2.1. The field values converge faster with corner rounding.

2.4 CAVITY FREQUENCY AND FIELD PERTURBATION

Any perturbation to the accelerator cavity causes a resonance frequency shift in the cavity. This shift can be estimated by Slater's theorem [59] and by numerical solvers. Apart from the frequency shift to the cavity, the coupler produces local field changes in the cavity. As a general guideline, these perturbations should be kept to minimum. Frequency shift introduced by the coupler is unavoidable, so frequency tuning system is generally incorporated in accelerator cavities. In loop and probe type couplers, the change in cavity frequency by coupler port opening can be canceled by suitable choice of metal thickness of loop or probe. Similarly, decrease in the cavity frequency by iris opening in waveguide couplers can be cancelled by slight movement of

the metallic iris into the cavity. Most of the time, these studies are carried out using full wave solvers and fabricating prototypes so that full power coupler-cavity system works satisfactorily.

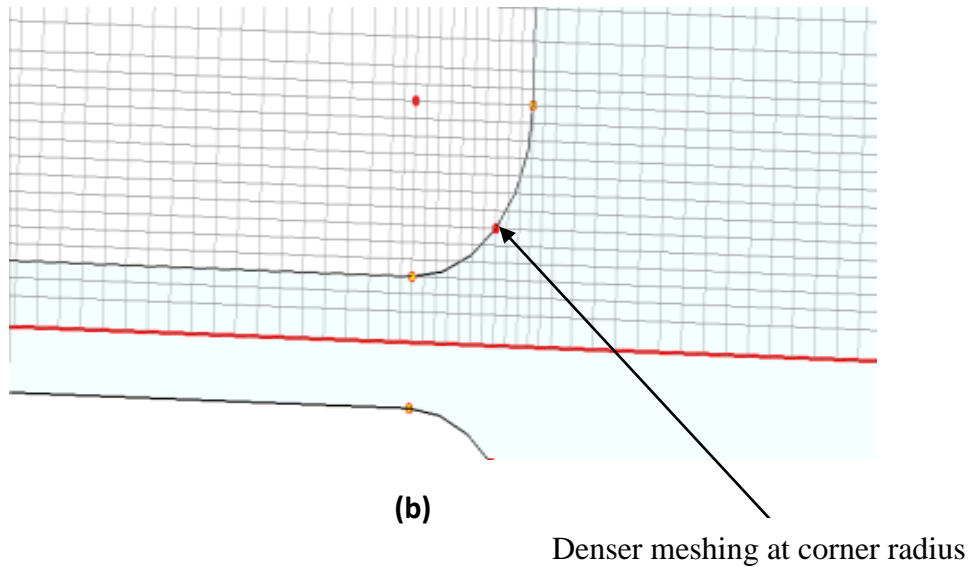
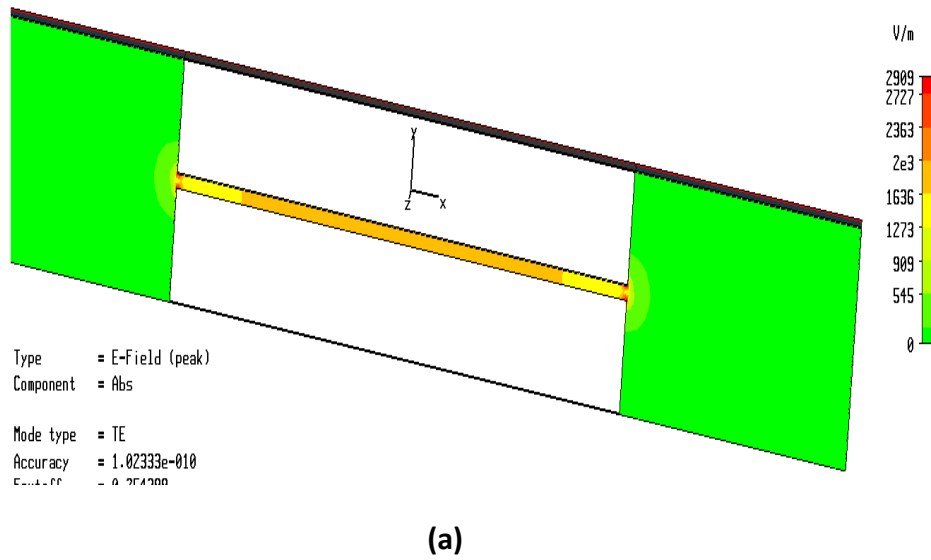


Fig. 2.4 Plot of (a) E field in ridge waveguide and (b) view of meshing near the rounded corners.

Table 2.1 Convergence of Peak electric field with mesh size.

Min. mesh size (microns)	Number of Mesh cells	E_{max}/E_{avg}. (without corner radius)	E_{max}/E_{avg}. (with 1 mm corner radius)
375	864	1.11	1.11
187.5	2610	1.39	1.12
93.66	15180	1.8	1.12
46.95	82368	2.89	1.13
12.15	4157384	3.42	1.13

In the above simulations, ridge waveguide of width 189 mm and height 35 mm is chosen. The ridge gap is 1.55 mm. In the prototypes, in-order to avoid field concentrations, typical corner radius has been kept as 2 mm.

2.5 RF LOSS CALCULATIONS AND THERMAL ANALYSIS

The coupler assembly is supposed to transfer full incoming power to the cavity, but it does not happen in practice even for perfectly matched system (i.e., critically coupled system). The RF currents produce heating on metal parts. At high frequencies, the RF loss occurs on surface because of very small skin depth. Hence, this loss is also called surface loss, which can be calculated as:

$$P_{surface} = \frac{R_s}{2} \iint H^2 dS \quad (2.8)$$

where R_s is the surface resistance and H is magnetic field on the metallic surfaces. The other form of loss is volumetric loss, which takes place in the dielectric barrier of RF window and is given as:

$$P_{volumetric} = \frac{\omega^2 \epsilon_r \tan(\delta)}{4} \iiint E^2 dV \quad (2.9)$$

where ' ϵ_r ' is the relative permittivity and $\tan\delta$ is the loss tangent of the dielectric material. The surface resistance of metal parts and loss tangent of the dielectric should be small for low losses.

The required electric and magnetic field distributions inside the coupler can be calculated using a full wave EM solver. Most of the commercial EM solvers like CST Microwave Studio, HFSS, COMSOL, etc. have post-processing tools to perform above integrations for the solved fields.

Generally, port boundary of these solvers feed 1 W of power. The field values need to be suitably scaled to the required power levels during post-processing. The electrical conductivity of metal should be carefully considered as there can be variation from theoretical values of ideal surfaces and practical surfaces. Considering a safety factor of 20-30% can be useful to account for deterioration of electrical conductivity because of surface conditions. Nearly 90% of simulated quality factor can be achieved in accelerator cavities by machining the surfaces to sub-micron finish and following proper cleaning procedures like ultrasonic bath, pressure rinsing, etc. [14]. Same surface quality needs to be maintained for power couplers as well.

In couplers for superconducting cavities, static and dynamic thermal loads from the couplers to the cavity need to be calculated. The thermal straps are located at different positions along the couplers so that thermal load on 4K liquid helium system is minimal. One such schematic for the coaxial couplers is shown in Fig. 2.5 and resulting temperature distribution along the coupler length is given in Fig. 2.6 [60]. As the temperature gradient exists along the coupler length, static heat loss to the 2 K system needs to be minimized. This is because cost of heat removal is more for 2 K than for 15 K and 125 K system. These results are obtained from the simulations using CST-MWS.

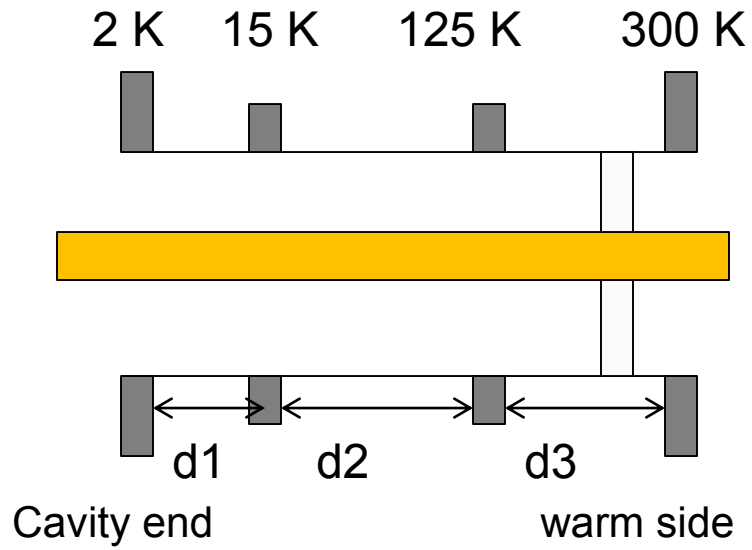


Fig. 2.5 Schematic view of coaxial coupler with thermal straps at 15 K and 125 K [60].

For a typical coupler of 220 mm length, the distance of 15K thermal strap 'd1' is optimized to be 15 mm whereas distance 'd2' is around 140 mm [60].

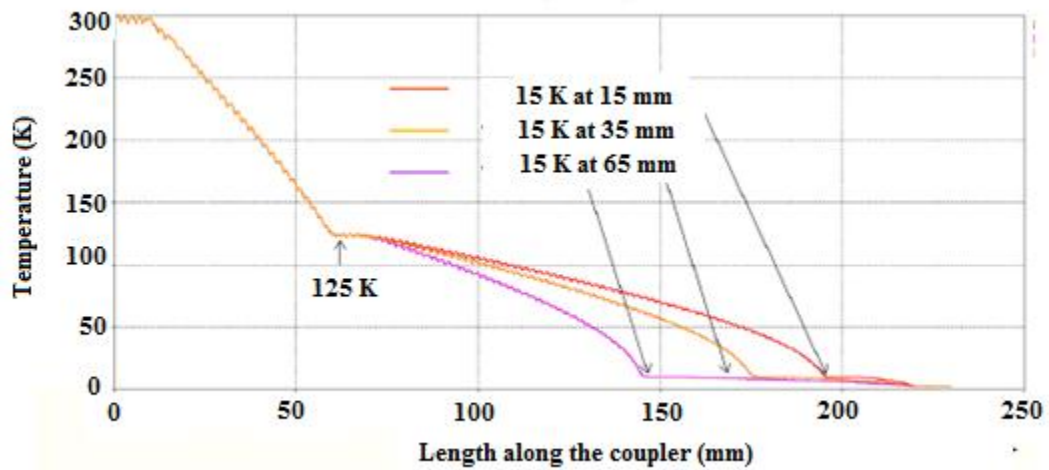


Fig. 2.6 Simulations of temperature variation along the coupler for different 15 K thermal strap positions [60].

2.6 MULTIPACTING ANALYSIS

Multipacting is a resonant secondary electron emission from metal surfaces inside vacuum. In simplistic terms, if the time of travel between two surfaces is equal to half the RF period, an exponential growth of secondary electrons takes place and leads to multipacting discharge. This is harmful to couplers because it produces impedance change and hence reflections, localized overheating, window rupture, etc. The problem of multipacting and its mitigation techniques have been studied extensively [61-63]. Simple scaling laws have been established for coaxial lines and waveguides. Multipacting power level in coaxial lines depend on RF frequency (f), gap between the line conductors (d) and characteristic impedance (Z_o) [62]:

for one point multipacting:
$$P \propto f^4 d^4 Z_o \quad (2.10)$$

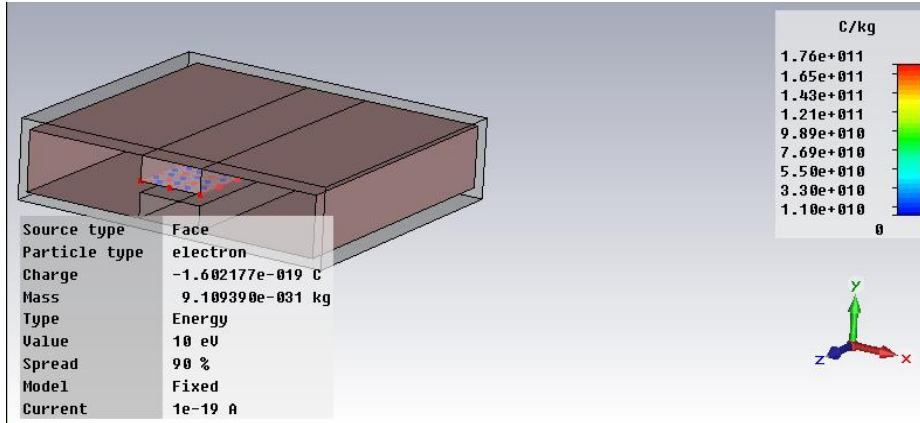
and for two point multipacting as:
$$P \propto f^4 d^4 Z_o^2 \quad (2.11)$$

Many numerical solvers have also been developed to track secondary electrons and predict multipacting in various accelerator laboratories. Apart from resonance condition, other factors like dependence of secondary electron yield (SEY) on surface condition in practical conditions also play a role. Still, it is better to analyze the coupling structures for multipacting susceptibility during the design stages itself. To give an example, a ridge waveguide structure is studied for multipacting levels using CST MWS. The location of electrons and electron trajectories for a typical ridge waveguide are given in Figs. 2.7(a) and (b), respectively. These simulations are performed using tracking (TRK) solver of CST-MWS. The particles are defined on the upper and lower ridge surfaces to predict the multipacting threshold value at 352.2 MHz. The simulated power level of multipacting threshold for the considered ridge waveguide is approximately

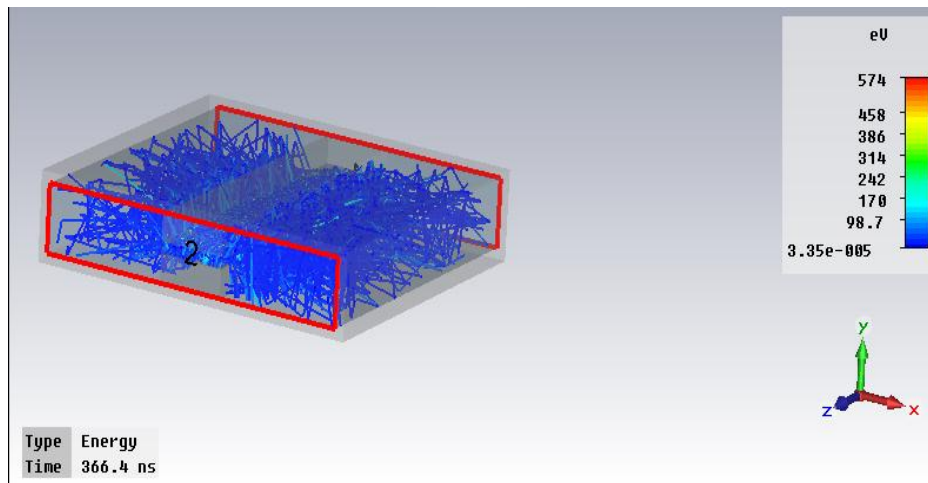
0.7 kW. This matches closely with the value of 0.68 kW as predicted from multipacting scaling laws for ridge waveguides [64].

2.7 FABRICATION AND TESTING ASPECTS

Fabrication and RF conditioning require maximum resources in terms of materials, fabrication facilities and conditioning set-ups, so a careful and iterative design process is required to reach at optimum design choices. The most commonly used material for RF couplers in both normal conducting and superconducting couplers is OFE copper. The brazing of copper parts is done in vacuum or hydrogen furnace. The flanges are made up of SS 304L or SS316. Either conflat or helicoflex vacuum seals are used for coupler flanges. Brazing of alumina disc to inner and outer copper conductors needs careful design of fixtures in-order to control the unequal expansion of alumina and copper during high temperature brazing in vacuum furnace.



(a)



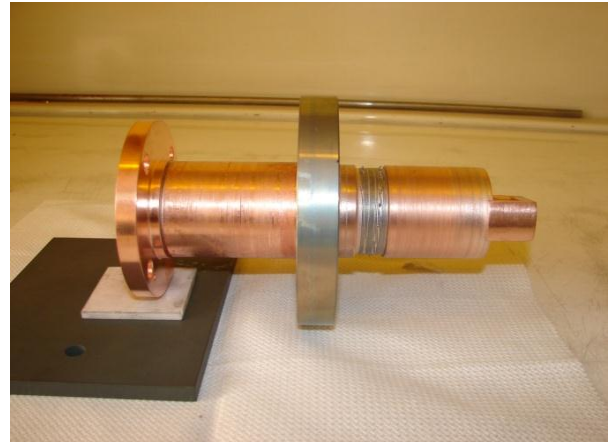
(b)

Fig. 2.7 View of (a) location of initial electrons and (b) simulated electron trajectories inside ridge waveguide

Fig. 2.8(a) shows different parts of a typical coaxial coupler before brazing and Fig. 2.8(b) shows a brazed coaxial coupler. The brazed coupler assembly is cleaned for any oil and dust contamination and tested for vacuum leak rate of better than 1×10^{-10} torr liters/sec. Generally, a separate cavity and test set-up is used to condition the couplers. The RF conditioning is started in pulsed mode and peak power is raised to design value. The pulsed width and repetition rate is increased slowly to reach at final design value [54].



(a)



(b)

Fig. 2.8 Coaxial coupler parts (a) before and (b) after brazing.

Details of these coaxial coupling structures are given in Chapter 5. The SC couplers require elaborate test set-ups consisting of vertical and horizontal test stands for coupler conditioning. The set-ups are necessary to create required cryogenic environment in the cavity region. Parts of SC couplers also experience cryogenic temperatures.

2.8 SUMMARY

Important design steps and considerations for RF Coupler design and development are explained briefly in this chapter. Though most of the initial design work involves electromagnetic simulations, the successful development of coupling structures is a multidisciplinary area involving expertise in thermal, mechanical, materials, fabrication and RF conditioning. EM simulation tools are used at various design stages of the RF couplers. The successful technology development of couplers require precise brazing with vacuum compatible joints and elaborate RF conditioning set- ups.

CHAPTER-3

COUPLING VARIATION BY IRIS ROTATION IN WAVEGUIDE COUPLERS

3.1 INTRODUCTION

Waveguide to cavity coupled systems frequently need coupling coefficient adjustments after fabrication. The change in coupling is achieved either by changing the dimensions of iris mechanically or introducing a matching post. A novel coupling coefficient tuning method based upon iris rotation is proposed. The coupling can be varied over a wide range without changes in the dimensions of the iris or an extra matching post. The proposed method of iris rotation can be compared to loop rotation in coaxial couplers. As the direction of magnetic moment changes, the effective coupling decreases when a loop is rotated. A scaling procedure is defined to obtain the coupling coefficient of rectangular iris of arbitrary length and width. The targeted value of coupling coefficient can be obtained by rotating the iris. This also opens up the possibilities of coupling coefficient tuning over a wider range without machining requirements on fabricated components.

3.2 EM SIMULATIONS FOR IRIS COUPLED CAVITY AT 350 MHz

RF coupling in magnetically coupled systems can be varied by changing the area of the loop [65] or by rotating the loop [66]. In some waveguide to coaxial transition based systems, the coupling can be tuned by changing the waveguide short position [67]. In the directly coupled waveguide

to cavity systems, a small aperture or iris is used in the end wall for coupling as shown in Fig. 3.1.

As discussed in Section 1.5, for an elliptic iris based waveguide to cavity coupling system, coupling coefficient β for TE₁₀ mode of waveguide is given as [11]:

$$\beta = \frac{\Gamma_{10} k_o Z_o \pi^2 \exp^{-2\alpha d} l_1^6 e_o^4 H^2}{9ab(K(e_o) - E(e_o))^2 P_o} \quad (3.1)$$

For elliptical iris, β varies as l_1^6 or S^6 where S is the area of the elliptic aperture ($=\pi l_1 l_2$) [11].

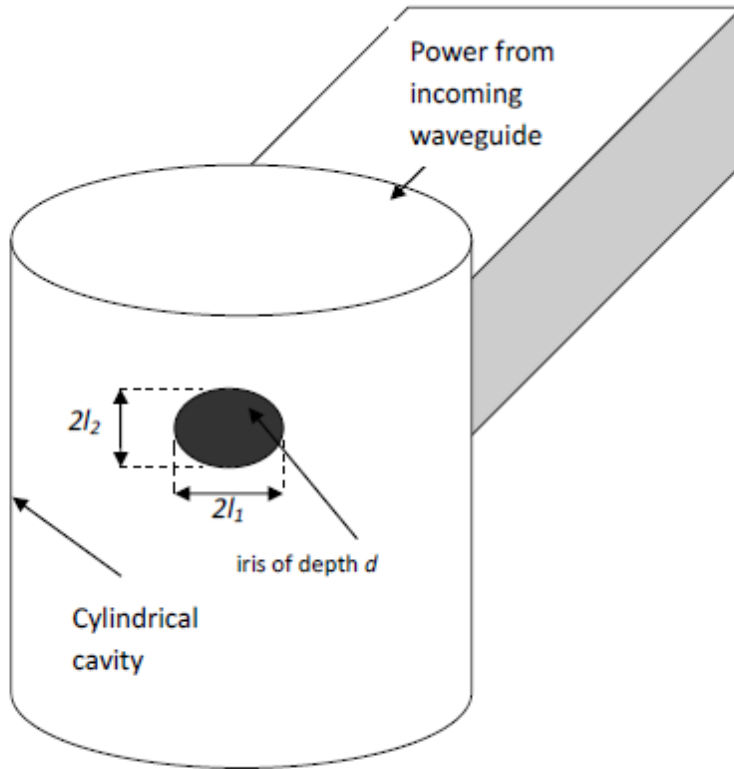


Fig. 3.1 Schematic of iris coupled cavity.

However, coupling can only be increased by post fabrication machining as it increases with length. This is true for other practical iris shapes like rounded edge rectangular iris [11] and dog-bone shaped iris [68, 69]. As discussed earlier, a matching post before the iris can also be used to obtain the required coupling [18]. However, to the best of author's knowledge, the iris rotation based coupling tuning in couplers is being proposed in this work for the first time.

3.2.1 Simulation Model and Scaling Procedure

To demonstrate the existing schemes of coupling variation and proposed scheme thereafter, a pill box cavity is considered. The cavity of length 50 cm and radius of 32.8 cm is modeled using CST-MWS. With around 20000 mesh cells, the resonance frequency of TM_{010} mode using Eigen Mode Solver of CST-MWS is found to be 349.51 MHz, which is 0.16% less than calculated value of 350.0923 MHz. Quality factor (Q_o) from post processor calculations (boundary conductivity (σ) = 5.8×10^7 S/m) is found to be 56364. The cavity is coupled to a half height WR2300 waveguide (width a = 58.4 cm, height b = 14.6 cm) by a rectangular iris. The cross sections of waveguide and iris are shown in Fig. 3.2. The coupling from dominant TE_{10} waveguide mode to TM_{010} mode of pill box cavity is considered. Q_{ext} value is obtained from 'Modal Solver' of CST-MWS. The simulation model is shown in Fig. 3.3. Coupling coefficient β is calculated by taking the ratio of Q_o and Q_{ext} .

An iris of rectangular shape is considered for demonstrating the proposed scaling method (explained in Section 3.2.4) and iris rotation method (explained in Section 3.3). However, the proposed iris rotation based method can be implemented for other iris shapes and sizes as well.

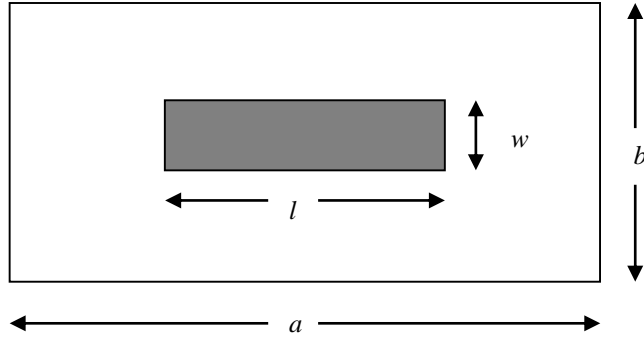


Fig. 3.2 Cross-section view of rectangular waveguide and iris.

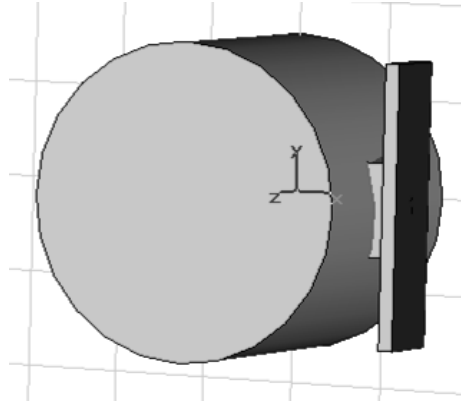


Fig. 3.3 Simulation Model of waveguide to cavity coupled system.

3.2.2 Coupling coefficient variation with iris length

To demonstrate the variation of coupling with length, a rectangular iris of length $l = 20$ cm, width $w = 10$ cm and depth $d = 2.8$ cm is considered. The length l is varied from 7.5 cm to 20 cm in steps of 2.5 cm. For each length of iris, separate run of Eigen Mode solver of CST-MWS is made. For all β calculations, an average value of $Q_o = 55,000$ is considered. The results are plotted in Fig. 3.4. The curve fitting gives a $l^{6.1}$ variation for coupling, which is close to that

shown in [12] in spite of the fact that coupling shape considered in [12] is elliptical. This fact has been noticed in [11] as well for rounded edge rectangular iris.

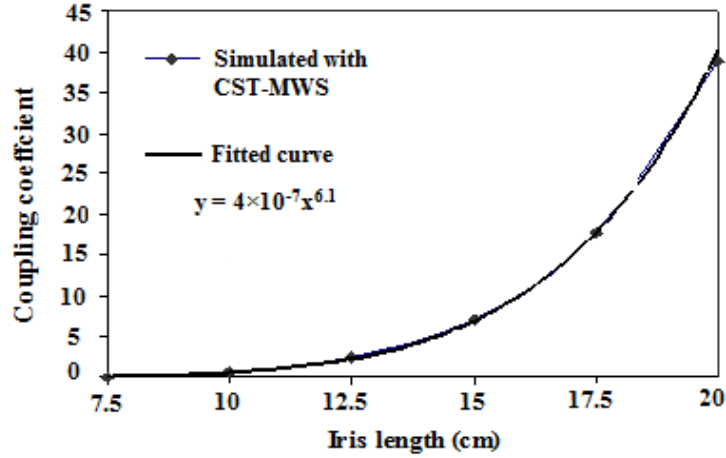


Fig. 3.4 Variation of coupling coefficient with length of iris (width = 10 cm).

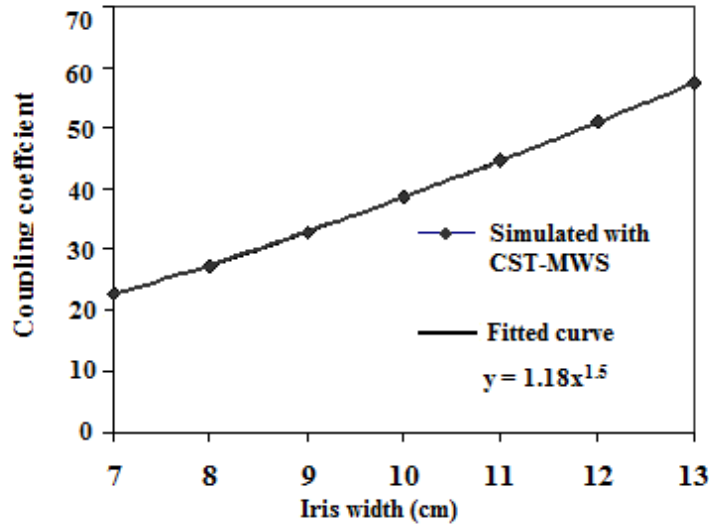


Fig. 3.5 Variation of coupling coefficient with width of iris (length = 20 cm).

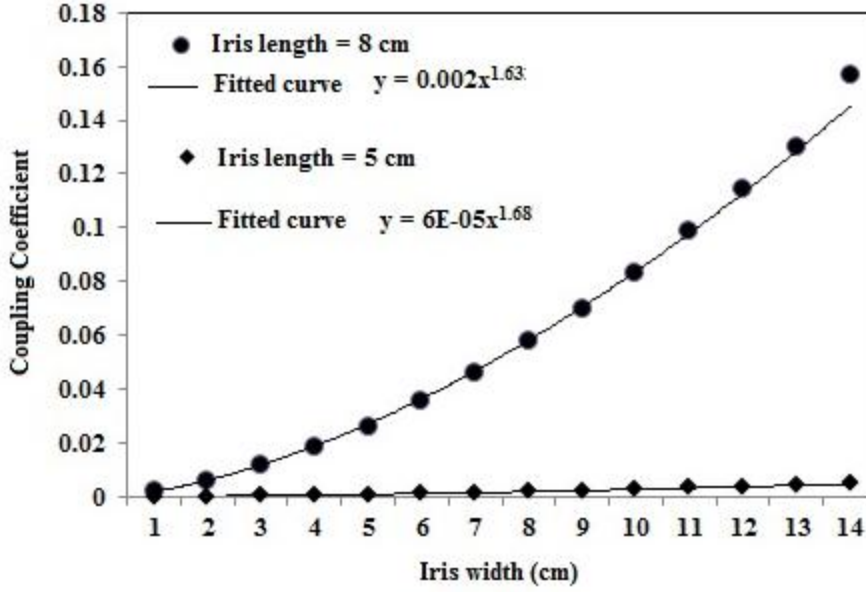


Fig. 3.6 Variation of coupling coefficient with iris width for different iris lengths.

3.2.3 Coupling coefficient variation with iris width

The coupling variation with the width of iris for a given iris length of 20 cm is also obtained. The width is varied from 7 cm to 13 cm in steps of 1 cm and simulator is run for each width to calculate Q_{ext} values. The plot of coupling variation with width is shown in Fig. 3.5. The curve fitting gives a variation of $w^{1.5}$. However, CST-MWS simulation results for other iris lengths as shown in Fig. 3.6 indicate that this dependence is not universal. The relation for width dependence has been combined with the results of Section 3.2.2 to obtain a scaling formula in next Section.

3.2.4 Scaling of Coupling Coefficient for different iris sizes

Following scaling procedure is defined which can take care of changes in length and width of a rectangular iris.

$$\beta_2 = \beta_1 \left(\frac{l_2}{l_1} \right)^{6.1} \left(\frac{w_2}{w_1} \right)^{1.5} \quad (3.2)$$

where β_2 is coupling coefficient for iris of length l_2 and width w_2 , β_1 is coupling coefficient for iris of length l_1 and width w_1 . If coupling is known for a particular length and width, it can be scaled to other iris sizes of different lengths and widths. For example, the coupling coefficient is extrapolated for iris of length $l = 20$ cm, $w = 10$ cm, $\beta_1 = 38.73$ to rectangular iris of 10 cm length. The width is varied from 1cm to 20 cm in steps of 1cm. The plot of simulated values and calculated values using eqn. (3.2) is shown in Fig. 3.7.

It is seen that values calculated by eqn. (3.2) follows simulated values quite closely up to iris width of 15 cm. However, the rate of rise of coupling comes down thereafter. The reason for this mismatch with eqn. (3.2) is because of the height of input waveguide, which is 14.6 cm. When the width of coupling iris is increased beyond this value, there is no appreciable increase in the coupling as physical area available for coupling remains same. Hence the scaling based upon eqn. (3.2) works well only for iris sizes much less than the input waveguide dimensions.

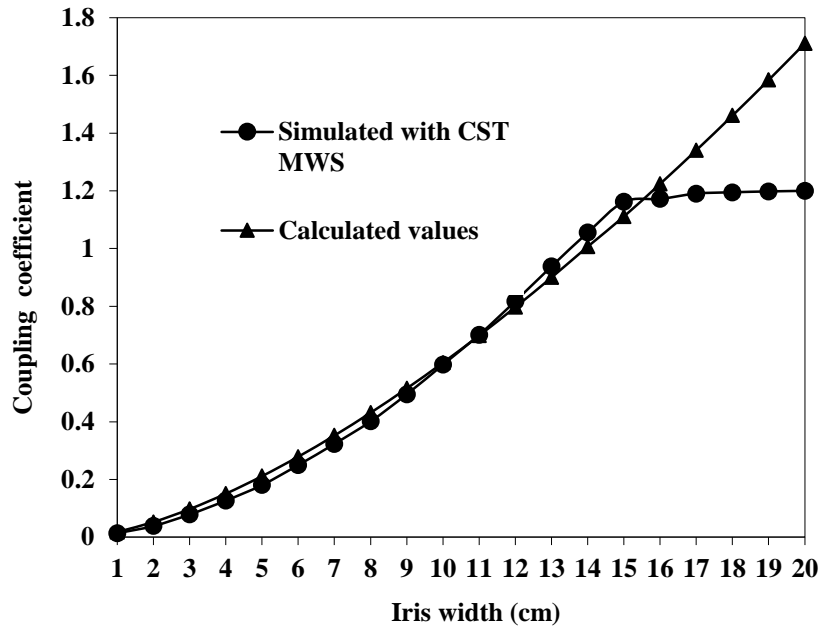


Fig. 3.7 Variation of coupling coefficient with width for an iris of length 10 cm.

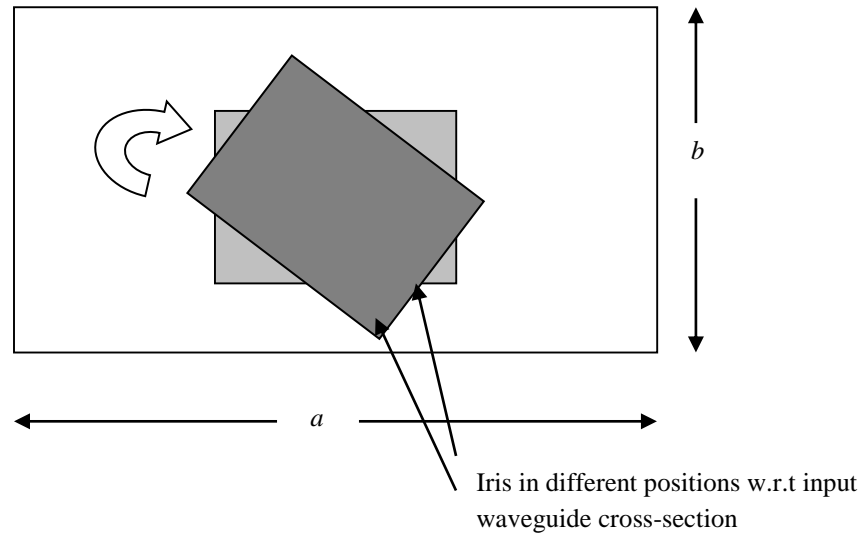


Fig. 3.8 Cross section of iris in two different positions of 0 degree and 45 degrees.

Above equations have been found to be valid for a limited range of changes in l_2 ($l_2 \leq a/3$) and $w/l < 1.5$. For the larger changes, it is difficult to define power scaling. This is because the length

based dependence of eqn. (3.1) is derived from the concept of magnetic moment associated with the apertures. The magnetic moment definition assumes small iris sizes with respect to the wavelength, so that static field distributions could be assumed [11]. Hence, as the size of the iris approaches waveguide width, the $l^{6.1}$ power scaling for length variation is not valid.

A procedure for coupling calculations for rectangular iris with rounded edges has been explained in [11]. This procedure uses the concept of equivalent area of an elliptical iris. However, only change in length of the iris in a limited range has been considered in [11].

3.3 PROPOSED TECHNIQUE FOR TUNING OF COUPLING COEFFICIENT

The saturation of coupling variation for iris sizes exceeding the waveguide dimensions leads to the idea of changing the effective coupling area by rotating the iris in the plane of input waveguide. When an iris of length 20 cm and width 10 cm is rotated clockwise, it will intercept different areas and hence coupling coefficient should change. A schematic of iris rotation with respect to the waveguide iris for two different positions of zero degree and 45 degrees is shown in Fig. 3.8. The variation in coupling by iris rotation is verified by numerical simulations using CST-MWS. The iris is rotated in steps of 10 degrees from 0 to 90 degrees and at each step coupling coefficient is calculated. The variation of coupling with rotation angle is plotted in Fig. 3.9. The coupling happens to peak at about 10 degrees because the iris is conformal and effective depth changes with rotation.

By rotating the iris up to 90 degrees, the coupling can be decreased appreciably (from 38.7 to 1.2). This can be a very useful technique to obtain the required coupling. By suitably designing the iris size, required critical coupling (for room temperature cavities) or over-coupling (for super conducting cavities) can be achieved. The coupling can be increased or

decreased by rotating the iris with respect to the plane of the input waveguide. For a square iris of 10 cm length, it is found that after a small increase from 0.59 (at 0 degree) to 0.749 (at 10 degrees), coupling stays constant with rotation and eventually falls to 0.59 at 90 degrees.

This is expected as 10 cm size is less than any of the input waveguide dimensions, and overlap area remains constant throughout the rotation. The coupling variation for 10 cm by 10 cm iris is shown in Fig. 3.10. As expected, the variation is symmetric with respect to iris position at 45 degrees.

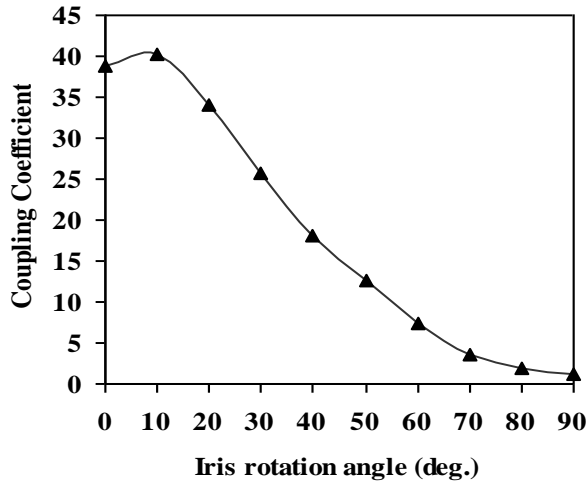


Fig. 3.9 Coupling coefficient variation with iris rotation for iris of size $l = 20$ cm and $w = 10$ cm.

3.4 ANALYTICAL EXPRESSIONS, PROTOTYPING AND MEASUREMENTS

Theory of coupling and radiation by small apertures in an infinite conducting wall has been studied by H. Bethe [70] and modified further by Bouwkamp [71]. Further, for apertures of arbitrary shapes, Cohn has obtained electric and magnetic polarizability values by measurements in a chemical cell [72]. Bethe's theory has been used to obtain analytical expressions for waveguide to cavity coupling by Gao [11]. Gao has further extended the analysis from end

coupled waveguide [11] to side coupled waveguide-cavity system [12]. For practical apertures of finite thickness, Gao has included attenuation coefficient to evaluate coupling coefficient of a waveguide-cavity coupled system.

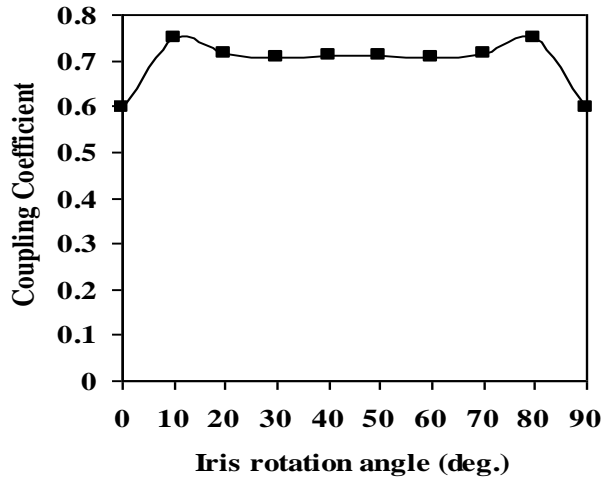


Fig. 3.10 Coupling coefficient variation with iris rotation for iris of size $l = 10$ cm and $w = 10$ cm.

In Section 3.3, a novel way of changing the coupling coefficient by iris rotation in RF couplers for accelerator cavities is explained. Concept of iris rotation is demonstrated using CST-MWS. A pill box cavity resonating at 350 MHz is simulated for rotated rectangular and square iris coupling only. The work is further extended to derive analytical expressions for rotated irises from first principles using Bethe's theory. Other iris shapes like circular and elliptical are also analyzed apart from rectangular and square irises. S- band cavity is fabricated and microwave measurements are carried out to verify the proposed analytical results. A smaller coupler-cavity system at S- band is analyzed as compared to 350 MHz system in Section 3.3. Iris rotation based

technique is expected to be useful alternative to existing techniques based upon post fabrication machining for coupling adjustments in particle accelerator cavities. Hence, a detailed analytical study of such coupling structures will be useful.

In the context of accelerator cavities, Pascal Balleyguier has used a method for calculating external Q numerically with lesser solver runs [73]. An equivalent circuit based approach for external Q calculations is reported in [74] but it doesn't consider rotated iris. Though, iris at an angle has been used in waveguide directional couplers as a means to get different power divisions [75-77], the techniques used to obtain coupling values are either purely numerical or studied in the context of waveguide to waveguide coupling. There are many numerical studies on rotated iris coupling for filters [78] and EMC applications [79]. Bethe's theory has been used recently to evaluate coupling in rectangular coaxial lines [80].

Bethe's original theory is modified by Collins by including reaction terms [81]. The modified theory is useful for waveguide-waveguide and waveguide-cavity coupling calculations to obtain physically realizable equivalent circuits. The Collin's approach has been used for analytical studies on open resonator coupling [82] and cavity to cavity coupling [83]. However, in particle accelerator resonator cavities, information of external quality factor and coupling coefficient is good enough for describing their behavior at resonance because of single frequency operation. Hence, description of reaction terms for obtaining the physically realizable equivalent circuit may not be needed. As described in [11-12], by using Bethe's original theory, coupling coefficient for iris coupled waveguide to cavity system can be obtained with reasonable accuracy. Bethe's theory is used to arrive at analytical expressions for External Q and coupling of an iris at arbitrary orientation. A rectangular iris is chosen because of its simplicity and regular use in practical waveguide-cavity coupled systems in accelerators. It also provides wider range

of coupling variation with iris rotation as compared to square and circular iris shapes as shown in Section 3.4.2. Analytical expressions are not available for rectangular iris as opposed to elliptical iris. However, polynomial based methods are available [84-86]. Magnetic polarizability (i.e. longitudinal and transverse magnetic polarizability) is calculated for rectangular iris from these polynomial methods. These values are used to define dyadic magnetic polarizability of rectangular iris for arbitrary iris orientation in the plane of incoming waveguide. Attenuation based term is included to account for finite iris length [12, 87].

External quality factor is evaluated explicitly because it is the characteristic of coupler-cavity geometry and size only. It is independent of cavity material and its surface qualities. The External Q values for arbitrary iris angle are used to obtain coupling coefficient of the given system for a known intrinsic quality factor.

3.4. 1 Theory of coupling calculations for rotated iris

A WR340 waveguide and rotatable rectangular iris for coupling power to a cylindrical pill box cavity is considered. End coupled waveguide to cavity coupling is used. The schematic of waveguide-cavity system along with rotatable iris cylinder is shown in Fig. 3.11.

The incoming waveguide and cylindrical cavity operate in TE_{10} and TM_{010} modes respectively. The dimensions of waveguide, cavity and iris are also shown in Fig. 3.11. The rectangular iris is cut inside a solid metallic cylinder. For the chosen dimensions, resonance frequency of cavity from analytical calculations comes out to be 2.373 GHz. In Fig. 3.11, iris length (major axis) is denoted by ' l ' and width (minor axis) as ' w ' and depth by ' d '. Cavity length is denoted by ' L ' and diameter as ' D '.

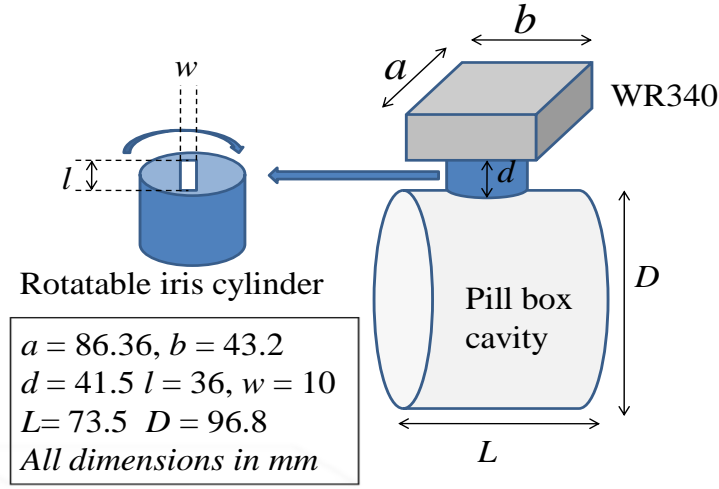


Fig. 3.11 Schematic of iris coupled waveguide-cavity system.

3.4.1.1 Magnetic Polarizability of Oriented Rectangular Iris

Iris oriented at angle ' θ ' in the plane of incoming waveguide is shown in Fig. 3.12. The incoming waveguide cross-section is shown in x-y co-ordinates whereas rotated iris is shown in u-v co-ordinate system. Iris is rotated by an angle ' θ ' w.r.t the x-y plane of incoming waveguide. Iris depth is not shown in Fig. 3.12. Electric and magnetic fields of pill-box cavity's TM_{010} mode are shown as \mathbf{E} and \mathbf{H} respectively.

As there is no electric field perpendicular to iris plane, we will consider magnetic polarizability only. Magnetic polarizability ' P_{ml} ' of rectangular iris at zero angle (also called longitudinal polarizability) is given by a polynomial expression as [85]:

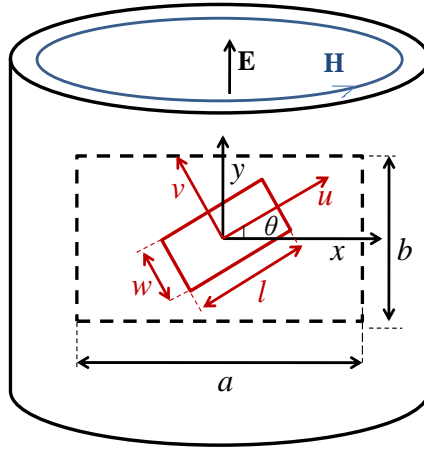


Fig. 3.12 Cross-section of incoming waveguide and rotated iris (in x-y and u-v coordinate systems respectively).

$$P_{m1} = f_1 l^3 \quad (3.3a)$$

$$f_1 = \frac{0.132}{\ln \left(1 + \frac{0.660}{(w/l)} \right)} \quad (3.3b)$$

where, ' l ' is iris length and ' w ' is iris width. Magnetic field orientation for longitudinal polarizability is shown in Fig. 3.13(a). The iris orientation for transverse polarizability is shown in Fig. 3.13(b).

Similarly, transverse magnetic polarizability of rectangular iris is given as [86]:

$$P_{m2} = f_2 l^3 \quad (3.4a)$$

$$f_2 = \frac{\pi}{16} \left(\frac{w}{l} \right)^2 \left(1.0 + 0.3221 \frac{w}{l} \right) \quad (3.4b)$$

Magnetic polarizability at an arbitrary angle can be defined by dyadic representation as [81]:

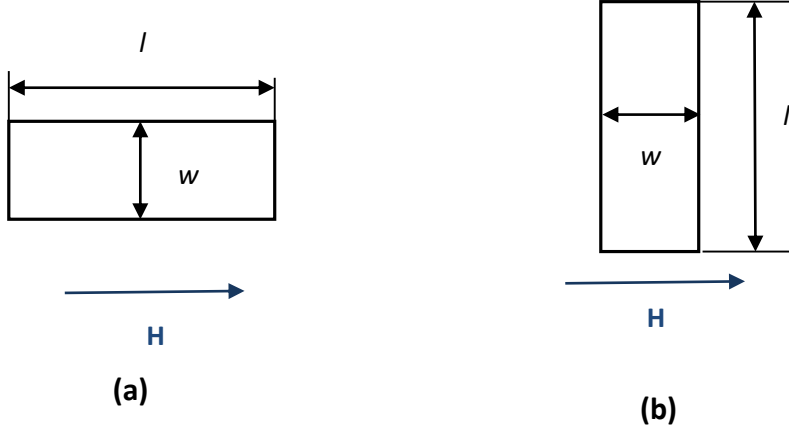


Fig. 3.13 Magnetic field and iris orientation for (a) longitudinal polarizability and (b) transverse polarizability.

$$\bar{P}_m = P_{m1} \mathbf{a}_u \mathbf{a}_u + P_{m2} \mathbf{a}_v \mathbf{a}_v \quad (3.5)$$

The vectors \mathbf{a}_u and \mathbf{a}_v are unit vectors in \mathbf{u} - \mathbf{v} plane. The \mathbf{a}_u is unit vector for \mathbf{u} axis and \mathbf{a}_v is unit vector for \mathbf{v} axis.

We will use this dyadic magnetic polarizability for external Q and coupling calculations using Bethe's original theory.

3.4.1.2 Analytical Expressions for External Q Calculations

The normalized fields for TE₁₀ mode of rectangular waveguide are given as [82]:

$$\mathbf{E}_{10}^+ = \mathbf{e}_{10} e^{-j\beta z} \quad (3.6a)$$

$$\mathbf{H}_{10}^+ = (\mathbf{h}_{10} + \mathbf{h}_{z10}) e^{-j\beta z} \quad (3.6b)$$

$$\mathbf{E}_{10}^- = \mathbf{e}_{10} e^{j\beta z} \quad (3.6c)$$

$$\mathbf{H}_{10}^- = (-\mathbf{h}_{10} + \mathbf{h}_{z10}) e^{j\beta z} \quad (3.6d)$$

where,

$$\mathbf{e}_{10} = -jk_o Z_o N \sin(\pi x / a) \mathbf{a}_y \quad (3.7a)$$

$$\mathbf{h}_{10} = -j\Gamma_{10} N \sin(\pi x / a) \mathbf{a}_x \quad (3.7b)$$

$$\mathbf{h}_{z10} = \frac{N\pi}{a} \cos(\pi x / a) \mathbf{a}_z \quad (3.7c)$$

$$N = (-2 / (abk_o Z_o \Gamma_{10}))^{1/2} \quad (3.7d)$$

where, Z_o is the intrinsic impedance of free space, k_o is free space propagation constant and Γ_{10} is the waveguide propagation constant. For all field equations discussed here, time dependence is not explicitly shown.

Let us assume that cavity's magnetic field at aperture location is \mathbf{H} . It is also assumed that cavity field is aligned with x-axis on the aperture surface. Magnetic moment (\mathbf{M}) produced by dyadic magnetic polarizability can be written as [80]:

$$\mathbf{M} = \bar{\mathbf{P}}_m \cdot \mathbf{H} \quad (3.8a)$$

After replacing polarizability value from eqn. (3.5) into eqn. (3.8a), we get

$$\mathbf{M} = \left(P_{m1} \mathbf{a}_u \mathbf{a}_u + P_{m2} \mathbf{a}_v \mathbf{a}_v \right) H \mathbf{a}_x \quad (3.8b)$$

After simplification, eqn. (3.8b) becomes:

$$\mathbf{M} = \left(P_{m1} \cos \theta \mathbf{a}_u + P_{m2} \sin \theta \mathbf{a}_v \right) H \quad (3.8c)$$

This means that cavity field is effectively splitting to two orthogonal polarizations in the rotated iris. In u-v coordinate system, ‘u’ polarization couples to cavity field magnitude of $H \cos \theta$ whereas ‘v’ polarization to field magnitude of $H \sin \theta$.

This magnetic dipole will radiate into the incoming waveguide. The induced magnetic field (H_o) in the incoming waveguide’s cross-section can be written as [81-83]:

$$H_o = (j\omega\mu_o \mathbf{H}_{10}^+ \cdot \mathbf{M}) \mathbf{H}_{10}^- \cdot \mathbf{a}_x \quad (3.9a)$$

The above expression reduces to

$$H_o = (j\omega\mu_o h_{10}^2) \mathbf{M} \cdot \mathbf{a}_x \quad (3.9b)$$

After substituting eqn. (3.7b) into above equation, it reduces to

$$H_o = \frac{-2j\Gamma_{10} \mathbf{M} \cdot \mathbf{a}_x}{ab} \quad (3.9c)$$

After replacing magnetic moment’s value from equation (3.8c) into eqn. (3.9c), we obtain

$$H_o = \frac{-2j\Gamma_{10} \left(P_{m1} \cos \theta \mathbf{a}_u \cdot \mathbf{a}_x + P_{m2} \sin \theta \mathbf{a}_v \cdot \mathbf{a}_x \right) H}{ab} \quad (3.10)$$

The H_o is \mathbf{x} component of waveguide’s maximum magnetic field .

After simplification, eqn. (3.10) reduces to:

$$H_x = \frac{-2j\Gamma_{10} \left(P_{m1} \cos^2 \theta + P_{m2} \sin^2 \theta \right) H}{ab} \quad (3.11)$$

Corresponding maximum electric field E_y at the center of waveguide can be obtained from waveguide impedance (Z_{TE}) given below [88]:

$$Z_{TE} = \frac{E_y}{H_x} = \frac{k_o Z_o}{\Gamma_{10}} \quad (3.12)$$

With the information obtained so far, the average power radiated into the waveguide can be calculated as [88]:

$$P_{rad} = \frac{E_y H_x ab}{4} \quad (3.13a)$$

Power radiated into the waveguide can also be written as

$$P_{rad} = \frac{H_x^2 ab Z_{TE}}{4} \quad (3.13b)$$

From eqns. (3.11), (3.12) and (3.13b), we get

$$P_{rad} = \frac{\Gamma_{10} k_o Z_o \left(P_{m1} \cos^2 \theta + P_{m2} \sin^2 \theta \right)^2 H^2}{ab} \quad (3.13c)$$

External quality factor (Q_{ext}) can be written as

$$Q_{ext} = \frac{\omega_o U}{P_{rad}} \quad (3.14a)$$

where, ω_o is resonance frequency and U is energy stored in cavity.

After placing eqn. (3.13c) into eqn. (3.14a), we obtain

$$Q_{ext} = \frac{\omega_o Uab}{\Gamma_{10} k_o Z_o H^2 (P_{m_1} \cos \theta^2 + P_{m_2} \sin \theta^2)^2} \quad (3.14b)$$

This expression is obtained for zero iris thickness. For iris of thickness d , an attenuation term is included for the magnetic field [12, 87]. If α is attenuation coefficient of dominant TE₁₀ mode of rectangular iris, eqn. (3.14b) can be written for iris of finite thickness as

$$Q_{ext} = \frac{\omega_o Uab}{\Gamma_{10} k_o Z_o H^2 \exp^{(-2\alpha d)} (P_{m_1} \cos \theta^2 + P_{m_2} \sin \theta^2)^2} \quad (3.14c)$$

Intrinsic quality factor (Q_o) of the resonator can be written as

$$Q_o = \frac{\omega_o U}{P_o} \quad (3.15)$$

where, P_o is the power dissipated on the cavity walls. Coupling coefficient ' β ' can be calculated as:

$$\beta = \frac{Q_o}{Q_{ext}} \quad (3.16a)$$

After using eqns. (3.14c) , (3.15) and (3.16a), we get

$$\beta = \frac{\Gamma_{10} k_o Z_o \exp^{(-2\alpha d)} (P_{m1} \cos^2 \theta + P_{m2} \sin^2 \theta)^2 H^2}{abP_o} \quad (3.16b)$$

After simplification, (3.16b) can be written as

$$\beta = \left(\sqrt{\beta_1} \cos^2 \theta + \sqrt{\beta_2} \sin^2 \theta \right)^2 \quad (3.16c)$$

where,

$$\beta_1 = \frac{\Gamma_{10} k_o Z_o \exp^{(-2\alpha d)} (P_{m1})^2 H^2}{abP_o} \quad (3.16d)$$

$$\beta_2 = \frac{\Gamma_{10} k_o Z_o \exp^{(-2\alpha d)} (P_{m2})^2 H^2}{abP_o} \quad (3.16e)$$

From eqn. (3.16c), we can observe that the coupling contributions from longitudinal and transverse polarizabilities get combined to produce the overall coupling. The contribution from longitudinal coupling is given in eqn. (3.16d) whereas the contribution from transverse coupling is shown in eqn. (3.16e).

3.4.1.3 Special Cases

Elliptical iris

Magnetic polarizability of elliptical iris with magnetic field parallel to longer dimension (i.e longitudinal polarizability) is given as [80]:

$$P_{m1} = \frac{\pi l_1^3 e_o^2}{3(K(e_o) - E(e_o))} \quad (3.17)$$

Here, l_1 is semi-major axis of ellipse and l_2 is semi-minor axis. $K(e_o)$ and $E(e_o)$ are elliptic integrals of first and second orders, respectively. Eccentricity ' e_o ' is given as:

$$e_o = \sqrt{1 - \frac{l_2^2}{l_1^2}} \quad (3.18)$$

As a special case, for zero degree iris orientation, eqn. (3.14c) reduces to

$$Q_{ext1} = \frac{\omega_o Uab}{\Gamma_{10} k_o Z_o \exp^{(-2\alpha d)} H^2 P_{m1}^2} \quad (3.19)$$

From eqns. (3.16a), (3.17) and (3.19), we get

$$\beta_1 = \frac{\Gamma_{10} k_o Z_o \pi^2 \exp^{-2\alpha d} l_1^6 e_o^4 H^2}{9ab(K(e_o) - E(e_o))^2 P_o} \quad (3.20)$$

This equation is same as that reported in [12]. Transverse coupling value has been obtained by same procedure. This is a validation of proposed expressions.

Circular iris

Coupling for circular iris with radius ‘ r ’ can be obtained by similar procedure. The magnetic polarizability of circular iris is given as

$$P_{m1} = \frac{4r^3}{3} \quad (3.21)$$

As circle is azimuthally symmetrical, coupling for zero and 90 degrees is same. Due to this fact, eqn. (3.16c) can be written as

$$\beta = \left[\sqrt{\beta_1} \left(\cos^2 \theta + \sin^2 \theta \right) \right]^2 \quad (3.22a)$$

After simplification, eqn. (3.22a) reduces to:

$$\beta = \beta_1 \quad (3.22b)$$

This implies that coupling for circular iris remains constant with iris rotation in the plane of incoming wave-guide cross-section. This result is quite logical and thus validates the proposed theoretical procedure.

Square iris

For a square iris also, the coupling for zero and 90 degrees iris orientation will be the same. This happens because the longitudinal and transverse polarizability values are same owing to equal arm lengths [85, 86]. Hence, we will get the same result as that of eqn. (3.22b). This implies that coupling for square iris should remain constant with iris rotation. However, there is about $\pm 10\%$ variation in the beginning and end of rotation range for square iris. This is attributed to the fact that square iris simulated in Section 3.3 is conformal to the cavity surface. Because of curved nature of cavity surface, effective iris thickness changes during its rotation range. Other factor causing the small variation in coupling of square iris can be field non-uniformity at waveguide end. For large apertures, the non-uniform nature of waveguide's TE_{10} fields leads to errors as proposed theory assumes uniform field.

Rectangular iris with low aspect ratio ($w/l \ll 1$)

For rectangular iris with small aspect ratio, it is noticed that transverse coupling is several orders of magnitude lower than longitudinal coupling ($\beta_2 \ll \beta_1$). This happens because of lower polarizability ($P_{m2} \ll P_{m1}$) and higher attenuation in transverse slot. Hence, after neglecting the contribution of transverse term, eqns. (3.14c) and (3.16c) can be written as:

$$Q_{ext} = \frac{\omega_o U a b}{\Gamma_{10} k_o Z_o \exp^{(-2\alpha d)} H^2 P_{m1}^2 \cos^4 \theta} \quad (3.23)$$

$$\beta(\theta) = \left(\sqrt{\beta_1} \cos^2 \theta \right)^2 = \beta_1 \cos^4 \theta \quad (3.24)$$

3.4.2 EM design of rotated iris and S- band cavity

As the resonance frequency of the structure is known analytically, we need the value of maximum magnetic field H on cavity surface. The maximum magnetic field on cavity surface for 1 J of energy stored can also be obtained analytically for a pill box cavity. All other parameters required for Q_{ext} calculations from eqn. (3.14c) are known analytically.

As practical structures are complex, EM modal solver run is used to get the value of H for 1 J of energy stored. This value for the structure under consideration is found to be 65000 A/m from CST-MWS. From this H value, Q_{ext} can be obtained for any iris orientation from eqn. (3.14c).

Further, if intrinsic quality factor is known, coupling coefficient can be obtained by simply dividing it with Q_{ext} . By using H , ω_o and P_o values from one modal solver run, we could calculate Q_{ext} and β for any arbitrary iris orientation. The Q_{ext} values obtained from eqn. (3.14c) and β values from eqn. (3.14) are compared with simulated and measured values. The comparison is discussed in next section.

A cylindrical cavity is modeled using CST-MWS. The analytical value of resonance frequency for the cavity dimensions given in Fig. 3.12 comes out to be 2.373 GHz. The simulated value of resonance frequency for TM_{010} mode is 2.36 GHz. Slight decrease in simulation values is because the RF port, iris and incoming waveguide are also included in the simulation. The extra magnetic volume introduced by the iris and waveguide results in lower frequency in simulated model. The coupler- cavity simulation model is shown in Fig. 3.14. For each Eigen Mode solver run of CST MWS, iris is rotated in the plane of incoming WR340 waveguide. Conducting boundary with σ (conductivity) = 5.8×10^7 S/m is used. Intrinsic quality factor of approx. 22,000 is obtained during simulations for the entire rotation range. External Q value is obtained from the

CST-MWS Modal Solver for every 15 degrees iris rotation by defining a matched boundary at waveguide port.

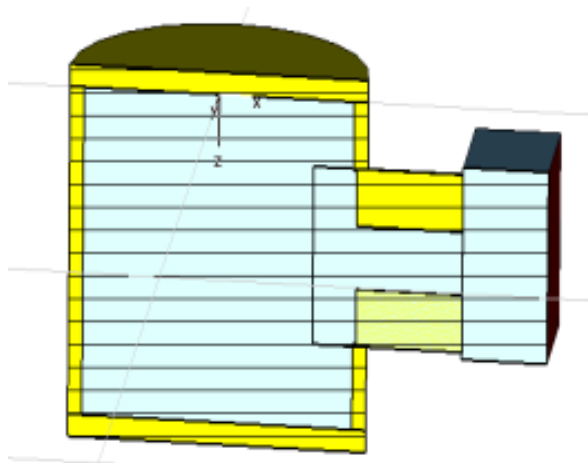
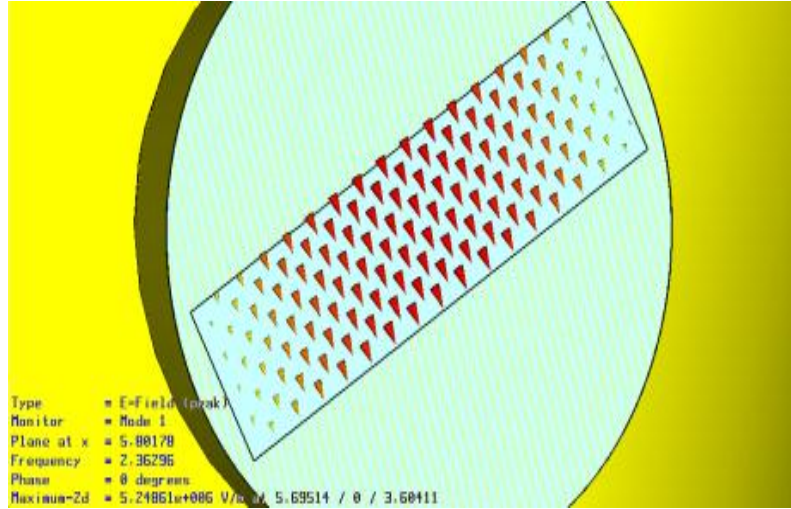
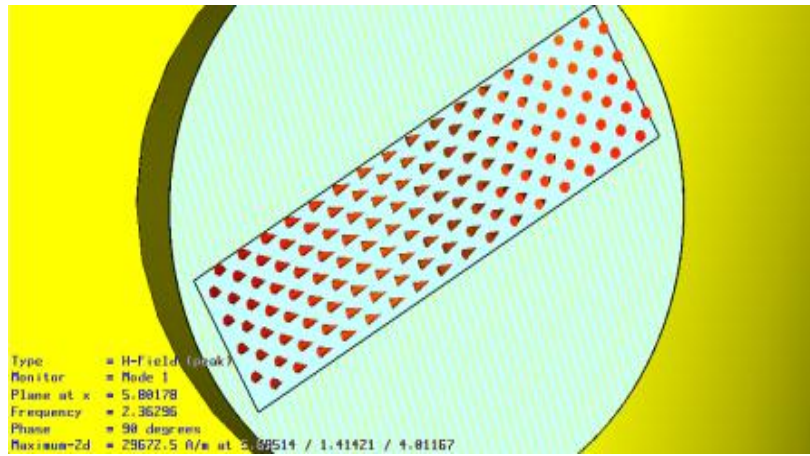


Fig. 3.14 Cut-view of simulation model for iris coupled cavity.

In order to have a better view of fields in the rotated iris, arrow plots of simulated \mathbf{E} and \mathbf{H} fields are shown in Figs. 3.15(a) and (b), respectively. Full wave simulations are performed for rectangular, elliptical, square and circular iris shapes. As shown in Fig. 3.12, rectangular iris of length 36 mm and width 10 mm is chosen. To keep the sizes comparable, elliptical iris with major axis of 36 mm and minor axis of 10 mm is considered. Similarly, diagonal of square iris and diameter of circular iris are chosen to be 36 mm.



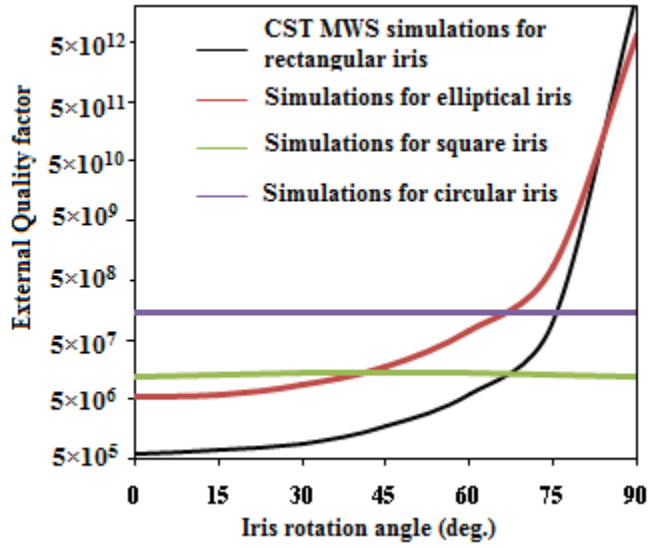
(a)



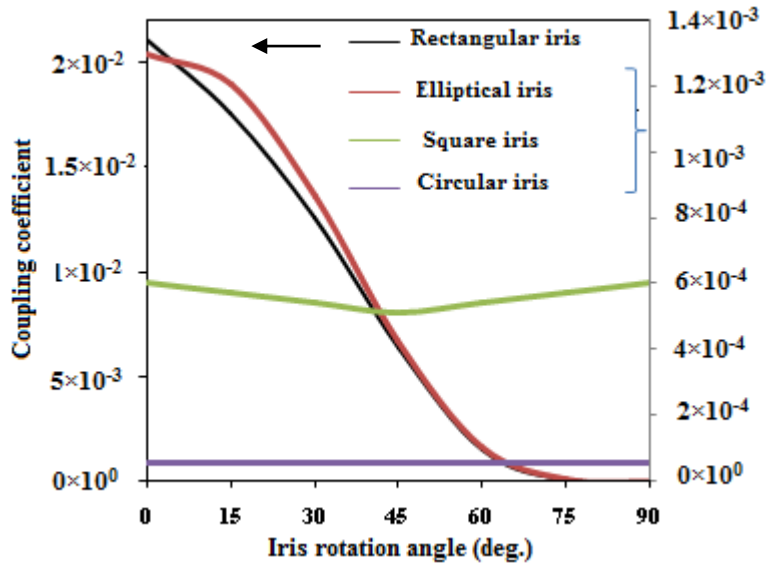
(b)

Fig. 3.15 Simulated arrow plots of (a) Electric field and (b) Magnetic field in the rotated iris.

The plots for variation of External Q with iris rotation are given in Fig. 3.16(a). It should be noted that External Q is plotted on log scale because of several orders of variation over the rotation range. Coupling coefficient variation with rotation angle is shown in Fig. 3.16(b). The rectangular iris is plotted on the left scale whereas other iris shapes are plotted on the right scale because of orders of magnitude difference in coupling values.



(a)



(b)

Fig. 3.16 CST Simulation results for (a) External Q and (b) coupling coefficient for different iris shapes.

We can observe from these plots that square and circular irises give very low coupling as compared to rectangular and elliptical irises. Moreover, square and circular irises are not useful

for rotatable iris based coupling variation schemes as there is practically no coupling variation over the entire rotation range. The rectangular iris gives more coupling than elliptical iris for chosen dimensions. Hence, we chose rectangular iris for validation with measurements as it provides more coupling, wide range and is easier to fabricate. However, elliptical, square and circular iris coupling simulations from CST-MWS are compared with proposed formulae and a close match is found as shown in Fig. 3.17.

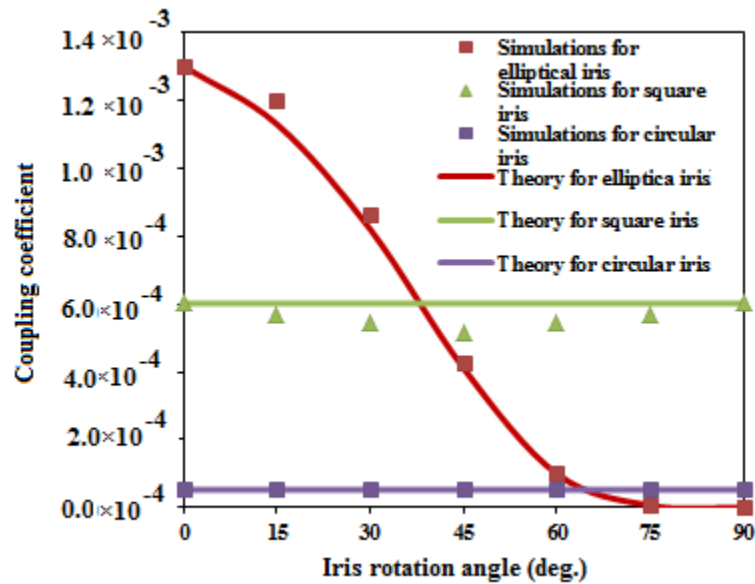


Fig. 3.17 Comparison of CST Simulation results with theoretically calculated values for different iris shapes.

3.4.3 Measurements for External Q and coupling coefficient

The coupler parts and fabricated cavity are shown in Figs. 3.18(a) and (b), respectively. The incoming waveguide port from WR340 to N Type adapter is blocked with a stainless steel (SS) flange. The SS flange has a provision for mounting the iris at the center. The iris part can be rotated with respect to the waveguide cross-section. The SS flange is also provided with holes so that it can be mounted on to the cavity port. Cavity port diameter is 40 mm. The cavity, ports and iris are made with SS and plated with Cu to have good quality factor.



(a)



(b)

Fig. 3.18 The pictures of (a) Iris cylinder with rectangular iris and (b) cavity connected to VNA through WR340- N Type adapter and auxiliary port for transmission measurements.

To measure the coupling with transmission method [17], a small port of 10 mm diameter is provided on the cavity. A small loop made of an N Type connector is mounted on this auxiliary port. WR340 to N Type adapter is used to feed the microwave power to WR340 waveguide. Measurements are performed with Vector Network Analyzer (VNA) of R&S ZVB4 series.

The coupling coefficient of auxiliary loop coupled cavity can be written as:

$$\beta_a = \frac{R}{Z_o} \quad (3.25a)$$

where, R is the impedance of cavity at resonance and Z_o is 50 Ohms. The reflection coefficient of coupled cavity at resonance is given as:

$$S_{11} = \frac{\frac{R}{Z_o} - 1}{\frac{R}{Z_o} + 1} \quad (3.25b)$$

A reflection measurement (S_{11}) at auxiliary port is used to calculate the coupling coefficient from eqns. (3.25a) and (3.25b).

From measured S_{11} of 15 dB, coupling of auxiliary loop (β_a) is found to be 0.7. The relevant equations for Q_o and Q_{ext} calculations from measurements are given as [17]:

$$Q_o = Q_L (1 + \beta_a + \beta_{ex}) \quad (3.26a)$$

$$Q_{ext} = \frac{4\beta_a Q_L}{1 + \beta_a} 10^{|S_{21}|_{dB}/10} \quad (3.26b)$$

Loaded quality factor Q_L is obtained from transmission measurements using 3 dB method. Q_o of fabricated cavity is calculated to be 7219 using eqn. (3.26a). As found from reflection measurements, coupling coefficient of iris coupled waveguide to cavity system (β_{ext}) is very low and hence neglected for calculating Q_o from eqn. (3.26a). For each measurement, iris coupler is rotated and corresponding transmission magnitude is noted. Finally, unknown Q_{ext} and coupling coefficient are calculated from eqns. (3.26b) and (3.16a) respectively.

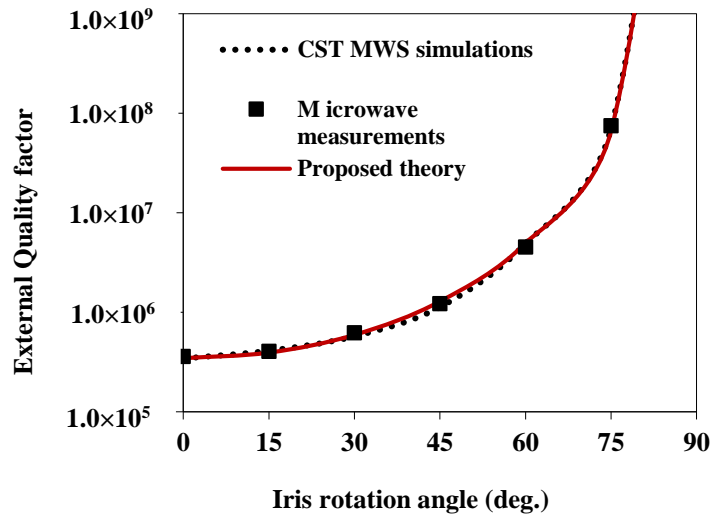
The external Q and coupling coefficient values are obtained from measurements and compared with simulations and theoretically calculated values. For coupling coefficient calculations, measured value of Q_o is used for comparative analysis.

The plots for external Q and coupling coefficient variation with iris rotation are shown in Figs. 3.19(a) and (b), respectively. A close agreement is found between simulations, measurements and proposed theory. Maximum mismatch between theoretical and measured values as compared to simulations is found to be less than 10%.

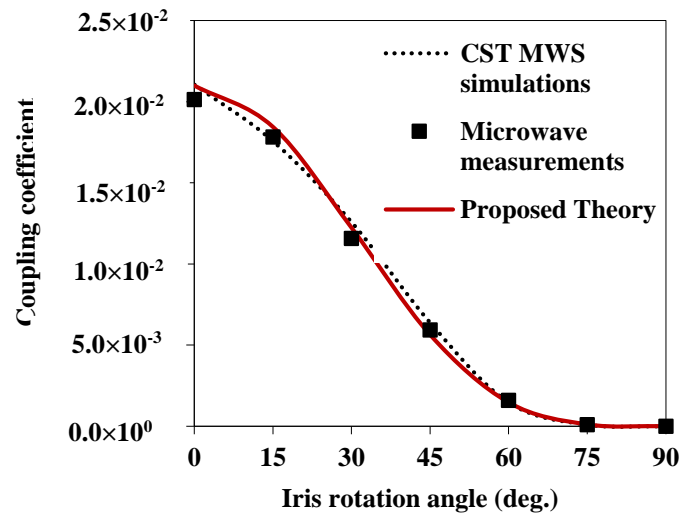
The possible sources of measurement errors and uncertainties are: The external Q measurements are very sensitive to S_{21} magnitude especially at higher angles (because of very weak coupling). This error is found to be around 3-4% at higher angles with ± 0.1 dB change in S_{21} magnitude. The angle of iris rotation was adjusted within accuracy of ± 1 degree during measurements. The dimensional accuracy of fabricated components was within ± 100 microns. The coupling is highly sensitive to iris length and can result in around 1.5-2% change of coupling for said tolerances. The cavity surface is not exactly planar at iris interface as assumed in proposed theory. All of these factors may be responsible for difference in theoretical, simulated and measured results.

3.4.4 Practical aspects of rotated iris couplers

Like any other coupling scheme, iris rotation based coupling will need to address challenges like sufficient coupling with given depth of iris cylinder and RF losses in the iris. Also, resonance frequency changes and possible enhancement of fields in rotated iris positions needs to be carefully evaluated.



(a)



(b)

Fig. 3.19 Variation of (a) External Q (b) coupling coefficient of simulated, measured, and proposed analytical results for different rotation angle of rectangular iris.

Vacuum sealing for various rotated iris positions can be provided with rotatable flange and conflate or helicon-flex seals. The iris can be manually rotated during low power testing for desired coupling and then vacuum sealed for high power operation. Dynamic rotation of iris with vacuum seal will need complex mechanical design but static iris rotation can be implemented as

is done in coaxial loop couplers. Studies to address these problems in iris rotation based couplers are discussed here.

3.4.4.1 Increasing the coupling for given iris depth

The rotatable iris coupler discussed in Sections 3.4.2 and 3.4.3 used a rectangular iris. The choice of rectangular iris shape is made because of its simplicity and regular use in accelerator cavities. However, for the considered S- band waveguide-cavity system, coupling coefficient obtained with rectangular iris is very small. Hence, its applicability to practical couplers for accelerator cavities may need modifications. There is extensive literature available on the slot/iris/aperture coupling in the context of antenna and shielding. For example, different slot shapes have been compared for their coupling strength in the context of antennas in [89]. Coupling through apertures for shielding effectiveness has been reported in [90]. The coupling coefficient is proportional to ' $\exp(-2\alpha d)$ ' where ' α ' is attenuation constant and ' d ' is iris depth [11]. The iris depth can not be decreased beyond a point because of finite port depth and flange thickness. This limitation exists in practically any type of iris coupler. The constraints on depth are compensated by increasing the iris length in traditional iris couplers. However, iris length of rotatable iris can not be increased beyond a point as it has to fit in the incoming waveguide cross-section throughout its rotation range. Hence, other iris shapes were explored for increasing the coupling coefficient to desired value without changing the overall length, height and depth of iris cylinder. This is achieved by decreasing the attenuation constant ' α ' of the iris. One way of decreasing α is to include a ridge waveguide type iris. By introducing the double ridge at the center of rectangular iris, the attenuation coefficient can be sufficiently decreased to get the required coupling coefficient. The dog-bone shaped iris for increasing the coupling coefficient is also

considered. The dimensions of the iris cross-section and depth are chosen in such a way so that they can fit into the given iris cylinder. The cross-sections of iris shapes are shown in Fig. 3.20.

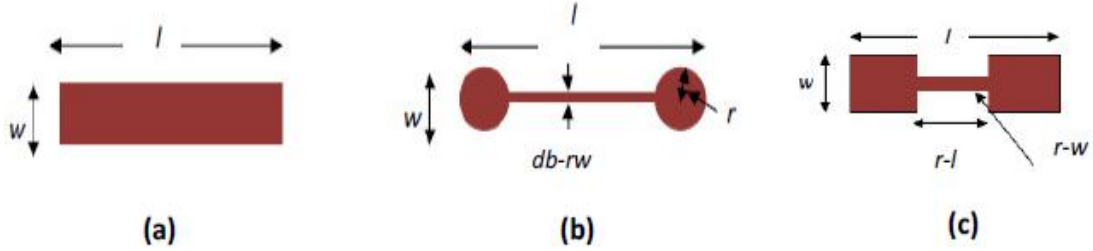


Fig. 3.20 Iris shapes considered (a) rectangular iris; (b) dog-bone shaped iris and (c) rectangular ridge type iris.

The overall dimensions for all these iris shapes are kept same i.e. $l = 36$ mm and $w = 10$ mm. The depth for all above irises is equal ($d = 38.3$ mm) and same as that considered in Sections 3.4.2 and 3.4.3. Ridge length ($r-l$) is half of total length (l). Ridge width of rectangular ridge ($r-w$) and dog bone shape ($dg-w$) are varied from 2.5 mm to 3 mm to evaluate coupling coefficient values for different gaps. The radius (r) of both circular holes is 5 mm.

A numerical study is carried out using Eigen Mode solver of CST-MWS to evaluate the coupling coefficient variation with ridge width. The values of coupling with ridge width changes are shown in Fig. 3.21 (a). Coupling coefficient variation with length for rectangular iris is shown in Fig. 3.21 (b). The ridge iris and dog-bone shaped iris provide higher coupling by decreasing their ridge width. However, for rectangular iris, critical coupling is obtained for iris length of 49 mm which is too long to be fitted into rotatable iris cylinder under consideration. Hence, ridge and dog-bone shaped irises will be suitable choices for rotation type iris couplers as they can provide

higher coupling within the given size constraints. It is important to note that coupling coefficient values for rectangular iris are more than two orders of magnitude lower than other two iris shapes.

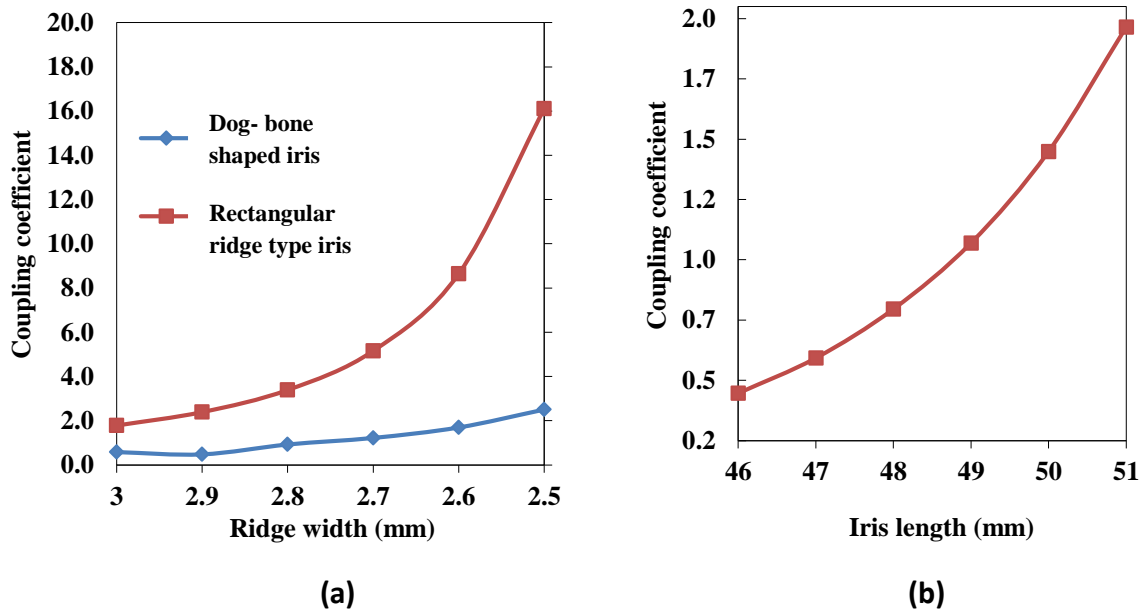


Fig. 3.21 Coupling coefficient variation for (a) rectangular ridge and dog-bone shaped iris and (b) for rectangular iris.

3.4.4.2 RF Losses and resonant frequency variation

The iris region generally experiences more RF losses than other coupler parts as it is exposed to high cavity magnetic fields. This is true for both rotatable and non rotatable iris couplers. RF losses in iris cylinder and cavity resonant frequency with iris are evaluated using Eigen Mode solver of CST-MWS. The RF loss values obtained are based upon 1 J energy stored in the cavity. As an example of conventional coupler, rectangular iris is considered. In order to vary the

coupling from say 0.45 to 1.9, iris length needs to be increased from 46 mm to 51 mm. It can be seen from Fig. 3.22 that RF loss increases and resonance frequency decreases with increase in iris length for rectangular iris. This is expected because magnetic field entering into iris increases with iris length.

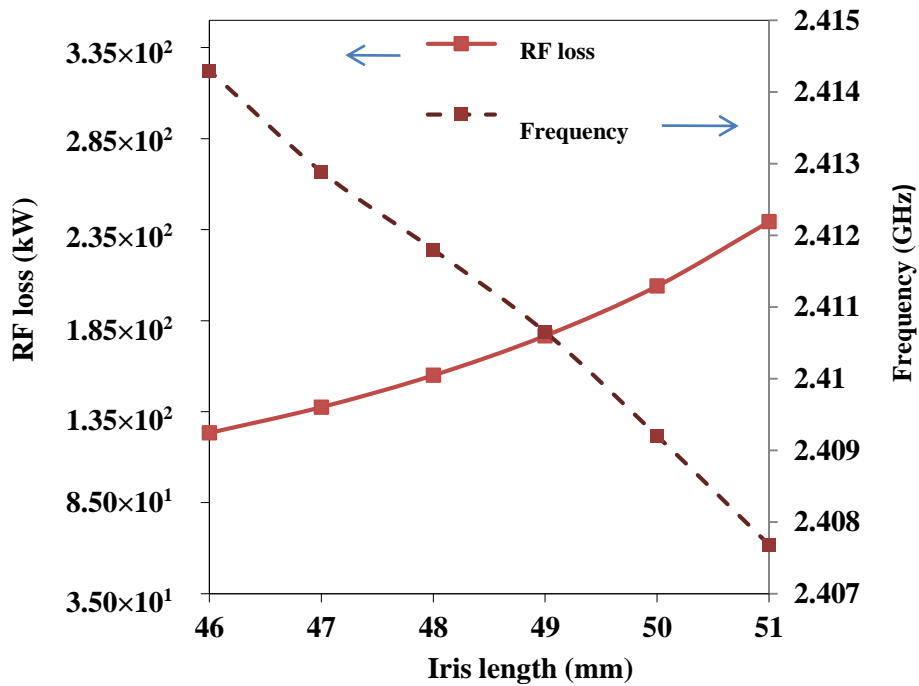


Fig. 3.22 RF loss and cavity resonance frequency variation with iris length of rectangular iris.

For rotatable iris coupler, results with iris rotation are shown in Fig. 3.23. The iris shapes are chosen in such a way, so that coupling value of more than 1.7 is obtained for 0 degree. It can be seen from Fig. 3.23 that RF loss decreases and cavity resonance frequency increases with iris rotation. This behavior is expected because lesser field enters into iris in rotated position.

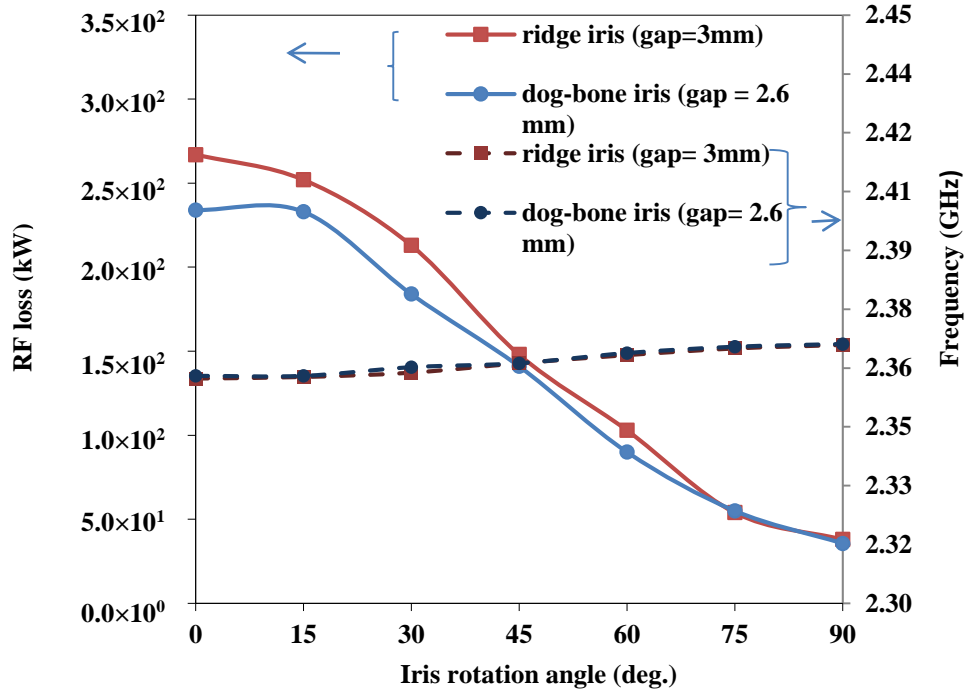


Fig. 3.23 Variation of RF losses and resonant frequency with iris rotation for different iris shapes.

Table 3.1 summarizes the comparison of different iris shapes in rotated and horizontal positions for RF losses, cavity frequency and maximum iris fields. For all the considered cases, coupling is kept around critical value.

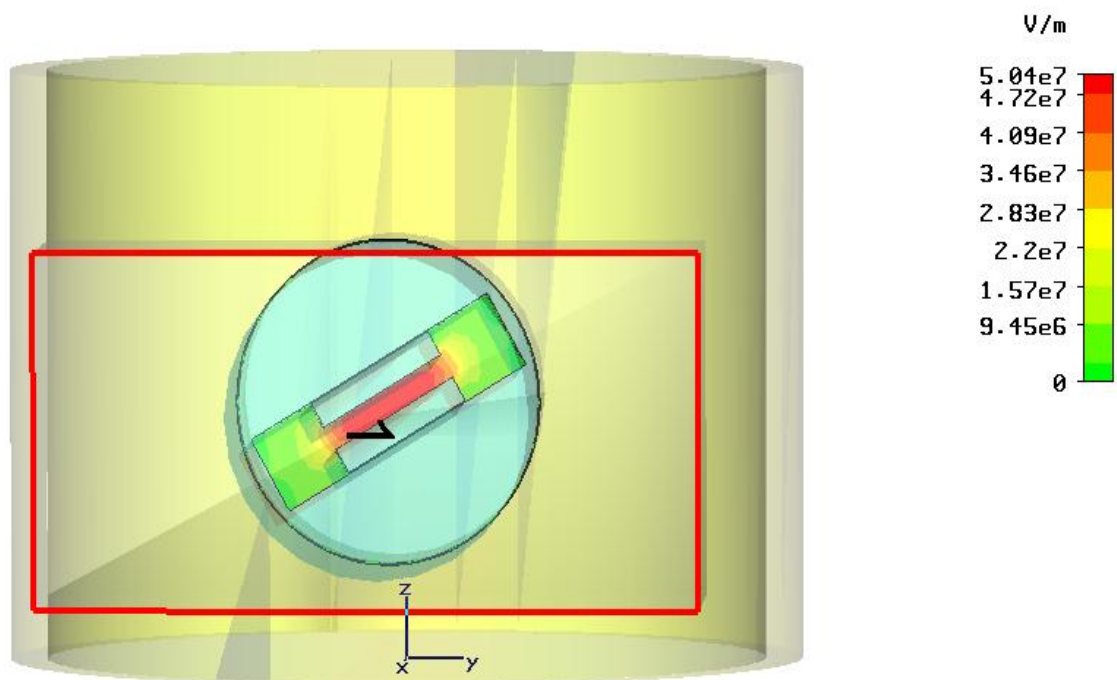
3.4.4.3 EM fields in rotatable iris coupler

As discussed in above section, ridge loaded and dog-bone iris shapes will be useful in rotatable iris couplers. Though the total iris loss does not increase significantly in these iris shapes as compared to rectangular iris of conventional couplers, it is important to evaluate the maximum electric and magnetic field values in the iris. It is found that there is local field enhancement near the sharp edges of iris. As can be noticed from Table 3.1, maximum magnetic field for rotated iris can become 1.25 times higher than rectangular iris.

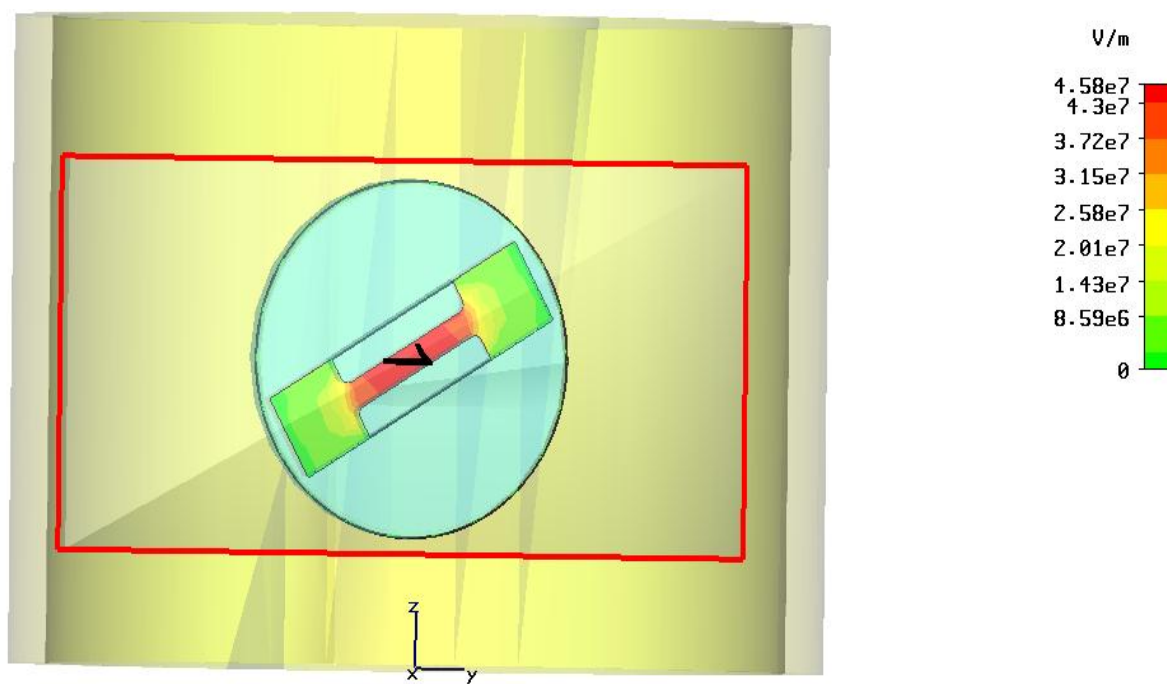
Table 3.1 Variation of coupling coefficient, RF loss, E and H fields for different iris shapes.

Type of iris	Dimensions (mm)	Angle (degree)	Coupling coeff. (for $Q_0=7219$)	RF loss on iris (W)	Freq. (GHz)	Max. Magnetic field (A/m)	Max. Electric field (V/m)
Rectangular ridge type	$l=36, w=10, r-w=3, r-l=18,$	30	0.98	2.18×10^5	2.3579	9.4×10^4	5.0×10^7
Dog-bone shaped iris	$l=36, w=10, db-w=2.6, r=5$	15	1.09	2.0×10^5	2.3582	9.0×10^4	7.0×10^7
Rectangular iris	$l=49, w=10$	0	1.02	1.77×10^5	2.4106	7.5×10^4	2.6×10^7
Rectangular ridge type	$l=36, w=10, r-w=3.2, r-l=18,$	0	1.09	2.09×10^5	2.3574	9.0×10^4	4.7×10^7
Dog-bone shaped iris	$l=36, w=10, db-w=2.8, r=5$	0	0.93	1.99×10^5	2.3581	9.3×10^4	4.8×10^7

However, maximum magnetic field values for rectangular ridge and dog-bone shaped irises without rotation are almost same as that of rotated iris for critical coupling. Maximum electric field can increase by 2.7 times for rotated dog-bone shaped iris as compared to rectangular iris. The rotation angles are decided so that critical coupling is obtained. The maximum electric field values for rectangular ridge and dog-bone shaped irises without rotation are approx. 1.85 times higher than rectangular iris. However, field enhancement can be decreased by corner rounding as can be seen from Figs. 3.24(a) and (b). The maximum electric field could be decreased from 5.04×10^7 V/m to 4.58×10^7 V/m by edge rounding of 1 mm radius.



(a)



(b)

Fig. 3.24 Electric field in the rotated iris (a) before corner rounding and (b) after corner rounding(1 mm radius).

The field enhancement values may limit the maximum power handling capabilities. The rounding of corners can be used to obtain maximum possible ratings. Following points are worth noting from Table 3.1.

- There is a marginal increase in RF losses for rectangular ridge and dog-bone shaped irises in rotated positions as compared to horizontal (i.e. non-rotated) position.
- RF losses are approximately 10% higher in rotatable iris coupler than conventional coupler using rectangular iris.
- Magnetic and Electric field enhancement take place in both rectangular ridge and dog-bone shaped irises as compared to rectangular iris. The field enhancement can be brought down by rounding the sharp corners.

3.5 SUMMARY

Concept of iris rotation is proposed by numerical studies on a 350 MHz cavity. Analytical expressions are derived for waveguide to cavity coupling with rotated rectangular iris. From proposed generalized expressions for arbitrary iris orientation, analytically known results for non-rotated elliptical iris could be obtained as a special case. Other iris shapes like square and circular are also analyzed with the proposed theory and simulations.

Keeping in view the smaller size, an S- band pill box cavity and rotated iris coupler are fabricated and microwave measurements are performed. The analytically calculated, simulated and measured values are in close agreement. With a suitably designed coupler with over coupling for an accelerator cavity, coupling can be brought down to the desired value by iris rotation. The EM analysis results for coupling, RF losses, frequency shift and local field enhancements are provided for different iris shapes. The RF losses of rotation based coupler for

critical coupling are comparable to conventional couplers with rectangular iris. However, field enhancements take place because of use of ridge type iris or dog-bone shaped irises. The field enhancements may be reduced using corner rounding. The results are validated with full wave simulations and measurements. These expressions will be useful in reducing the design time of RF couplers for accelerator cavities and other novel devices based upon rotated iris coupling. Proposed theoretical results will also be useful in establishing the coupling scaling laws for an iris at an arbitrary angle.

CHAPTER- 4

HIGH POWER RIDGE WAVEGUIDE COUPLERS

4.1 INTRODUCTION

As discussed in Chapter 1, high current proton accelerators with energies in GeV range are under development worldwide for various applications like accelerator driven systems and spallation neutron source. This has increased the power handling requirements of individual couplers. The coupler design starts with electromagnetic design, various other factors like thermal, fabrication, multipacting and RF conditioning are equally important. Excellent reviews on high power couplers and related challenges can be found in [91–94].

For 20 MeV, 30 mA proton accelerator LEHIPA (Low Energy High Intensity Proton Accelerator) at BARC, ridge waveguide iris couplers (250 kW, 352.2 MHz CW) are under development. However, ridge waveguide couplers require very strict dimensional tolerances during manufacturing [95]. Though three stub tuners or EH tuners can be used to correct the mismatches caused by dimensional changes [96], it requires one extra component in the form of tuner. A straight ridge matching section, which is similar to [97] is optimized for LEHIPA and considered here for tuning studies. This chapter addresses the issues of strict dimensional tolerances and coupling coefficient tuning. Tuners are proposed for the ridge waveguide transition. A lower effect of coupler dimensions on its performance is observed in iris coupled-cavity. It is demonstrated by simulations that same tuners can be used to tune the coupling

coefficient. Tuners will be cylindrical rods and can be machined to required dimensions during low power testing.

A comparative study is also carried out for linearly tapered ridge and straight ridge waveguide transition. It is found that the linearly tapered ridge is less sensitive to most of the dimensional changes as compared to the straight ridge taper. It is also shown that the linearly tapered ridge waveguide transition is superior to the straight ridge transition in terms of the return loss bandwidth, lower insertion loss, phase shift and the EM field concentrations. However, because of its simpler design and recently proposed tuning scheme to relax its dimensional tolerances in previous section, the straight ridge transition is also expected to be a good alternative.

Finally, two straight ridge waveguide couplers are fabricated and characterized by connecting them back to back. Tuners are shown to be effective in optimizing the required return loss at design frequency of 352.2 MHz.

4.2 DESCRIPTION OF A RIDGE WAVEGUIDE COUPLER

Waveguide coupler assembly consists of three sections. The incoming section is half height WR2300 waveguide followed by a $\lambda_g/4$ length double ridge waveguide, where λ_g is the waveguide wavelength. The output port is a double ridge waveguide of reduced dimensions. An iris section for coupling power to the cavity is designed and fabricated separately. The vacuum barrier is provided by a standalone window in WR 2300 half height size and hence not considered in this study. Fig. 4.1 (a) shows the coupler view from input port side and Fig. 4.1 (b) shows the coupler view from output ridge side. The waveguide impedances of all three sections are quite close. However, dimensions are optimized for good match at input port at the desired frequency of 352.2 MHz.

4.2.1. EM simulations of quarter wave matching section

The coupler is modeled in CST-MWS to obtain return loss of better than -30 dB at 352.2 MHz. A symbolic notation is used for various coupler dimensions. Top view of the coupler schematic is shown in Fig. 4.2 (a). The cavity is shown for completeness and is not included in the S parameter simulations. Fig. 4.2 (b) shows the cross-section view of coupler at different sections with symbolic notations. The simulation model is shown in Fig. 4.2 (c).

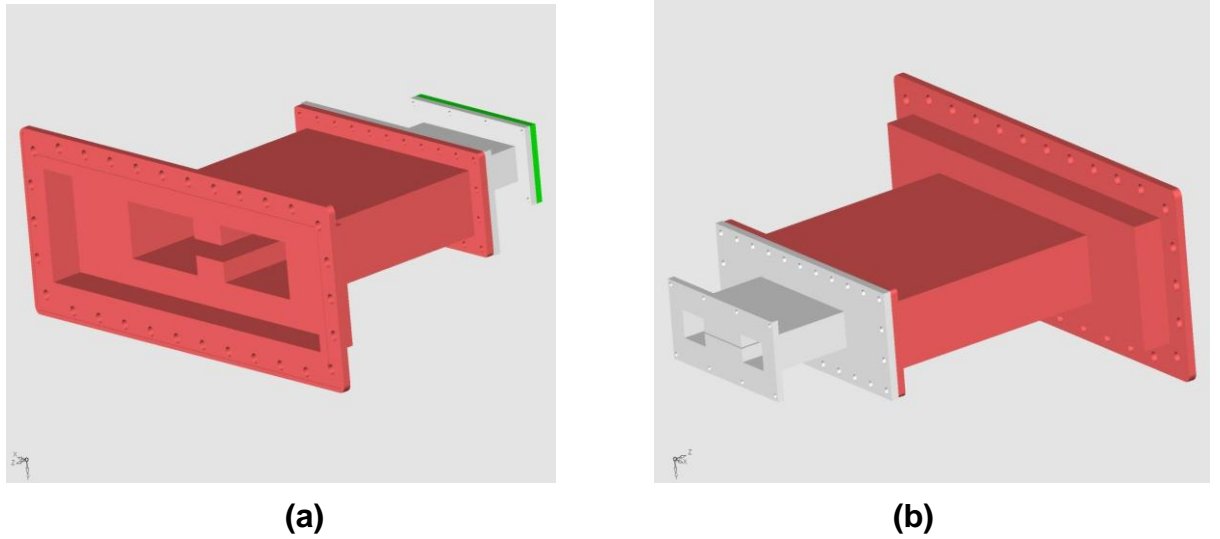


Fig. 4.1 Model of ridge waveguide coupler view from (a) WR2300 input port and (b) output ridge waveguide port.

For S parameter studies using transient solver, waveguide ports are defined at incoming WR2300 section and output double ridge waveguide. The structure is meshed with 25 points per wavelength. As the structure is symmetric in E and H plane, only 1/4th structure is simulated by defining E wall and H wall boundary conditions. This results in 16128 mesh points which is equivalent to 64512 mesh points on complete geometry. The S parameter results for the

optimized structure are shown in Fig. 4.2 (d). It can be noticed that return loss of better than -33 dB is obtained at 352.2 MHz. The dimensions of optimized geometry are listed in Table 4.1.

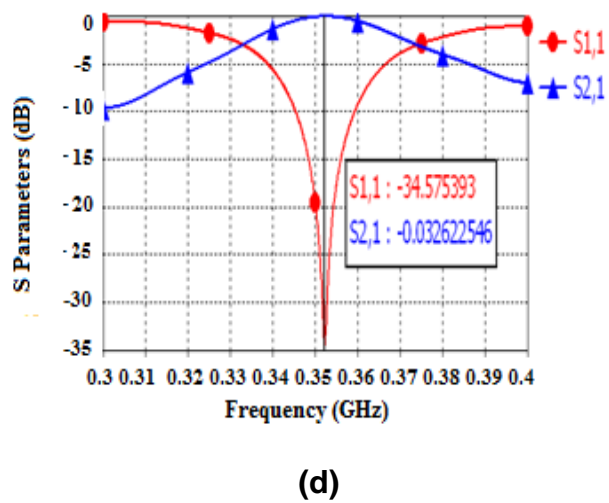
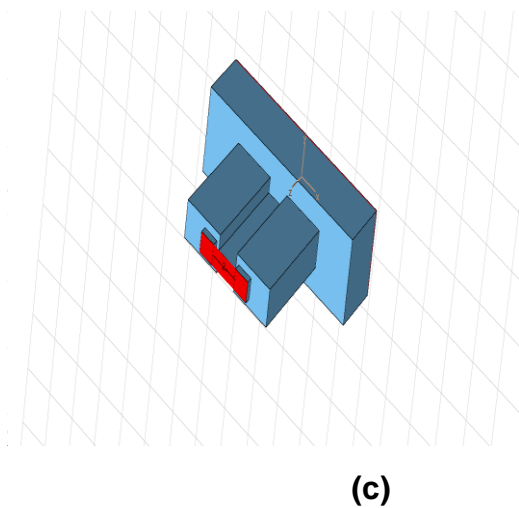
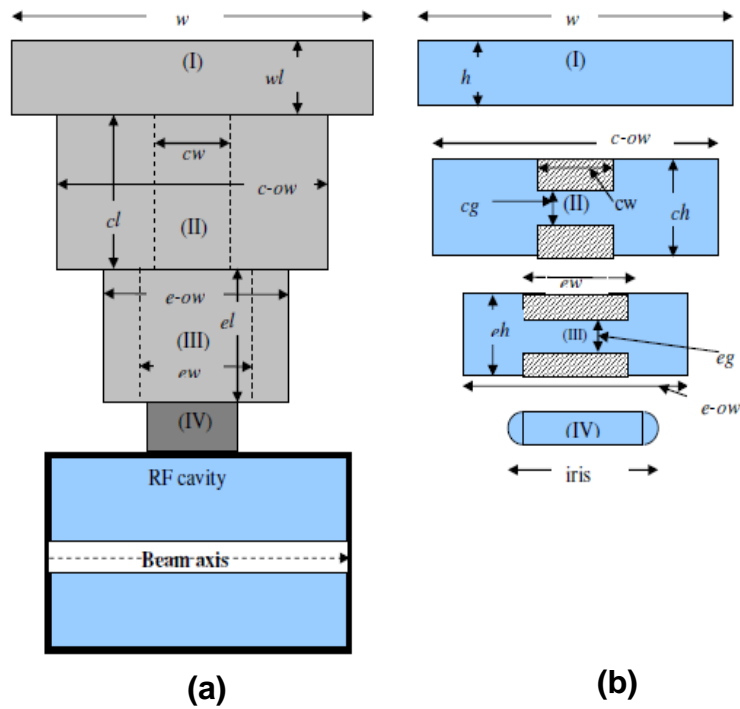


Fig. 4.2 Ridge waveguide coupler's (a) top view; (b) cross-section view; (c) 3D simulation model and (d) S_{11} and S_{21} parameters plot of coupler.

Table 4.1 Dimensions of optimized coupler parameters.

Parameter	Description	Value (mm)
w	WR2300 width	584.2
h	WR2300 height	146.05
wl	Input Port length	160
$c-ow$	Central section-overall width	334
cw	Central ridge width	69.4
cl	Central ridge length	315
cg	Central ridge gap	11.5
ch	Central ridge height	64
ew	End ridge width	89
$e-ow$	End section- overall width	189
eg	End ridge gap	1.55
eh	End ridge height	35
el	Output Port length	20

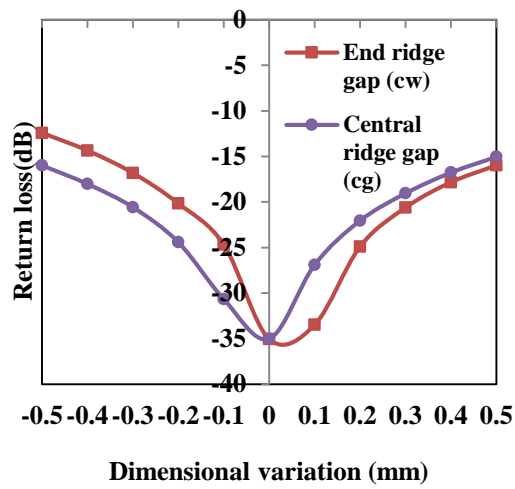
4.2.2 Dependence of return loss on dimensional tolerances

The dependence of resonance frequency and return loss of coupler on dimensional changes has been studied. Several simulations were made to understand the return loss sensitivity to various coupler dimensions. It is observed that S_{11} parameter is mainly sensitive to six lengths or gaps, namely end ridge gap, central ridge gap, central ridge length, central ridge width, central ridge overall width and central ridge height. The lengths are varied in 1.0 mm steps except for end ridge gap and central ridge gap where the variation step is 0.1 mm. The ridge gaps are given smaller steps of 0.1 mm because of their smaller lengths as compared to other coupler

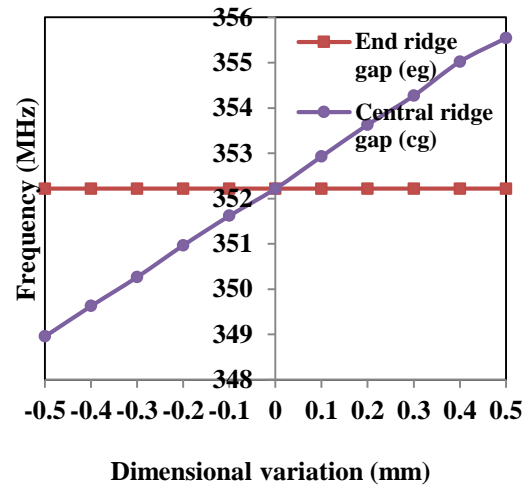
dimensions. Return loss value at design frequency of 352.2 MHz is noted down for each variation. The new resonance frequency of S_{11} parameter is also recorded for each variation step. The plots for variation of return loss at design frequency and shifted resonant frequency with dimensional changes are given in Fig. 4.3. The return loss results for end ridge gap and central section ridge gap are plotted in Fig. 4.3(a). The resonance frequencies for these gap values are shown in Fig. 4.3(b). It can be observed that return loss degrades to below -20 dB for a dimensional change of + 0.2 mm for end ridge gap and ± 0.4 mm for central ridge gap. This is because optimized end ridge gap is 1.55 mm where as central ridge gap is 11.5 mm. The sensitivity for end ridge gap dimensions is also expected because of high field concentrations in the output region. Also, return loss plot for end ridge gap variation is slightly non symmetric. This is because the optimum end ridge gap is slightly more than 1.55mm.

It can be noticed from Fig. 4.3(b) that there is no frequency shift for end ridge gap changes whereas a frequency shift of about ± 3.5 MHz is observed for central ridge gap changes. This happens because end ridge gap only changes the wave impedance of output port and hence the return loss. The central gap changes the capacitive ridge loading in the central matching section which is approximately quarter wave length long. The capacitive loading changes the guide wavelength. Hence more shift in frequency is observed for central ridge gap changes.

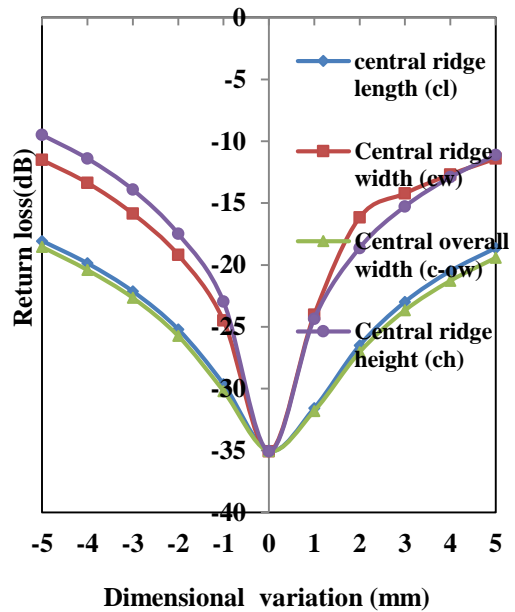
Return loss and frequency plots for other central matching section dimension changes (like central ridge length, central ridge width, central section overall width and central ridge height) are plotted in Figs. 4.3(c) and (d) respectively. The corresponding plots for remaining dimensions are given in Figs. 4.4(a) and (b). The remaining waveguide coupler dimensions are not very sensitive to dimensional changes.



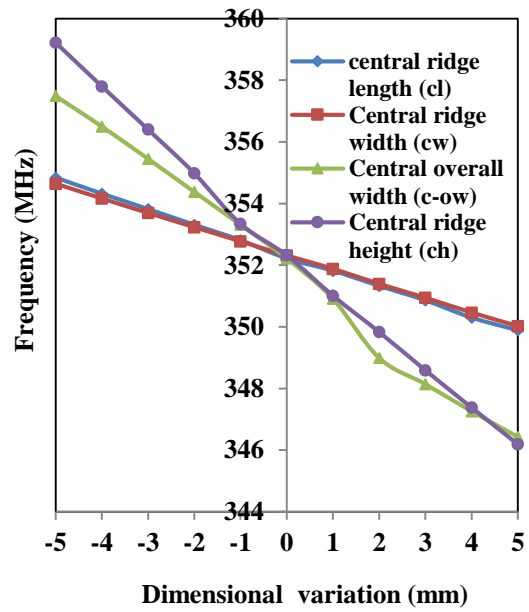
(a)



(b)



(c)



(d)

Fig. 4.3 Plot of (a) return loss at design frequency and (b) minimum return loss frequency for end gap and central gap; (c) return loss for central section length, central ridge width, central overall width and height and (d) variation of minimum return loss frequency for central ridge dimensions.

It can be observed from the plots of Fig. 4.3 that the central ridge section dimensions are quite sensitive to dimensional changes. This is expected because the quarter wave central matching

section acts as a $\lambda g/4$ transmission line resonator with openings at input and output for power transfer. The return loss sensitivity for central ridge overall width and length is less as compared to central ridge width and height. This is because optimized dimensions of central ridge with (69.4mm) and height (64mm) are less as compared to overall width (334mm) and length (315mm). This results in lower relative dimensional shift for ± 5 mm dimensional changes. It is observed from Fig. 4.3(b) that frequency shift for central ridge width and length is less as compared to other dimensions. This occurs because of the central matching section acts as a quarter wave matching resonator and its frequency dependence is decided by the field concentrations at various locations. A non-symmetric variation is also observed for end ridge gap and central ridge overall width. A possible explanation for this behavior may be that wave impedance of central matching section has a non linear dependence on its widths.

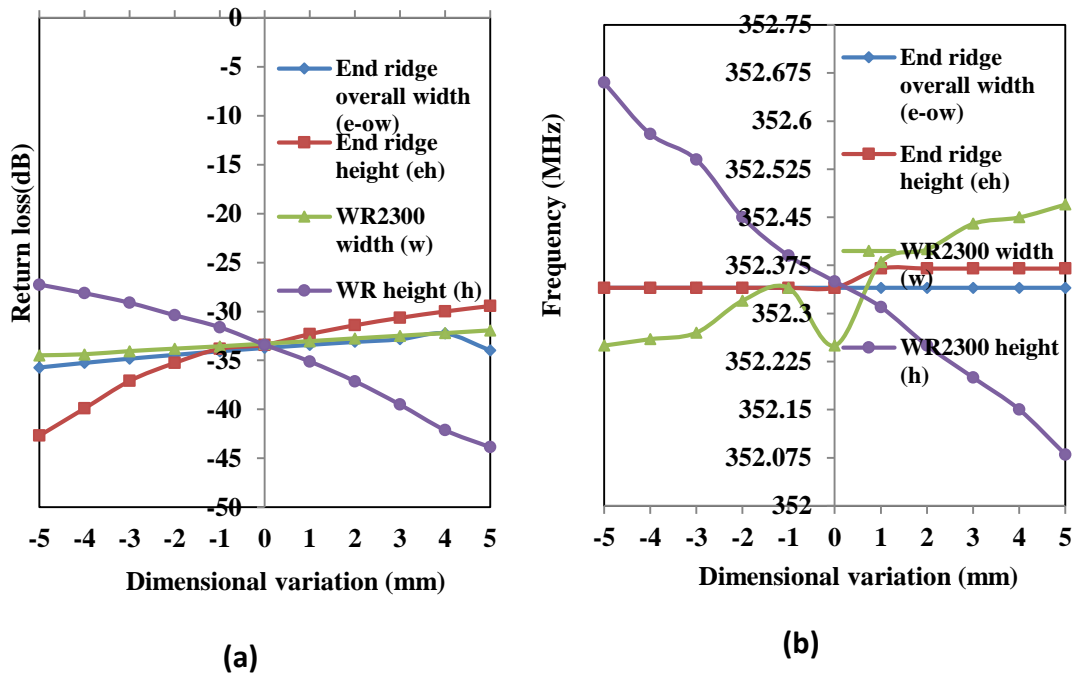


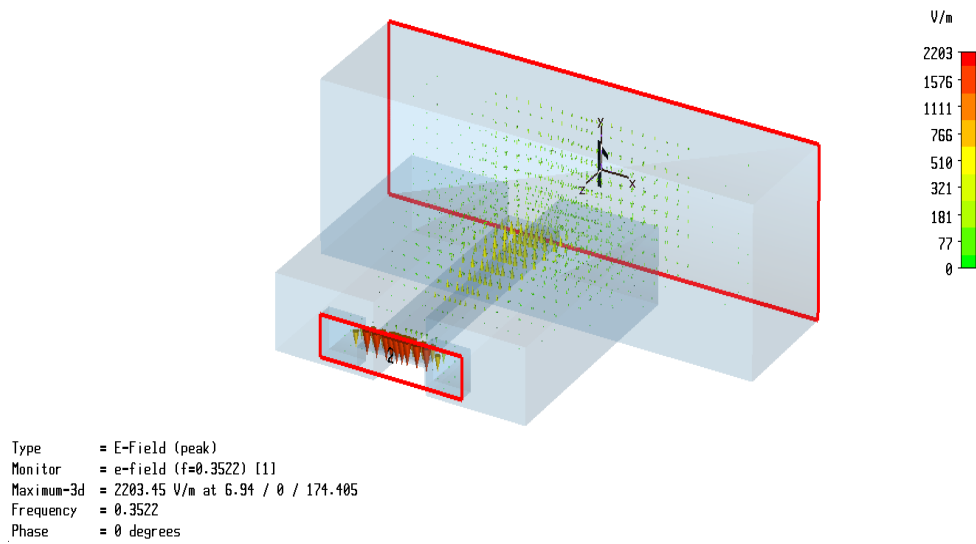
Fig. 4.4 Plot of (a) return loss at design frequency and (b) corresponding minimum return loss frequency.

It can be observed from Fig. 4.4(a) and (b) that return loss is better -25 dB and frequency shift is less than 0.1% of design frequency. This is because the end ridge height and width and WR 2300 height and width are not resulting in appreciable changes in their wave impedance and frequency of central matching section.

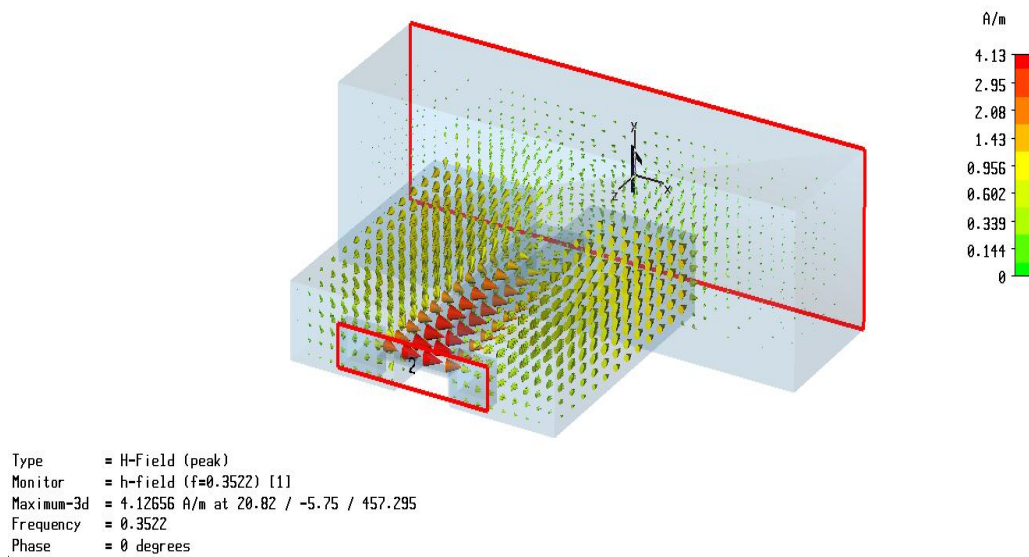
4.3 PROPOSED TUNING SCHEME FOR RIDGE WAVEGUIDE COUPLER

Before using the tuners on the coupler geometry, a detailed study of the electric and magnetic fields is carried out. It is found that fields are high at two ends of central ridge of 315 mm length. The benefit of using the tuners in the quarter wave region is spatial separation of electric and magnetic fields. The field plots obtained from CST-MWS simulations are shown in Fig. 4.5. The electric and magnetic field intensity plots are shown in Fig. 4.5. The field levels are peak quantities for 1 W peak power at input port.

The electric field in the matching section is high near the input port whereas magnetic field is high near the output port. These plots are for same RF phase (of zero degree) which means that relative electric and magnetic field concentrations are maintained at two ends throughout the RF cycle. As the central ridge section acts as a resonator, the resonance frequency depends upon its dimensions strongly. However, dimensional changes of output ridge section change the output impedance and results in the degradation of return loss. As return loss and resonance frequency shift may not be correlated, one tuner may not be able to relax the tolerances over a wide range. Hence, it is decided to use two cylindrical tuners. The two tuners are named as T_e and T_m . Tuner T_e refers to its placement in electric field dominated region whereas second tuner T_m refers to its placement in magnetic field dominated region. The spacing between the tuners is less than $\lambda_g/4$ as central matching ridge section is approximately quarter wavelength long.



(a)



(b)

Fig. 4.5 Arrow plots of (a) Electric and (b) magnetic field on simulated coupler.

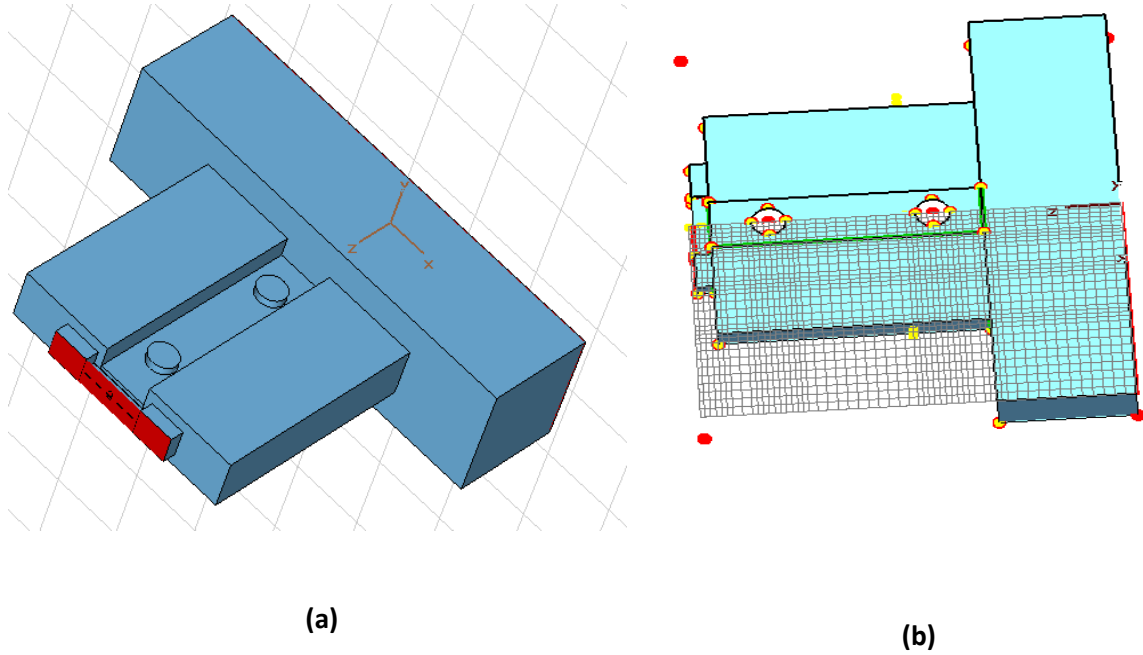


Fig. 4.6 Simulation model for (a) two cylindrical tuners on central ridge waveguide section and (b) mesh view on cut-plane of simulation model.

The simulation model of coupler along with Tuners is given in Fig. 4.6(a) whereas meshed geometry at a cut plane is shown in Fig. 4.6(b). As E and H symmetry planes are defined, only $1/4^{\text{th}}$ structure is meshed for simulations. As discussed in Section 4.2, 25 mesh points per wavelength are used. Both tuners are modeled as cylindrical rods of 20 mm radius. The T_e tuner is centered at 57.5 mm away (in z direction) from the start of the central section whereas T_m tuner is centered 67.5 mm before the end of central matching section. The distances from two ends are decided so that sufficient distance is available from the incoming waveguide wall and output ridge waveguide while mounting the tuners. It can be observed from Fig. 4.6(a), both are placed on the center line. As tuners are used to correct the effects of dimensional changes of coupler during manufacturing, it is important to study the effect of tuner movement on resonance frequency and return loss at 352.2 MHz. Any movement of tuner inside the coupler is termed as positive and out of the coupler is termed as negative. The coupler surface is taken as reference.

Maximum limit on insertion of these tuners is kept as 5 mm. The tuner port height will be more than 20 mm so that tuners could be withdrawn up to maximum of 10 mm. Tuners are effective only up to approx. 10 mm away from the coupler surface because of attenuating fields.

Fig. 4.7(a) shows the minimum return loss frequency variation with tuner depth. The plots of return loss at 352.2 MHz with tuner movement are shown in Fig. 4.7(b). The tuning range (in terms of frequency and return loss) is not symmetric with tuner movement from flush condition. The rate of frequency and return loss change is more for inward movement as compared to outward movement for both the tuners. This happens because tuner movement into the waveguide decreases the electric or magnetic volume of the resonator by a larger amount.

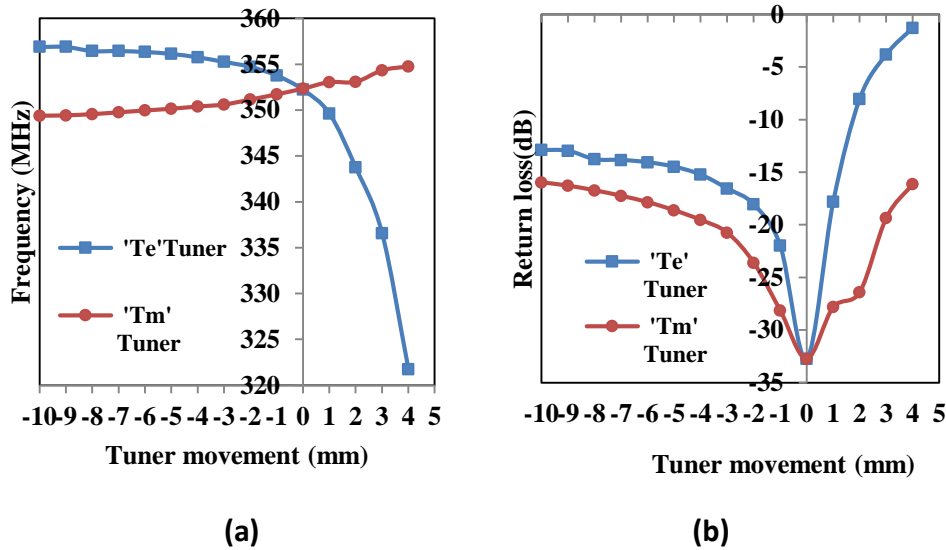


Fig. 4.7 Variation of (a) frequency of return loss minima and (b) S_{11} parameter at 352.2 MHz with tuner depth.

When the tuners are withdrawn from the flush condition, additional electric or magnetic volume is added to the resonator. However, due to attenuating fields in the cylindrical port, amount of electric or magnetic volume added keeps on decreasing with tuner withdrawal. By using more

tuners i.e. separate tuner for inward and outward movement placed at different locations along the z-axis), one may obtain a wider range and symmetric response. However, two tuners have been considered to demonstrate their effectiveness by keeping the analysis simple.

It is also observed from Fig. 4.7(a) that the slope of frequency change is negative for ‘Te’ Tuner and positive for ‘Tm’ tuner. This is because when the ‘Te’ tuner is lowered into the coupler, it increases the capacitive effect thereby decreasing the resonance frequency of central matching section. As the ‘Tm’ tuner is placed in the high magnetic field region, inductive effect is decreased when the tuner is inserted resulting in frequency increase.

4.4 TUNER OPTIMIZATION FOR COUPLER DIMENSIONAL ERRORS

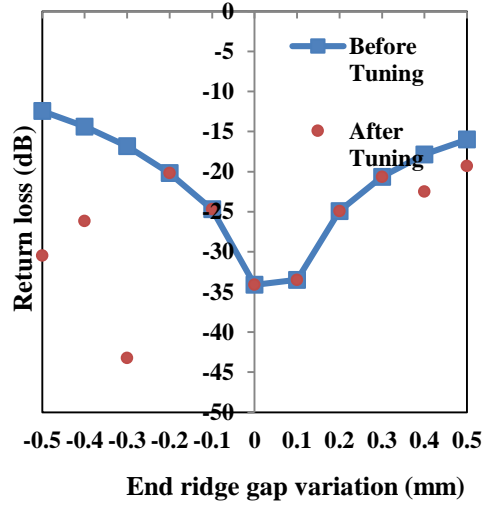
As observed in Section 4.2, S_{11} parameter is more sensitive to central ridge dimensions and end ridge gap. To demonstrate the tuner’s effectiveness, tuning studies are carried out for end ridge gap and central ridge gap dimensional changes. Tuners are applied to correct the effects of each shift. The return loss and frequency variation for end gap are in Figs. 4.8(a) and (b) respectively. Similarly, corresponding tuning results for central gap are shown in Figs. 4.8(c) and (d). The return loss can be tuned to better than -20 dB throughout the considered variation. Also, minimum return loss frequency when tuners are applied is within ± 0.2 MHz. The tuners are not applied if return loss is better than -20 dB. Hence, frequency shifts for those un-tuned acceptable cases is higher. The details of tuner depths for end gap and central ridge gap are given in Tables 4.2 and 4.3 respectively.

It is observed from Tables (4.2) and (4.3) that return loss can be tuned to better than -20 dB by optimizing the tuner depths. Tuners are applied to those dimensions only where return loss is worse than -20 dB.

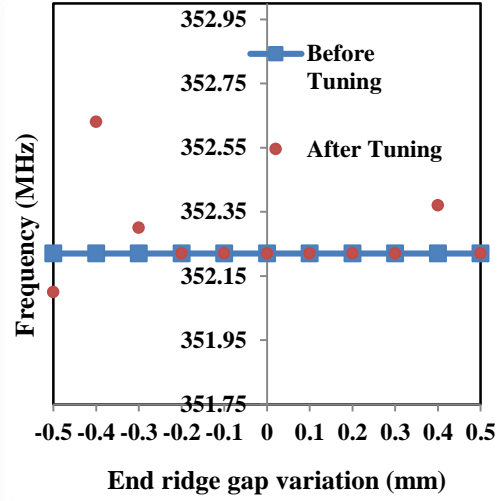
The tuners are found quite useful in restoring the RF matching of the coupler because of individual dimensional shifts. However, in real life scenario all coupler dimensions can experience dimensional shifts. To study the effects of these dimensional errors in detail, all the dimensions were changed as per the values given in Tables 4.4 and 4.5 respectively.

For each set of dimensional changes, tuner positions were optimized to obtain the best possible return loss and resonance frequency. Tuning results for dimensional changes as per Table 4.4 are shown in Figs. 4.9(a) and (b) respectively. Similarly, results for the dimensional changes as per Table 4.5 are shown in Figs. 4.9(c) and (d). It can be concluded that effects of dimensional changes of up to 1.0 mm could be corrected with the tuners. The details of tuner positions are given in Table 4.6.

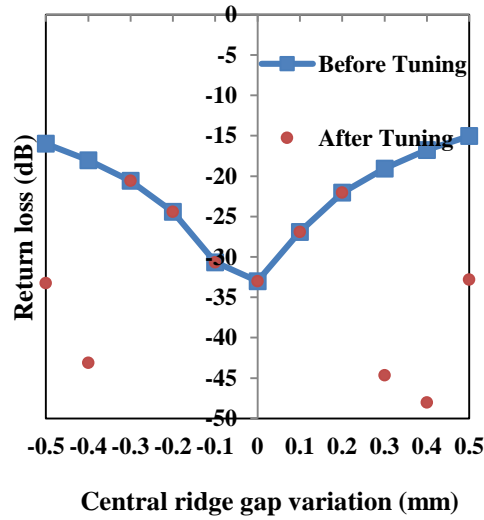
The frequency and return loss accuracies calculated with CST-MWS is related to the S parameter accuracies. Frequency domain solver of CST-MWS is used in auto-meshing mode so that meshing is refined iteratively to obtain an S parameter accuracy of better than .01. Similarly, the accuracy level is set to 1×10^{-9} wherever Eigen mode solver of CST-MWS is used in this work.



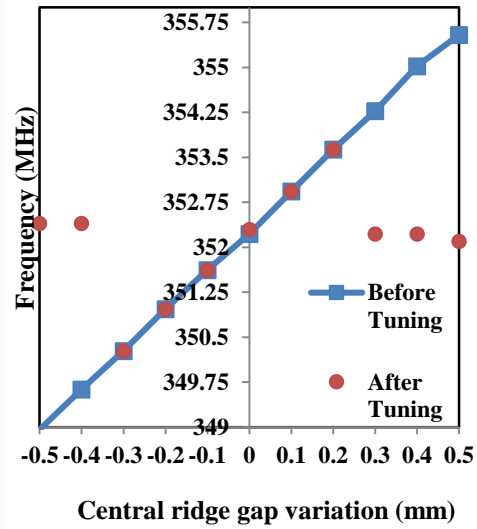
(a)



(b)



(c)



(d)

Fig. 4.8 Tuning results for (a) Return loss and (b) frequency values for before and after tuning for end gap changes; (c) return loss and (d) frequency values for before and after tuning for central gap changes.

Table 4.2 Tuning results for return loss and frequency with end gap variation.

End gap (mm)	Return Loss before Tuning (dB)	Return Loss after tuning (dB)	Frequency before tuning (MHz)	Frequency after tuning (MHz)	Tuner position in mm (Te,Tm)
1.05	-12.43	-30.48	352.22	352.10	0.5,4.6
1.15	-14.37	-26.14	352.22	352.3	0.7,4.0
1.25	-16.83	-43.24	352.22	352.22	0.7,3.4
1.35	-20.17	-20.17	352.22	352.22	0.0,0.0
1.45	-24.68	-24.68	352.22	352.22	0.0,0.0
1.55	-34.10	-34.1	352.22	352.22	0.0,0.0
1.65	-33.48	-33.48	352.22	352.22	0.0,0.0
1.75	-24.90	-24.9	352.22	352.22	0.0,0.0
1.85	-20.63	-20.63	352.22	352.22	0.0,0.0
1.95	-17.85	-22.5	352.22	352.37	-3.5,-10
2.05	-15.99	-19.3	352.22	352.22	-3.5,-10

Table 4.3 Tuning results for return loss and frequency with central ridge gap variation.

Central gap (mm)	Return Loss before Tuning (dB)	Return Loss after tuning (dB)	Frequency before tuning (MHz)	Frequency after tuning (MHz)	Tuner position in mm (Te,Tm)
11.0	-15.98	-33.25	348.96	352.40	-3.5,0.0
11.1	-18.02	-43.13	349.63	352.40	-3.7,-1.0
11.2	-20.58	-20.58	350.27	350.27	0.0,0.0
11.3	-24.42	-24.42	350.97	350.97	0.0,0.0
11.4	-30.66	-30.66	351.62	351.62	0.0,0.0
11.5	-33.01	-33.01	352.22	352.30	0.0,0.0
11.6	-26.9	-26.90	352.93	352.93	0.0,0.0
11.7	-22.05	-22.05	353.63	353.63	0.0,0.0
11.8	-19.05	-44.66	354.27	352.22	1.0, 2.0
11.9	-16.77	-48.02	355.02	352.22	1.1,2.0
12.0	-15.04	-32.8	355.54	352.10	1.5,3.0

Table 4.4 Details of dimensional variations on all coupler dimensions (Set 1).

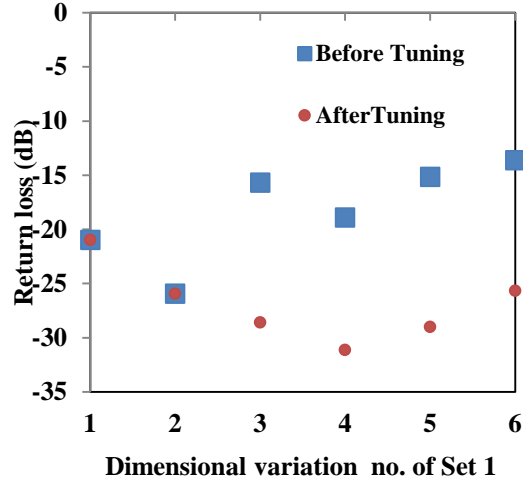
Parameter	Variation 1 (mm)	Variation 2 (mm)	Variation 3 (mm)	Variation 4 (mm)	Variation 5 (mm)	Variation 6 (mm)
eg	-0.1	+0.1	-0.2	+0.2	-0.2	+0.2
cg	+0.1	-0.1	+0.2	-0.2	+0.2	-0.2
cl	-0.1	+0.1	-0.2	+0.2	-1.0	+1.0
ew	+0.1	-0.1	+0.2	-0.2	+1.0	-1.0
cw	-0.1	+0.1	-0.2	+0.2	-1.0	+1.0
c-ow	+0.1	-0.1	+0.2	-0.2	+1.0	-1.0
ch	-0.1	+0.1	-0.2	+0.2	-1.0	+1.0
e-ow	+0.1	-0.1	+0.2	-0.2	+1.0	-1.0
eh	-0.1	+0.1	-0.2	+0.2	-1.0	+1.0
w	+0.1	-0.1	+0.2	-0.2	+1.0	-1.0
h	-0.1	+0.1	-0.2	+0.2	-1.0	+1.0

Table 4.5 Details of dimensional variation on all coupler dimensions (Set 2).

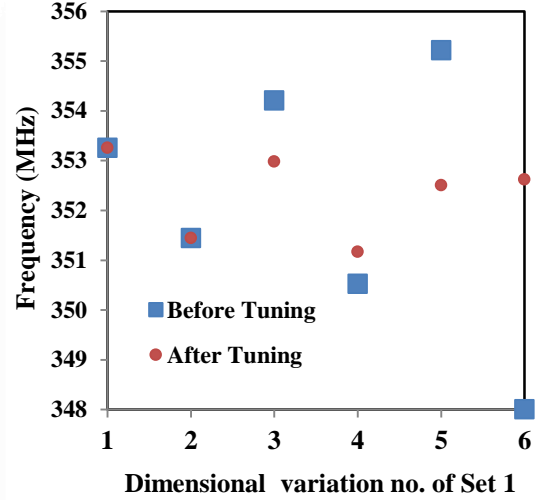
Parameter	Variation 1 (mm)	Variation 2 (mm)	Variation 3 (mm)	Variation 4 (mm)	Variation 5 (mm)	Variation 6 (mm)
eg	-0.1	+0.1	-0.2	+0.2	-0.2	+0.2
cg	-0.1	+0.1	-0.2	+0.2	-0.2	+0.2
cl	-0.1	+0.1	-0.2	+0.2	-1.0	+1.0
ew	-0.1	+0.1	-0.2	+0.2	-1.0	+1.0
cw	-0.1	+0.1	-0.2	+0.2	-1.0	+1.0
c-ow	-0.1	+0.1	-0.2	+0.2	-1.0	+1.0
ch	-0.1	+0.1	-0.2	+0.2	-1.0	+1.0
e-ow	-0.1	+0.1	-0.2	+0.2	-1.0	+1.0
eh	-0.1	+0.1	-0.2	+0.2	-1.0	+1.0
w	-0.1	+0.1	-0.2	+0.2	-1.0	+1.0
h	-0.1	+0.1	-0.2	+0.2	-1.0	+1.0

Table 4.6 Tuning details for dimensional variations on all coupler dimensions

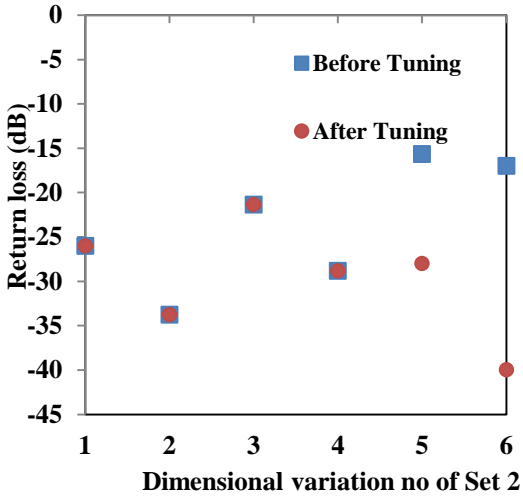
Dimensional variation	Return Loss before tuning (dB)	Return Loss after tuning (dB)	Frequency before tuning (MHz)	Frequency after tuning (MHz)	Te-Tuner Position (mm)	Tm-Tuner Position (mm)
Set 1						
Variation 1	-20.98	-20.98	353.26	353.26	0	0
Variation 2	-25.94	-25.94	351.45	351.45	0	0
Variation 3	-15.67	-28.6	354.21	352.98	1.2	3.8
Variation 4	-18.90	-31.13	350.53	351.17	-10	-10
Variation 5	-15.16	-29.00	355.22	352.51	1	1.75
Variation 6	-13.61	-25.67	348.01	352.62	-10	0
Set 2						
Variation 1	-26.00	-26.00	352.20	352.20	0	0
Variation 2	-33.76	-33.76	352.29	352.29	0	0
Variation 3	-21.34	-21.34	351.7	351.7	0	0
Variation 4	-28.83	-28.83	352.29	352.29	0	0
Variation 5	-15.66	-28.00	354.78	352.1	1.3	3.5
Variation 6	-16.99	-39.96	349.3	352.22	-10	-3



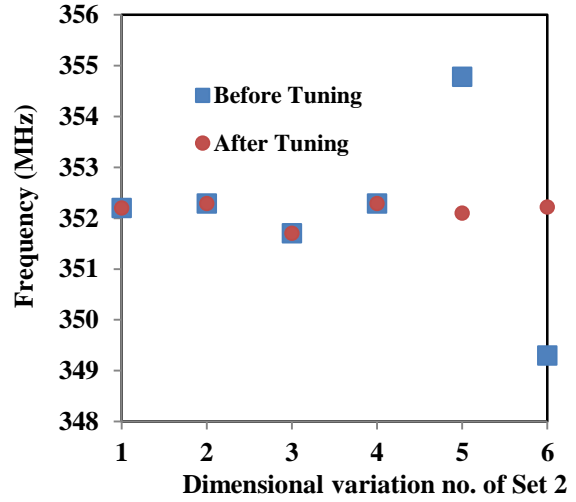
(a)



(b)



(c)



(d)

Fig. 4.9 Tuning results for (a) return loss and (b) frequency values before and after tuning for Set1 of dimensional changes (c) return loss and (d) frequency values before and after tuning for Set 2 of dimensional changes .

The proposed tuning scheme is able to relax the individual gap dimension changes up to ± 0.5 mm. Simultaneous changes of up to ± 0.2 mm on gaps and ± 1.0 mm on other dimensions could be allowed when tuners are used.

4.5 TUNER STUDIES ON IRIS COUPLER WITH CAVITY COUPLING

Though the effectiveness of tuners is demonstrated for a given coupler, it only helps in qualifying the couplers at designed RF parameters during back to back tests. This can be achieved by connecting a high power source at input and a matched load at the output. However, the coupler has to be finally coupled to an accelerator cavity through an iris. Hence, it is important to study the behavior of coupled cavity system for various dimensional changes. In this study, pillbox cylindrical cavity of 326.2 mm radius is modeled so that it resonates at 352.2 MHz without any iris. It is coupled to the waveguide coupler through an iris.

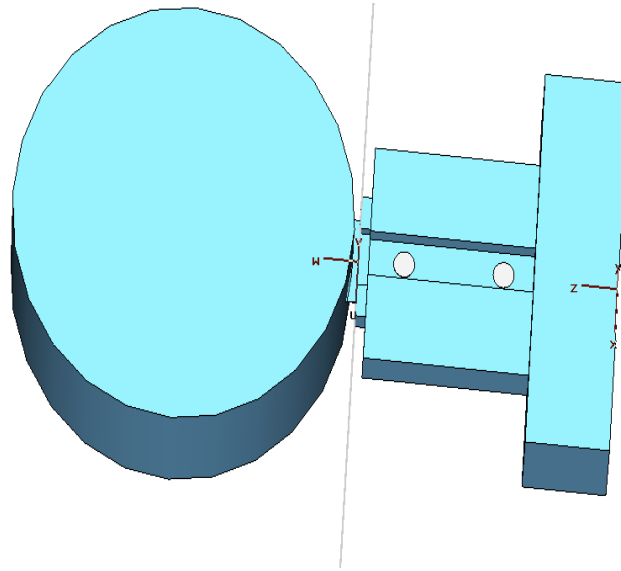


Fig. 4.10 RF Coupler connected to the pill box cavity through an iris.

The model is shown in Fig. 4.10. The iris dimensions are chosen in such a way that external quality factor (Q_{ext}) of 18100 is obtained at input port. The coupling coefficient is the ratio of intrinsic quality factor (Q_0) and Q_{ext} and should be 1 for critical coupling. The Q_{ext} is calculated from Modal solver by applying port boundary condition at input waveguide port. For each tuner position, Q_{ext} value is obtained from Modal solver results.

For explaining the design choices of tuners and coupler dimensions for a coupler cavity system, an equivalent circuit based can be useful. An equivalent circuit given in Fig. 4.11 may be used to describe the 3D model of Fig. 4.11.

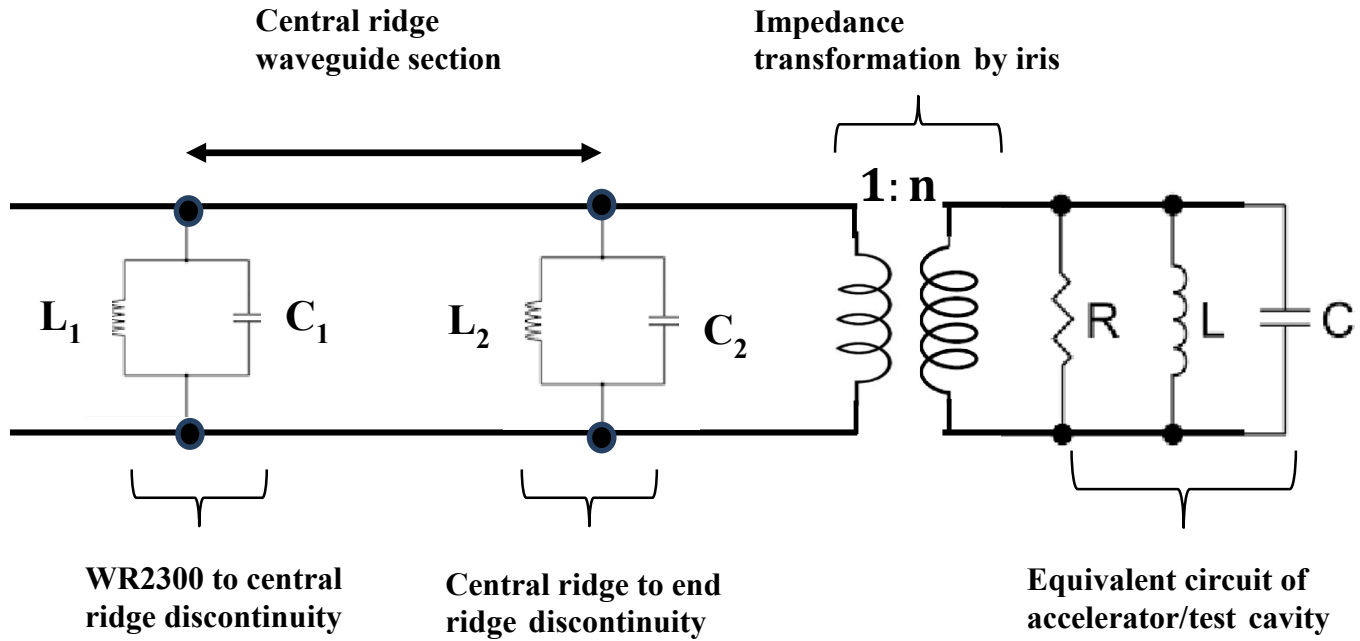


Fig. 4.11 Equivalent circuit of ridge waveguide coupler connected to a cavity.

In the proposed equivalent circuit, accelerator cavity or test cavity resonator is represented as a parallel RLC circuit. The dumbbell shaped iris (or any other iris shapes) couples the cavity's magnetic field to the incoming waveguide. The effect of magnetic coupling is represented as a transformer of ratio $1:n$. The impedance transformation is achieved by properly sizing the iris dimensions. The incoming WR2300 half height waveguide to central ridge transition discontinuity is represented as combination of inductive (L_1) and capacitive discontinuity (C_1). The central ridge to end ridge discontinuity is also represented as a combination of inductive (L_2) and capacitive effect (C_2). The central ridge waveguide section is approximately quarter

wavelength long and it transforms the load impedance so that reactive part of the rectangular to ridge waveguide discontinuity is cancelled. The tuners are placed near the locations of these discontinuities to utilize the stored energies for coupling tuning. The detailed analysis of this circuit will be useful in understanding the effect of various coupler dimensions.

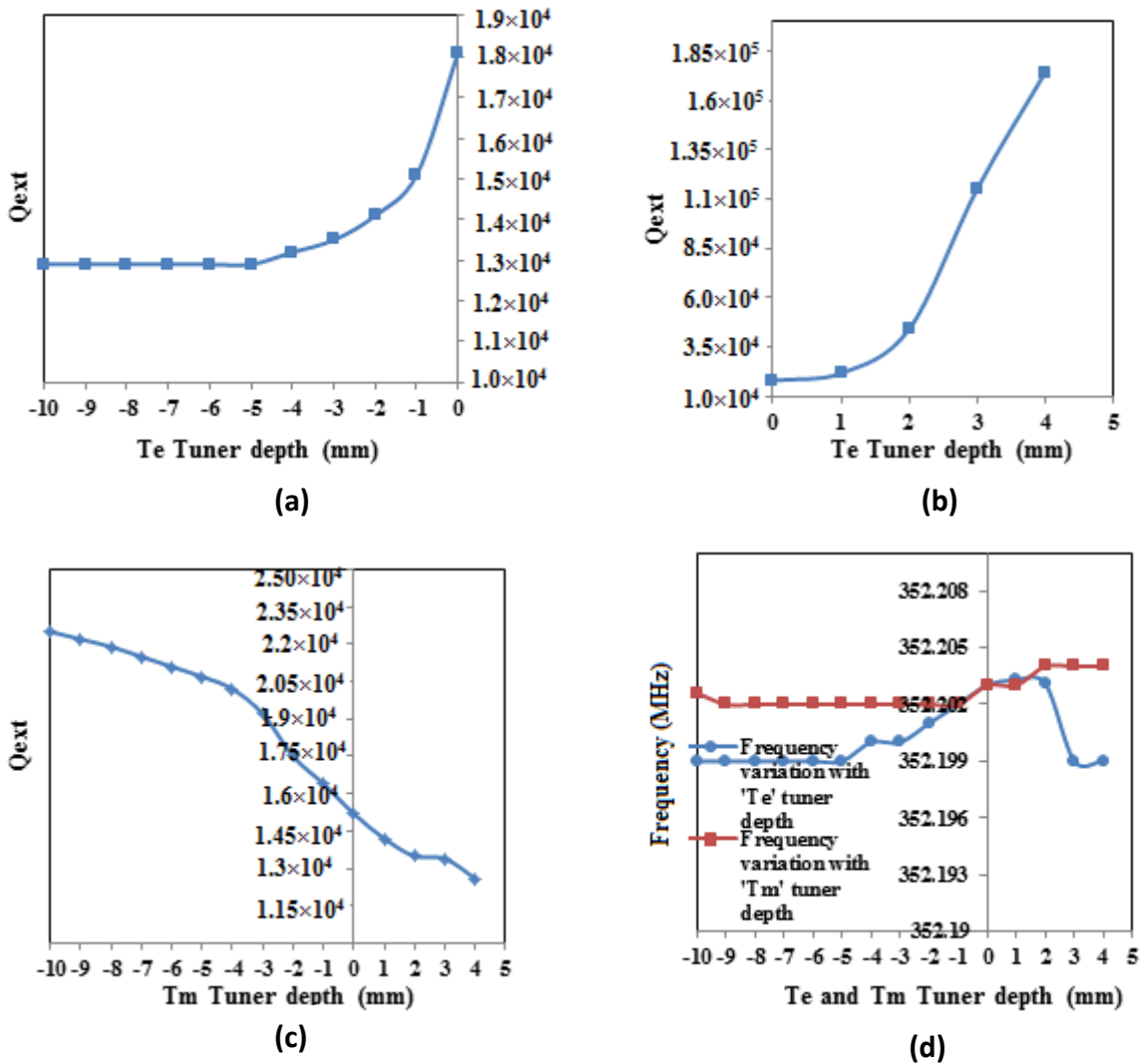


Fig. 4.12 Tuning results for (a) Q_{ext} with T_e Tuner movement up to the coupler surface; (b) Q_{ext} variation with T_e Tuner movement into the central gap from coupler surface; (c) Q_{ext} variation with T_m Tuner movement and (d) resonant frequency variation of coupled system with T_e and T_m Tuner movement.

The Q_{ext} variation with T_e tuner depth is plotted in Figs. 4.12(a) and (b). The Q_{ext} variation for T_m tuner is shown in Fig. 4.12(c). It is observed that Q_{ext} varies substantially with T_e tuner. This indicates that the tuners will be useful in tuning the Q_{ext} . The resonance frequency variation of coupled system with T_e and T_m tuner movement is plotted in Fig. 4.12(d). The tuner movement affects the resonance frequency of coupled system only marginally, the frequency shift is less than 6 kHz for entire tuning range. This is in contrast to individual coupler case as shown in Fig. 4.7 earlier. The similar trend is observed during further studies on coupled system for dimensional shifts.

4.5.1 Tuning studies for individual coupler dimension

The coupled system is subjected to end gap changes and Q_{ext} value is obtained from Modal solver. For the extreme shifts of ± 0.5 mm in end gap, it is found that Q_{ext} value changes are within tolerable limit as resulting return loss is better than -25 dB. The return loss is calculated for Q_o of 18100. This will give critical coupling for unperturbed coupler geometry with Q_{ext} of 18100. Return loss is taken as -33 dB for unperturbed case. For central ridge gap, return loss could be tuned back by applying the tuners with same lengths as in Table 4.3. The results of these studies for end gap and central gap are listed in Table 4.7 and 4.8 respectively. The Q_{ext} and return loss values listed in Table 4.7 show that no tuning is required for changes in end gap for coupler-cavity system. This is different from single coupler case as given in Table 4.2. as tuning is required.

However, tuning is required for one variation of central gap as given in Table 4.8. This demonstrates the tuners effectiveness for individual dimension changes in coupled case as well.

Table 4.7 Tuning details for end gap dimensional shifts.

End gap (mm)	Q_{ext} before tuning	Q_{ext} after Tuning	Return Loss before tuning (dB)	Return Loss after tuning (dB)	Te- Tuner Position (mm)	Tm- Tuner Position (mm)
1.05	16300	16300	-26	-26	0	0
1.55	18100	18100	-33	-33	0	0
2.05	17300	17300	-26	-26	0	0

Table 4.8 Tuning details for central gap dimensional shifts.

Central gap (mm)	Q_{ext} before tuning	Q_{ext} after Tuning	Return Loss before tuning (dB)	Return Loss after tuning (dB)	Te- Tuner Position (mm)	Tm- Tuner Position (mm)
11.0	24100	17900	-17	-45	-3.5	0
11.5	18100	18100	-33	-33	0	0
12.0	15200	19200	-21	-31	1.5	3.0

4.5.2 Studies for dimensional errors on all coupler dimensions

The dimensional changes as per Table 4.4 and 4.5 are applied to the coupled system also. The results are given in Table 4.9. The return loss deteriorate below -20 dB in only two of total twelve variations. This is in contrast to individual coupler case where six variations were needed for tuning as listed in Table 4.6. However, tuners are able to correct the resulting Q_{ext} shifts to acceptable levels. The same depths of tuners are applied here as in case of standalone coupler. The same depths of tuners are able to improve the resulting changes in Q_{ext} . This fact establishes the use of tuners to take care of coupler dimensional errors for coupled system as well. In other

way, assuming coupler dimensions are ideal, tuners can be used to simply change the Q_{ext} to desired value.

Table 4.9 Q_{ext} Tuning results for coupled system.

Dimensional variation	Q_{ext} before tuning	Q_{ext} after tuning	Frequency before tuning (MHz)	Frequency after tuning (MHz)	T_e -Tuner Position (mm)	T_m -Tuner Position (mm)	Return Loss in dB before tuning (after tuning)
Set 1							
Variation 1	15800	15800	352.202	352.202	0	0	-23.4 (-23.4)
Variation 2	17900	17900	352.203	352.203	0	0	-45.0 (-45.0)
Variation 3	15000	17100	352.202	352.206	1.2	3.8	-20.6 (-30.9)
Variation 4	21200	20000	352.198	352.197	-10	-10	-22.1 (-26.0)
Variation 5	14500	15100	352.199	352.202	1	1.75	-19.1 (-20.9)
Variation 6	23300	15700	352.200	352.200	-10	0	-18.0 (-23.0)
Set 2							
Variation 1	17200	17200	352.202	352.202	0	0	-31.9 (-31.9)
Variation 2	16300	16300	352.202	352.202	0	0	-25.6 (-25.6)
Variation 3	17700	17700	352.203	352.203	0	0	-39.0 (-39.0)
Variation 4	17100	17100	352.197	352.197	0	0	-30.9 (-30.9)
Variation 5	15200	18500	352.205	352.205	1.3	3.5	21.2 (-39.2)
Variation 6	20600	16500	352.190	352.190	-10	3	23.8 (-26.7)

As shown earlier, the change is very fast for T_e tuner. In such application scenario, the T_e tuner radius can be decreased from 20 mm to obtain lower Q_{ext} change with Tuner movement. As coupling coefficient (which is the ratio of Q_o and Q_{ext}) is generally tuned by machining the iris, the proposed tuner based approach is also able to achieve it. The tuner based approach is more

versatile as it can be used during coupler testing without intermediate cavity as well. The coupled cavity system is more tolerant towards coupler dimensional errors. The reason lies in the fact that the resonant cavity is coupled through an iris where fields are attenuating. The overall resonance frequency is dominated by the cavity resulting in less frequency shift and hence less dependence on coupler dimensions. Once the iris dimensions are fixed, changes in resonance frequency of the cavity because of coupler dimensions are negligible.

4.6 COMPARISON WITH TAPERED RIDGE WAVEGUIDE COUPLER

4.6.1 Introduction

Different ridge waveguide transitions like constant impedance taper [69], tapered ridge with a constant width [16,53] and a straight ridge coupler [97] have been used or are under consideration for the high power waveguide-cavity couplers in different accelerators worldwide. Though, these designs have been considered in different accelerator projects, there is no report of a comparative study on their dimensional tolerances. In order to study this dependence, a comparative electromagnetic study is carried out on the straight ridge and the linearly tapered ridge transitions using CST-MWS.

4.6.2 Comparative analysis of waveguide transitions

A detailed numerical analysis is carried out for the linear taper using CST-MWS. The results are compared to the straight ridge taper discussed in previous section. For the purpose of this discussion, input waveguide of WR2300 size and half height is considered. The design frequency is taken as 352.2 MHz. The incoming waveguide is matched to an output ridge waveguide of smaller cross-section. The matching section consists of a tapered ridge waveguide. Fig. 4.13(a) shows the top and cross-sectional views of tapered transition. Simulation model of the tapered

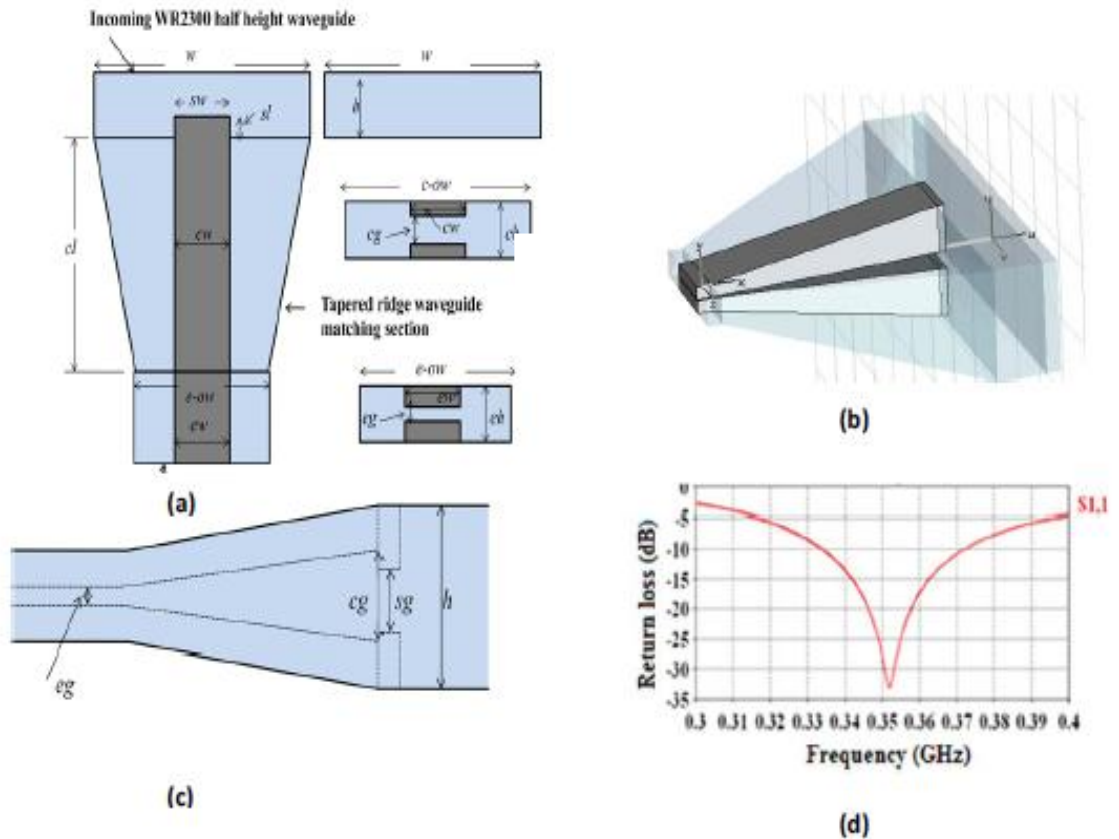


Fig. 4.13 Tapered ridge waveguide coupler's (a) top view and cross-sectional view; (b) CST MWS simulation model of coupler; (c) side view of coupler and (d) S_{11} parameters plot obtained from simulations for optimized geometry.

All the important dimensions of tapered ridge transition are summarized in Table 4.10. The equivalent dimensions for the straight ridge transition are also given, which are discussed in Section 4.5.

Table 4.10 Dimensions of the optimized tapered and straight ridge transition.

Parameter	Description	Value for tapered coupler (mm)	Value for straight ridge coupler (mm) Ref*[4]
w	WR2300 width	584.2	584.2
h	WR2300 height	146.05	146.05
wl	Input Port length	160	160
$c-ow$	Central section-overall width	584.2 to 189	334
cw	Central ridge width	89	69.4
cl	Central ridge length	321.7	315
cg	Central ridge gap	22.2 to 1.55	11.5
ch	Central ridge height	146.05 to 35	64
ew	End ridge width	89	89
$e-ow$	End section- overall width	189	189
eg	End ridge gap	1.55	1.55
eh	End ridge height	35	35
el	Output Port length	20	20
sw	Starting ridge width	89	Not present
sl	Starting ridge length	10	Not present
sg	Starting ridge gap	15.65	Not present

Ref*[4] in various Figures of section 4.6 refers to the author's following published work based on Section 4.5 :
 Rajesh Kumar, P.Singh, Divya Unnikrishanan, Girish Kumar, "A *tunable waveguide to cavity coupler for high power accelerator cavities*", Nuclear Instruments and Methods in Physics Research A, Vol. 664, 203-213 (2012)

For the sake of completeness, a 3D CST model of straight ridge taper is shown in Fig. 4.14(a). Simulation model of the tapered coupler with meshing is shown in Fig. 4.14(b). In the parametric studies for tapered coupler, frequency domain solver of CST MWS is used with tetrahedral

meshing. Twenty points per wavelength are assigned for meshing which results in approximately 30,000 tetrahedrons. The solver accuracy is set at $1E-5$.

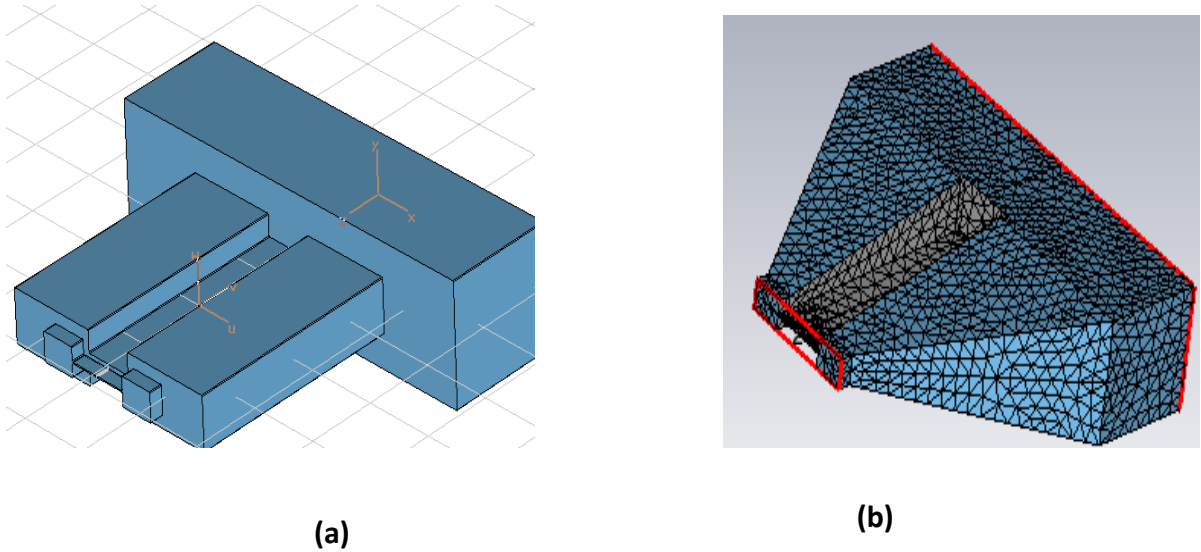


Fig. 4.14 CST MWS simulation model of (a) straight coupler and (b) simulation model of tapered coupler with meshing.

4.6.2.1 Studies for the return loss and resonant frequency variation

The end ridge gap is varied in steps of 0.1 mm for linearly tapered ridge waveguide transition. The plot of return loss for design frequency of 352.2 MHz is shown in Fig. 4.15(a). For the comparison purpose, the variation for straight ridge waveguide discussed in Section 4.5 (mentioned as Ref.[4] in the plots) is also given on the same plot. We can see that there is some non-symmetry in the return loss plots which is because the optimum value of gap may be slightly different. Similarly, the minimum return loss frequency plots are given in Fig. 4.15(b). The dependence of return loss variation with end gap is almost same in the straight ridge and linearly tapered ridge waveguide transition.

It is noticed from Fig. 4.15(b) that there is more frequency variation for tapered coupler. This is due to the fact that variation of end gap not only changes the end ridge impedance, it changes the taper angle as well. This is not the case in straight ridge coupler as the central ridge gap remains same during simulations. The variations in end gap only change the end ridge impedance in straight ridge coupler. As the central ridge dimensions remain same in straight ridge coupler, frequency variation is flat. However, return loss varies in straight ridge coupler because of the change in end ridge impedance

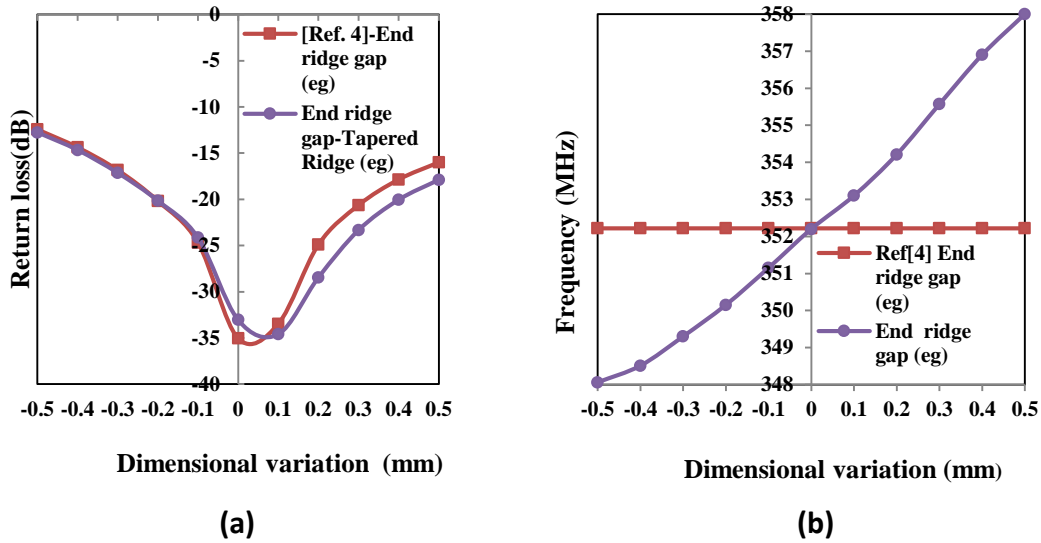
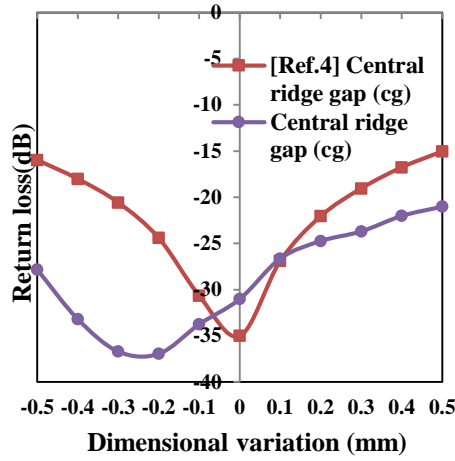
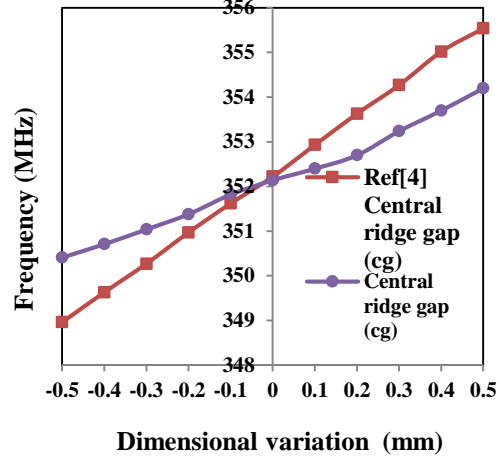


Fig. 4.15 Plots of (a) return loss at design frequency (of 352.2 MHz) with end gap changes and (b) frequency variation corresponding minimum return loss.

The variation of return loss at 352.2 MHz with central ridge gap is shown in Fig. 4.16(a). The corresponding plots for minimum return loss frequency are shown in Fig. 4.16 (b). The central ridge gap parameter 'cg' is varied during this simulation whereas 'eg' and 'sg' are kept constant.



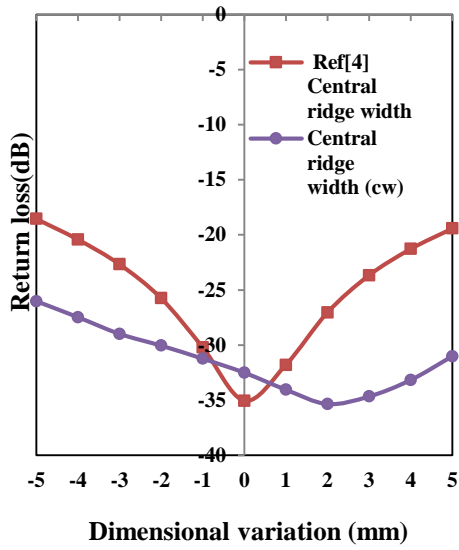
(a)



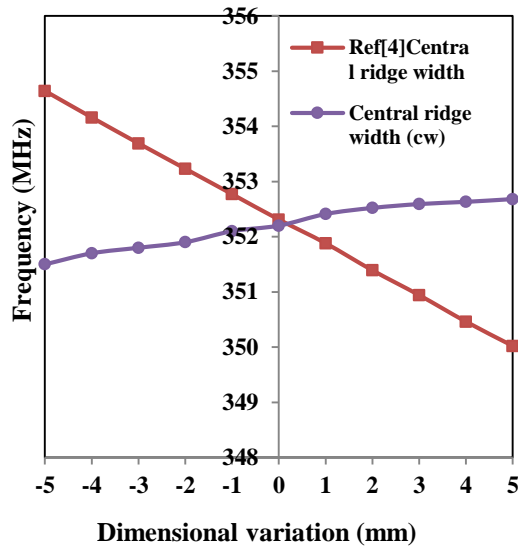
(b)

Fig. 4.16 Plots of (a) return loss at design frequency (of 352.2 MHz) with central gap changes and (b) frequency variation corresponding minimum return loss.

Similarly, the variation of return loss at 352.2 MHz with the central ridge width and the length is shown in Figs. 4.17(a) and 4.18(a) respectively. The dimensions are changed by ± 1.0 mm. The corresponding plots for the frequency at minimum return loss are shown in Figs. 4.17(b) and 4.18(b). The return loss deterioration is less in a tapered ridge waveguide as compared to the straight ridge. Except for the end ridge gap and central ridge gap (where parametric step is ± 0.1 mm), all other parametric variations in steps of ± 1.0 mm show a return loss of better than -20 dB for linearly tapered structure.

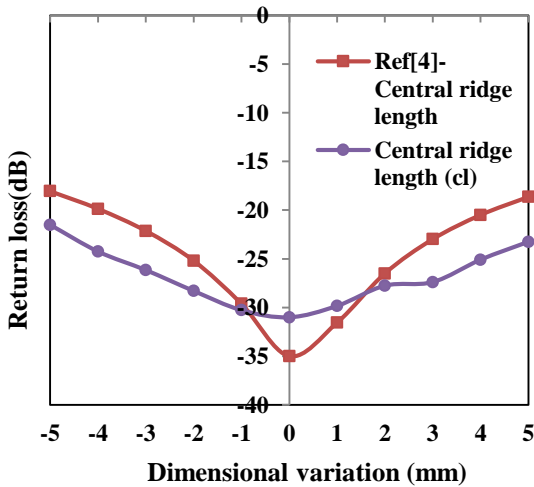


(a)

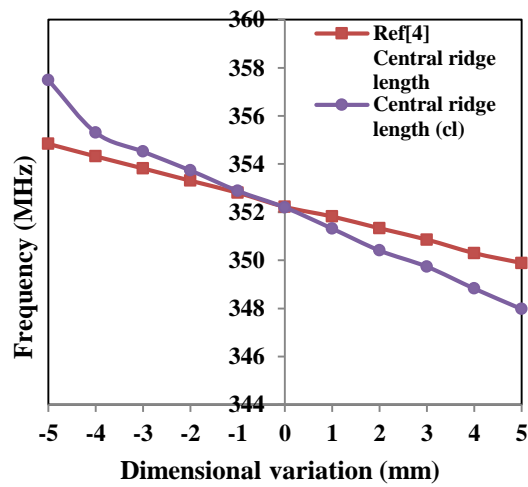


(b)

Fig. 4.17 Plots of (a) return loss at design frequency (of 352.2 MHz) with central ridge width changes and (b) frequency variation corresponding to minimum return loss.



(a)



(b)

Fig. 4.18 Plots of (a) return loss at design frequency (of 352.2 MHz) with central ridge length changes and (b) frequency variation corresponding minimum return loss.

Finally, the variation of return loss at 352.2 MHz with WR2300 width and height are simulated by varying the dimensions in steps of ± 1 mm. The plots are shown in Figs. 4.19(a) and 4.20(a) respectively. The corresponding plots for the frequency value at minimum return loss are shown in Figs. 4.19(b) and 4.20(b). It can be seen that the return loss and frequency deterioration is slightly more in tapered ridge waveguide as compared to straight ridge. However, the return loss still remains better than -25 dB in a tapered ridge.

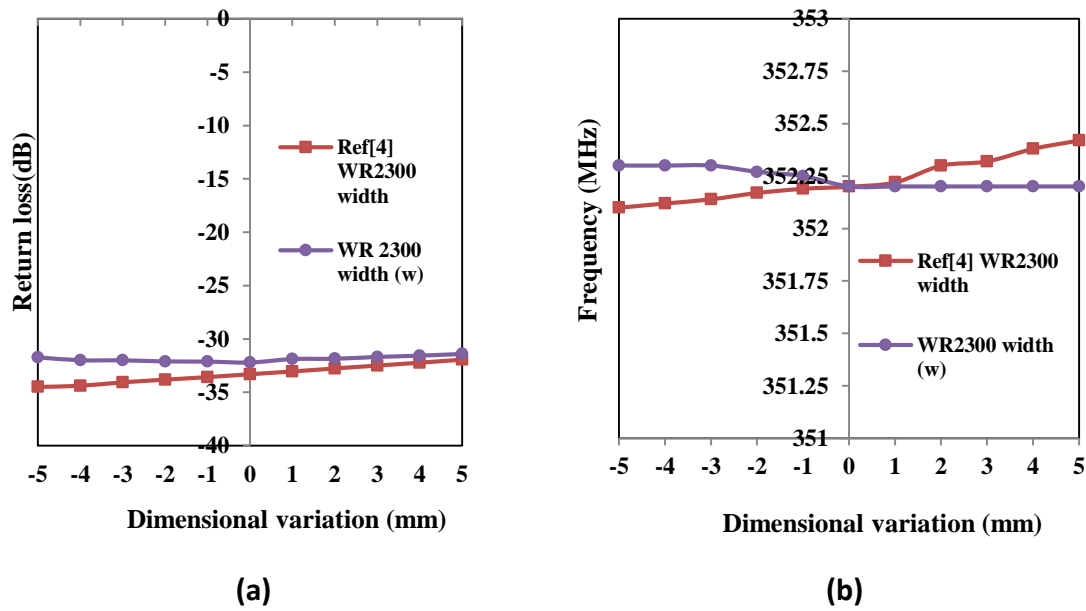


Fig. 4.19 Plots of (a) return loss at design frequency (of 352.2 MHz) with WR 2300 width changes and (b) frequency variation corresponding minimum return loss.

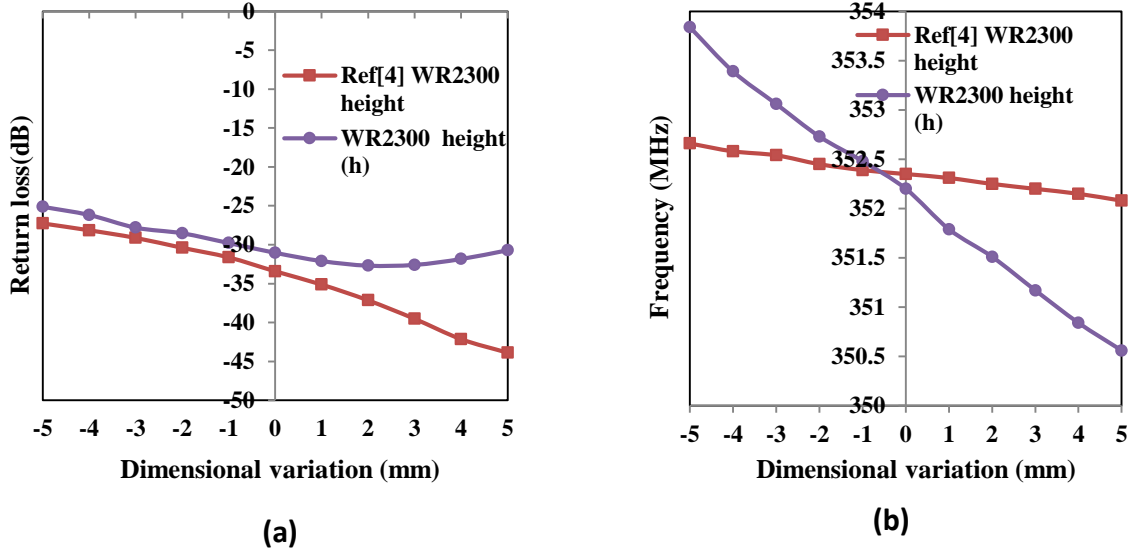


Fig. 4.20 Plots of (a) return loss at design frequency (of 352.2 MHz) with WR 2300 height changes and (b) frequency variation corresponding minimum return loss.

4.6.2.2 Dimensional variations on all coupler dimensions

The tapered ridge coupler is less sensitive to the most of the individual dimensional changes. More changes were applied to the parameters as given in Table 4.11. All the parameters were changed by ± 1 mm except the end ridge and central ridge gape. The ridge gaps were changed by $\pm .2$ mm only. These changes correspond to variation no. 6 from Set 1 and Set 2 as given in Section 4.4.1. We can see from Table 4.11 that the variation of return loss and frequency is much less in the tapered coupler than a straight ridge coupler. It should be noted here that only maximum shift is considered here because for smaller dimensional shifts, the return loss of tapered ridge does not deteriorate beyond -20 dB.

Table 4.11 Comparison for dimensional changes on all coupler dimensions.

Variation number	Tapered coupler Return Loss (dB)	Straight ridge coupler Return (dB)	Tapered ridge frequency (MHz)	Straight ridge frequency (MHz)
Variation 6 (Set1)	-18.68	-13.61	353.14	348.01
Variation 6 (Set2)	-20.9	-16.99	353.3	349.3

4.6.2.3 Transmission phase and insertion loss

Amplitude and phase balance are also important parameters in multiple coupler based cavity systems as the cavity acts as a power combiner in such applications [98]. Hence, a comparative study was carried out to study the effect of dimensional changes on the transmission phase and insertion loss. Insertion loss is also important for thermal management in high CW power applications.

As the return loss is quite sensitive to the end gap and central ridge gap, the corresponding study for transmission phase was also carried out. The plots for phase shift with end gap and central ridge gap are given in Figs. 4.21(a) and (b) respectively. Similarly, plots for the phase shift with central ridge length variation are given in Fig. 4.22.

It can be observed from Fig. 4.21(a) that the transmission phase shift is more for the tapered ridge as compared to the straight ridge in case of end ridge variation. However, as can be seen from Figs. 4.21(b) and 4.22, the phase shift is lesser in a tapered ridge coupler for central ridge gap and central ridge length variation.

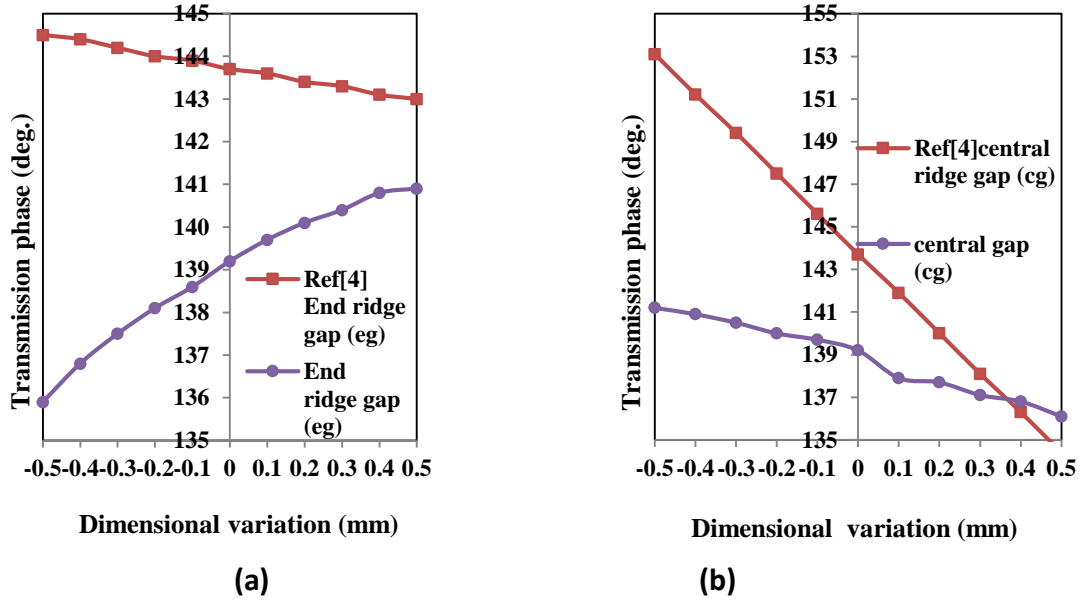


Fig. 4.21 Transmission phase plots (a) at design frequency with end gap changes and (b) corresponding variation of transmission phase with central gap changes.

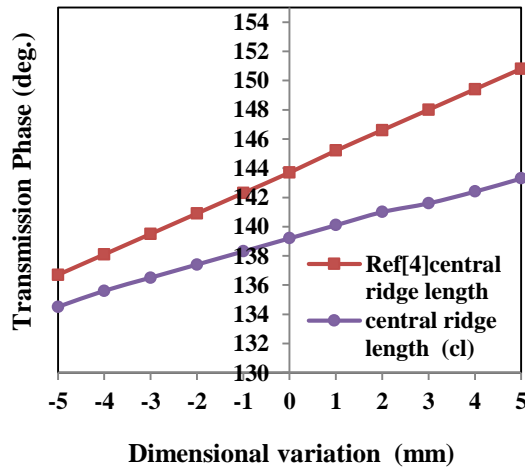


Fig. 4.22 Transmission phase at design frequency for central ridge length changes.

The insertion loss for the tapered ridge coupler is found using thermal loss calculations available in post processing module of CST-MWS. It is found to be 0.135% of input power for tapered ridge coupler. The corresponding value for the straight ridge coupler is 0.155%. For 250 kW

CW power, RF loss on tapered coupler will be around 340 W whereas for straight ridge coupler, loss will be around 400 W.

4.6.3 Comparison of return loss bandwidth

The return loss plots for the straight ridge and the tapered ridge coupler are given in Fig. 4.23. The bandwidth for a tapered ridge coupler is more than the straight ridge coupler. The -20 dB return loss bandwidth of tapered coupler is 11.26 MHz (i.e 3.2 % at 352.2 MHz) whereas it is 4.03 MHz (1.14%) for the straight ridge coupler. The transmission phase shift (i.e S_{21} phase) in the tapered ridge coupler is only 1.34 degrees/MHz whereas it is 3.05 degrees/MHz for the straight ridge coupler. This happens because of broader bandwidth of tapered ridge coupler as compared to the straight ridge coupler.

4.6.4 Electric and magnetic field distributions

The electric and magnetic field distributions were obtained from the time domain solver of CST-MWS at 352.2 MHz. The plot of electric field and magnetic field distributions for 1 W input power are shown in Fig. 4.24. The maximum peak electric field on the coupler is approx. 1800 V/m. Maximum field on the coupler at 250 kW CW power will be around 1.27 MV/m. The electric field is almost constant along the central region of tapered coupler whereas the magnetic field is varying along the coupler length. This is clearly evident from line plots of Fig. 4.25. The electric field is much lower in the central region of the tapered coupler as compared to the straight ridge coupler. Also, the magnetic field intensity is lesser in most of the central region of the tapered coupler as shown in Fig. 4.24(b). In fact, this results in lower RF losses in tapered coupler than the straight ridge coupler.

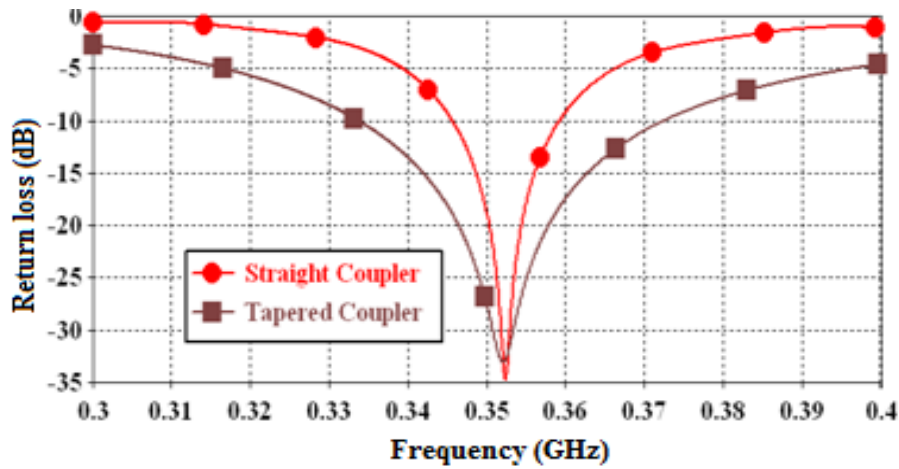
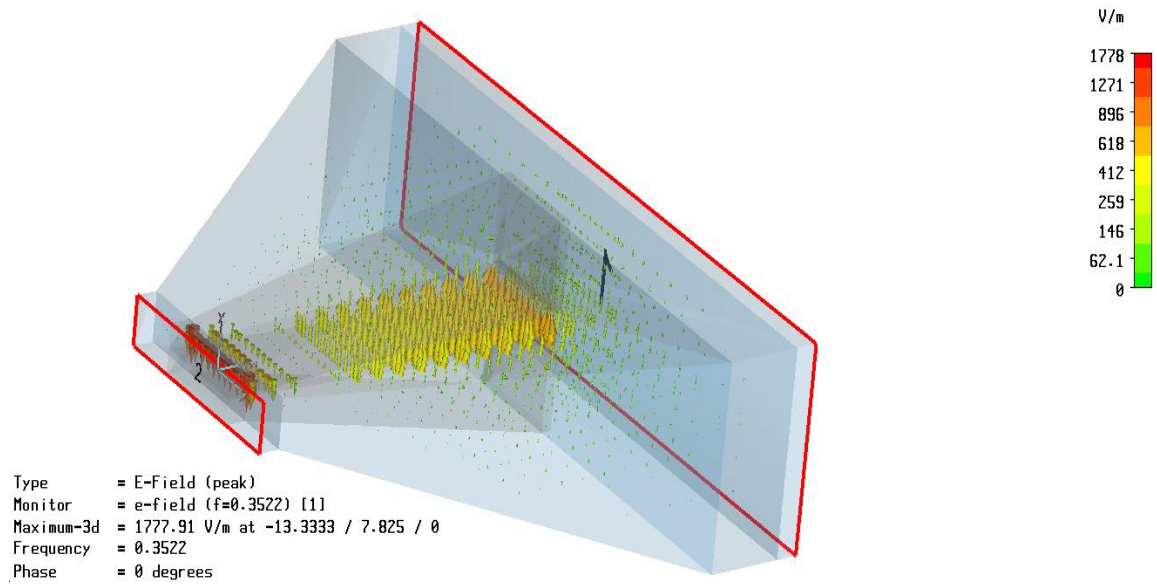


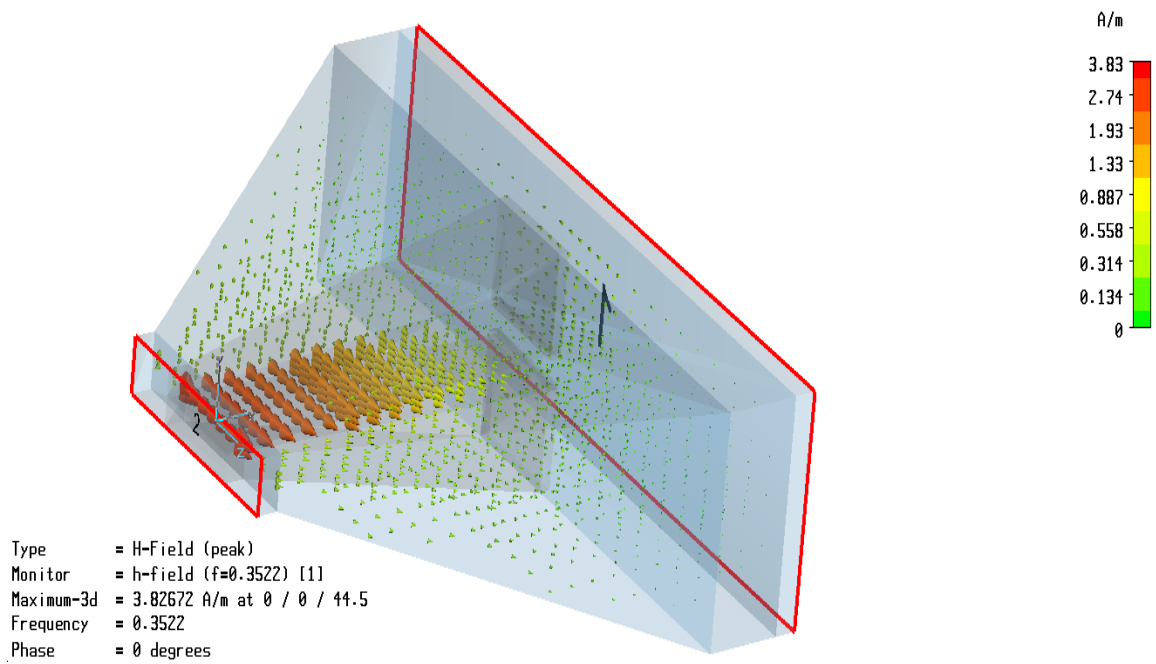
Fig. 4.23 Return loss plots for straight ridge coupler and tapered ridge coupler.

4.6.5 Comparison of multipacting behavior

Tapered ridge couplers are prone to multipacting problems [45]. However, it will be important to briefly discuss the multipacting behavior of straight ridge and tapered ridge couplers. Multipacting scaling laws described in [61] have been used by many researchers for coaxial lines [62] and for rectangular waveguides [63]. In general, two side multipacting power levels in coaxial and rectangular waveguides scales as $f^4 d^4$, where ‘f’ is the frequency and ‘d’ is the gap between multipacting surfaces. Recently, scaling laws have been reported for multipacting onset in ridge waveguides [64]. The scaling laws for ridge waveguides reported in [64] are used here to carry out multipacting comparison at the design frequency of 352.2 MHz.

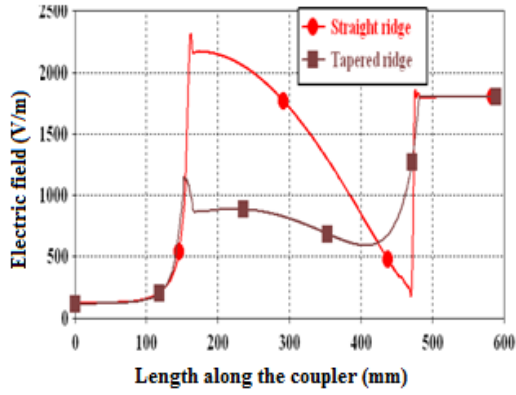


(a)

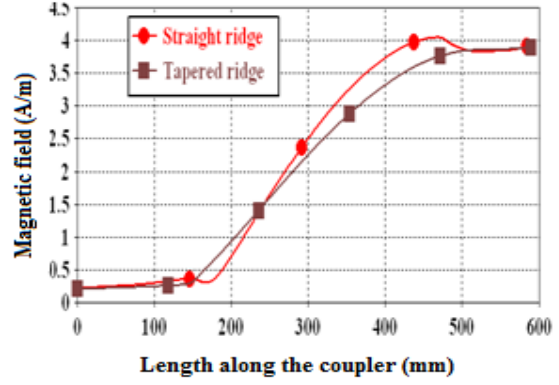


(b)

Fig. 4.24 Simulated arrow plots of (a) electric field and (b) magnetic field for tapered ridge coupler.



(a)



(b)

Fig. 4.25 Variation of (a) electric field (V/m) and (b) magnetic field intensity (A/m) along the coupler length for tapered and straight ridge coupler.

As the straight coupler consists of rectangular waveguide input and two ridge waveguide sections (central ridge and end ridge), there should be three distinct power levels at which multipacting can start. In the tapered ridge waveguide, central ridge gap changes along the length and hence multipacting onset will have many power levels. Such behavior has also been observed in tapered ridge waveguide couplers [45].

The multipacting onset levels for the straight ridge and tapered ridge are calculated using scaling laws given in [64]. For straight ridge coupler, multipacting onset voltage is estimated to be around 55 V and 300 V for end ridge and central ridge respectively. The corresponding power levels are calculated by CST-MWS port simulation with 1 W input power for end ridge and central ridge sections. As the end ridge and central ridge gaps are known, the voltage levels can be estimated from electric field plots of Fig. 4.25(a). The voltage level varies from 25.3 V to 2.3 V along the central ridge section of straight ridge coupler. Similarly, it varies from

17 V to 2.8 V in the central ridge section for tapered coupler. Hence, corresponding power level for multipacting voltages levels can be calculated. For input rectangular waveguide, reported data for WR1600 waveguide at 476 MHz [63] is used for scaling to WR2300 half height waveguide. The calculated multipacting onset power levels are summarized in the Table 4.12.

Table 4.12 Comparison of multipacting power levels

Coupler Type	Multipacting onset Power level in rectangular WG (kW)	Multipacting onset Power level in central ridge WG (kW)	Multipacting onset Power level in end ridge WG (kW)
Straight ridge	22.4	0.57 to 17	0.38
Tapered ridge	22.4	0.38 to 17	0.38

The multipacting onset takes place in the end ridge section at very low power level of 0.38 kW in both couplers as end ridge is same. The multipacting onset in central section takes place at power levels of 0.57 kW and 0.38 kW in straight ridge and tapered ridge coupler respectively. Multipacting onset in central section moves towards end ridge side as the power level is increased up to 17 kW in straight ridge coupler. This behavior will be more complex in central ridge section of tapered coupler because onset voltage also decreases with gap. The multipacting onset takes place in rectangular waveguide input of couplers at 22.4 kW.

From these studies, we can conclude that both coupler's are equally prone to the multipacting onset. As the couplers are expected to work at high power levels of 250 kW, both designs will

suffer from multipacting. RF conditioning will be required to achieve designed power levels. Prediction of higher order multipacting levels in these couplers will need further numerical and experimental studies.

4.6.6 Conclusions for comparative analysis

The tapered ridge transition is compared with the straight ridge transition for power couplers of accelerator cavities. The EM analysis results for the return loss and the frequency variation of tapered coupler are compared with the straight ridge coupler. The insertion loss, sensitivity of transmission phase shift with dimensions and frequency, return loss bandwidth and local field enhancements are also discussed. It is found that the tapered coupler has some desirable characteristics like lower RF losses, higher return loss bandwidth, lower variation in phase and lower fields in the central region. These studies will help the RF power coupler designers in choosing the desired ridge waveguide based coupling structures for accelerator cavities.

4.7 FABRICATION AND CHARACTERIZATION OF STRAIGHT RIDGE WAVEGUIDE COUPLER

4.7.1 Introduction

After carrying out detailed design studies on straight ridge and tapered ridge transitions, two no. of straight ridge transitions are fabricated. The dimensions of the transitions are same as given in Table 4.1 They are connected back to back for RF measurements using a VNA. The benefit of this characterization technique is that non standard matched load in ridge configuration is not needed at the ridge waveguide output. In standard high power testing techniques, a separate test

cavity is required [102]. The proposed technique can also be used at high powers also by using a RF window at input and output of the WR2300 half height waveguide. The output of the waveguide can be connected to a high power load which is available as a standard product. The tuners are used to bring the return loss to better than -30 dB at desired frequency of 352.2 MHz.

4.7.2 Studies on the EM fields and return loss

The schematic of side view of two couplers connected for RF measurements is shown in Fig. 4.26. The tuners are named as ‘Te₁’ and ‘Tm₁’ for the first coupler and ‘Te₂’ and ‘Tm₂’ for the

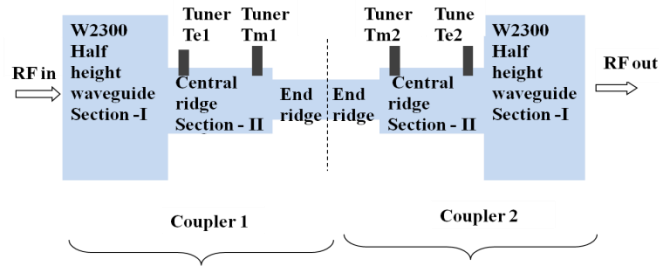
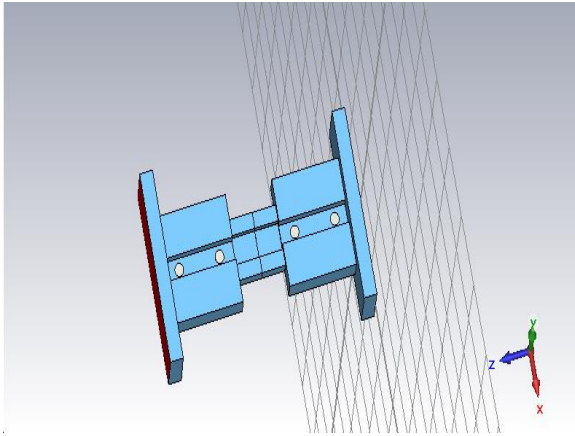
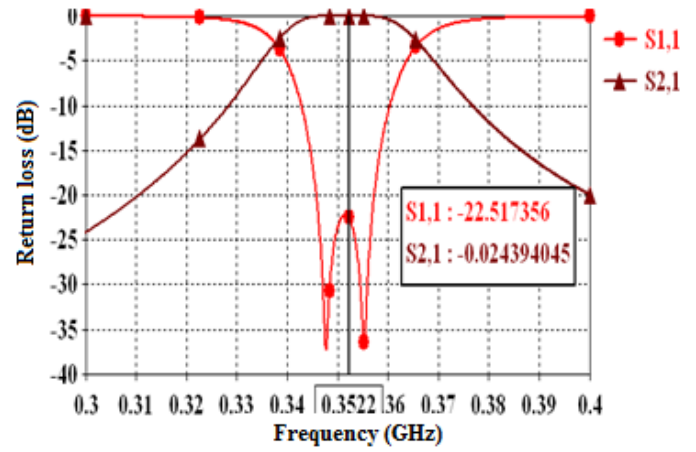


Fig. 4.26 Schematic of two couplers connected for RF measurements

second coupler. The simulated model and return loss plot for the connected transitions is given in Fig. 4.27(a) and (b) respectively. We can see that two dips appear in the return loss characteristics. These dips appear at different frequencies than the original frequency of single coupler, which had a single dip at 352.2 MHz. However, during back to back testing, it is found that minima of return loss shifts from the designed frequency to two distinct frequencies. This happens because two coupling transitions act as two single mode coupled resonators. Depending on their individual resonance frequencies and coupling provided by intermediate matching section, two distinct dips are obtained.



(a)



(b)

Fig. 4.27 CST-MWS model of (a) couplers connected to each other and (b) S parameter plots for the couplers.

It can also be observed that return loss at the desired frequency of operation (i.e 352.2 MHz) is poorer than that at other two dips at 348.4 MHz and 355.2 MHz. As discussed earlier, because of changes in dimensions during manufacturing, the return loss at the desired frequency can further degrade and hence back to back testing is not possible. The tuners are useful in that situation as discussed in following sections. To study the EM distributions in detail, a line plot of electric and magnetic fields on the centre line running along the couplers is obtained. These plots are shown in the Fig. 4.28.

These are obtained by CST Microwave Studio for input peak power of 1 W at port 1. These fields can be easily scaled for the full power operation at 250 kW CW, 352.2 MHz. For example, maximum electric field of about 22 V/cm (2200 V/m) at 352.2 MHz is obtained from Fig. 4.28a. As full power operation will be at 250 kW CW, (i.e. 500 kW peak), maximum peak electric field

along the center line will be approximately 16 kV/cm. As the coupler is symmetrical about the center line, global maximum electric field will be approximately of same value. This can be confirmed from Fig. 4.5 where electric field is plotted on all parts of the coupler.

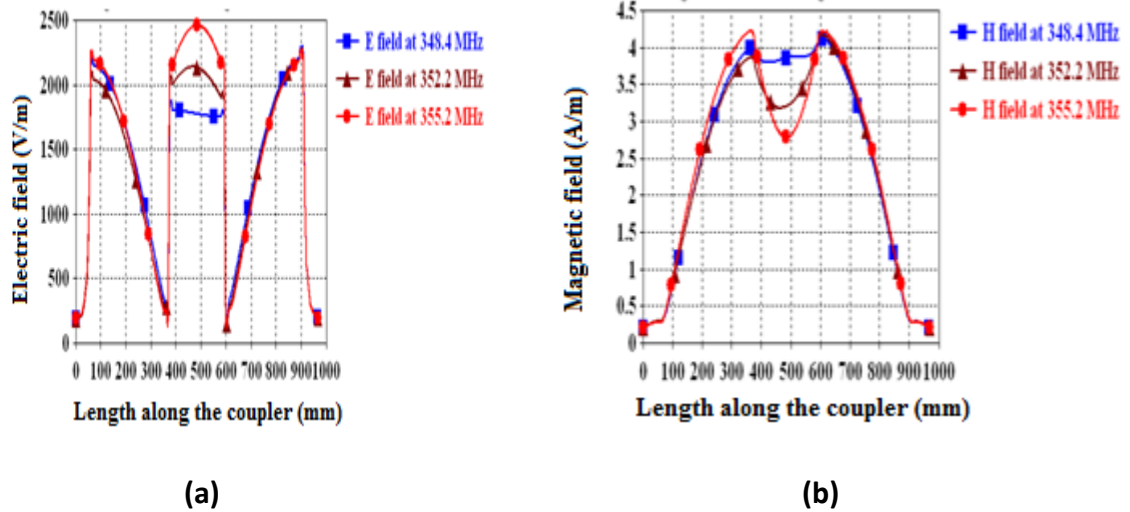


Fig. 4.28 Field plots along the center line of couplers for (a) electric field at frequencies of minimum return loss and at desired frequency of 352.2 MHz and (b) corresponding plots for magnetic field along the length.

Tuners are proposed and discussed in detail for the single ridge waveguide transition in Sections 4.1 to 4.6. During simulations, tuners were inserted or withdrawn to optimize the return loss at the desired frequency of 352.2 MHz. As discussed earlier, the tuner near the WR2300 WG is named as ‘ T_e ’ tuner whereas tuner near the end ridge is named as ‘ T_m ’ tuners. The tuners are cylindrical metallic rods which can move into the central ridge gap (+ve direction) or can be withdrawn (-ve direction). We can see from Fig. 4.29 that after tuning, return loss could be improved to -36.85 dB.

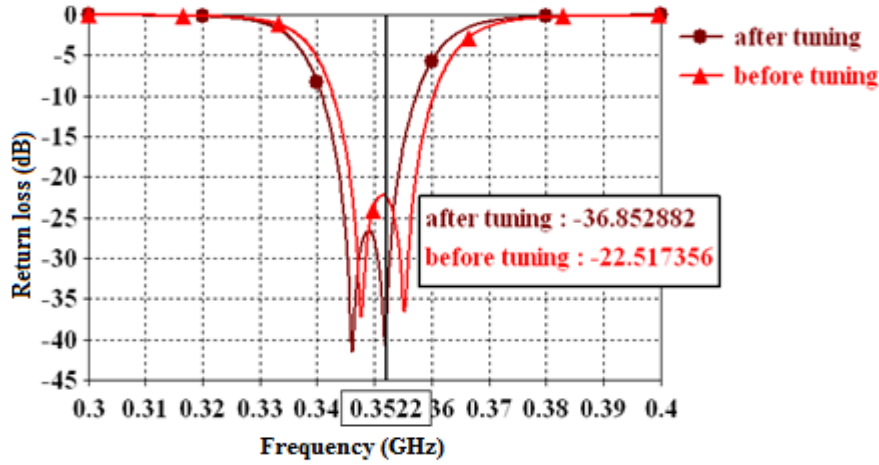


Fig. 4.29 S parameter plots for ridge transitions connected back to back.

The EM plots at 352.2 MHz are also obtained from CST-MWS after tuners are applied. We can notice from Fig. 4.30(a) that the electric field increases at ‘ T_e ’ tuner locations as they are inserted into the ridge gap. The ‘ T_m ’ tuners are withdrawn during tuning. This effect can be seen from Fig. 4.30(b) as the magnetic field dips at the ‘ T_m ’ tuner locations.

Exact values of tuner movement and their direction (i.e. insertion or with-drawl) are finalized by using iterative solver runs to obtain better return loss at 352.2 MHz. We can see that there is no gross perturbation of EM fields after tuning except at localized positions near tuners. This implies that back to back testing can be used for high power conditioning of these transitions even after tuners are applied. The conditioned couplers with tuners can be subsequently used for feeding high RF power to the accelerator cavity. However, individual coupler when connected to the cavity may need different tuner depths.

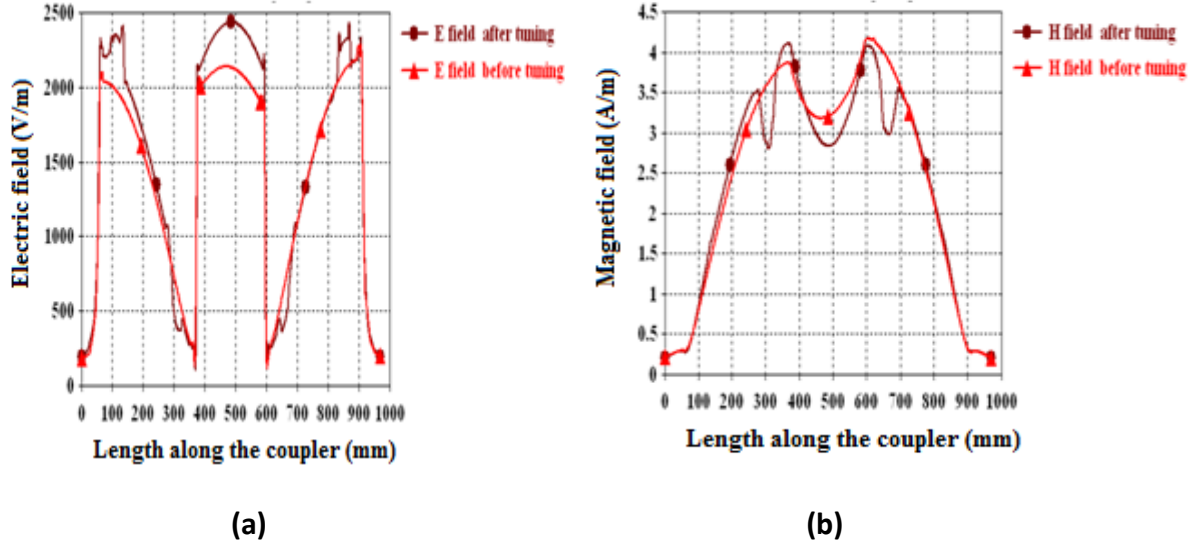


Fig. 4.30 EM field magnitude plots before and after tuning for (a) electric field (V/m) at 352.2 MHz and (b) corresponding magnetic field in A/m along length.

4.7.3 Fabrication and RF measurements

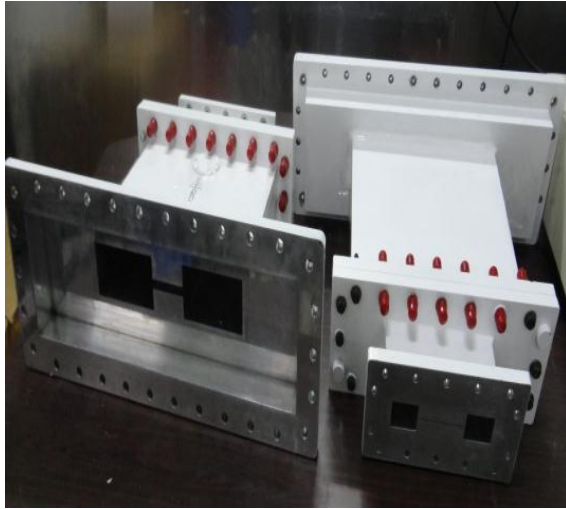
In order to verify the tuner effectiveness using RF measurements, two prototypes of ridge waveguide transitions were fabricated using aluminum as shown in Fig. 4.31.

The ridge waveguide transition can be seen as viewed from WR2300 side and from end ridge side in Fig. 4.31(a). WR2300 to N type adapters are used for connecting the two coupler transition ends to VNA as shown in Fig. 4.31(b). EM simulations are performed for various tuner depths compared with the RF measurements. The tuner 'Te₁' is inserted in one transition and its overall effect of two return loss minima frequencies f_1 and f_2 is noted. We can see from Fig. 4.32 that the simulated and measured trend is same. However, an offset in frequencies is found during measurements as compared to simulations. This shift can be attributed to the manufacturing and joining processes which can change the dimensions of the fabricated structure.

Table 4.13 Dimensions and tolerances of fabricated aluminum couplers.

Parameter	Description	Specified Value (mm)	Measured Value on Coupler1	Measured value on Coupler 2	Expected Thermal expansion for aluminum (mm) at 50 deg. C*
<i>w</i>	WR2300 width	584.2+-0.2	584.3	584.3	0.650
<i>h</i>	WR2300 height	146.05+-0.2	146.1	146.1	0.170
<i>wl</i>	Input Port length	60+-0.2	50	50	0.070
<i>c-ow</i>	Central section-overall width	334+-0.2	334.1	334.15	0.380
<i>cw</i>	Central ridge width	69.4+-0.1	69.45	69.4	0.080
<i>cl</i>	Central ridge length	315+-0.2	315+0.1	315	0.350
<i>cg</i>	Central ridge gap	11+-0.1	10.9	10.9	0.013
<i>ch</i>	Central ridge height	64+-0.1	64.05	63.95	0.074
<i>ew</i>	End ridge width	89+-0.1	89.1	89.05	0.100
<i>e-ow</i>	End section-overall width	189+-0.2	189	189	0.220
<i>eg</i>	End ridge gap	1.55+-0.05	1.55	1.56	0.002
<i>eh</i>	End ridge height	35+-0.1	35.03	35	0.040
<i>el</i>	Output Port length	60+-0.2	50.1	50.15	0.100
Corner radius and rounding at edges = 0.5 mm					

*Linear thermal expansion mentioned is for aluminum (linear thermal expansion coefficient = 0.000023 m/m°C) in un-constrained conditions.

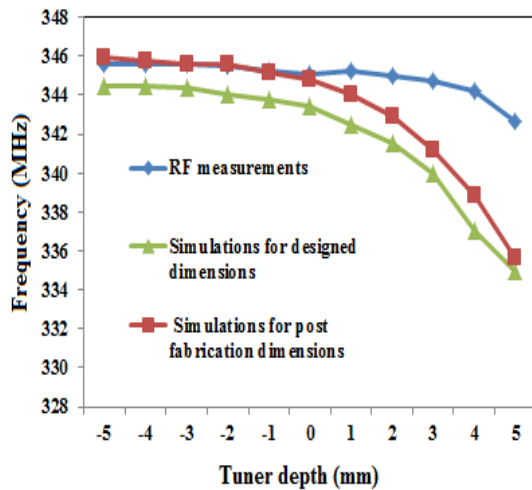


(a)

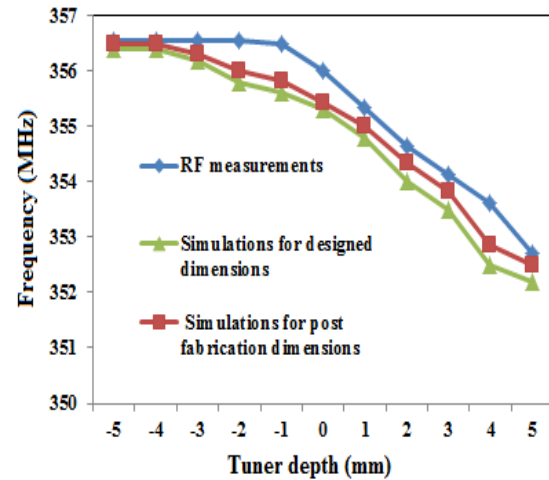


(b)

Fig. 4.31 Ridge waveguide transitions (a) viewed from input and output end and (b) transitions connected to network analyzer with WR2300 to N type adapters.



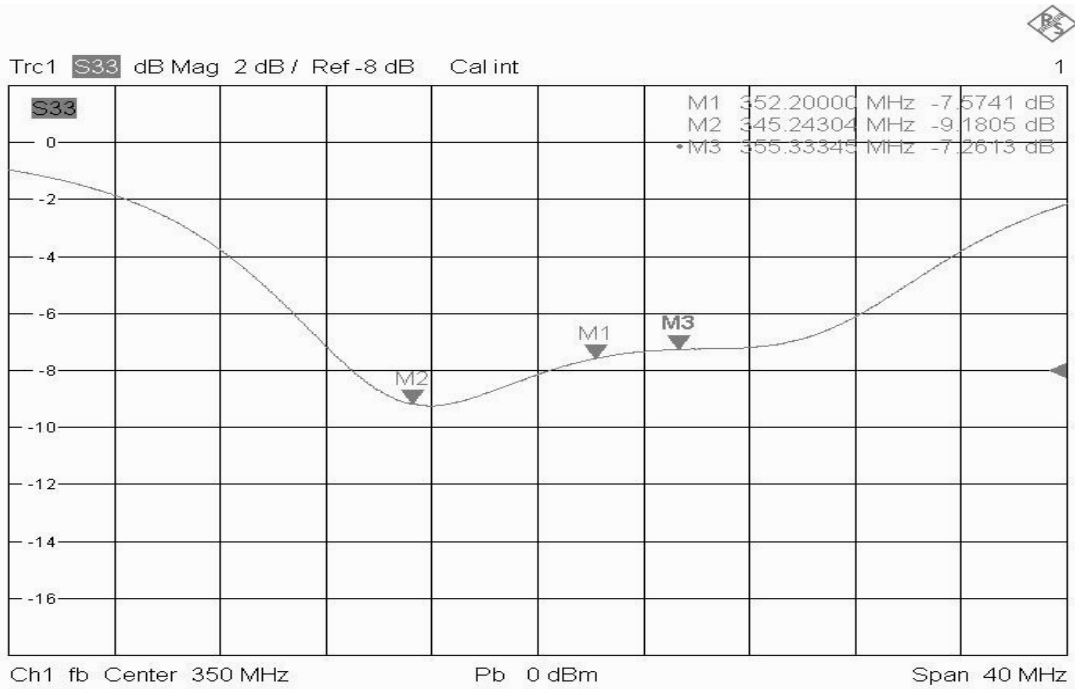
(a)



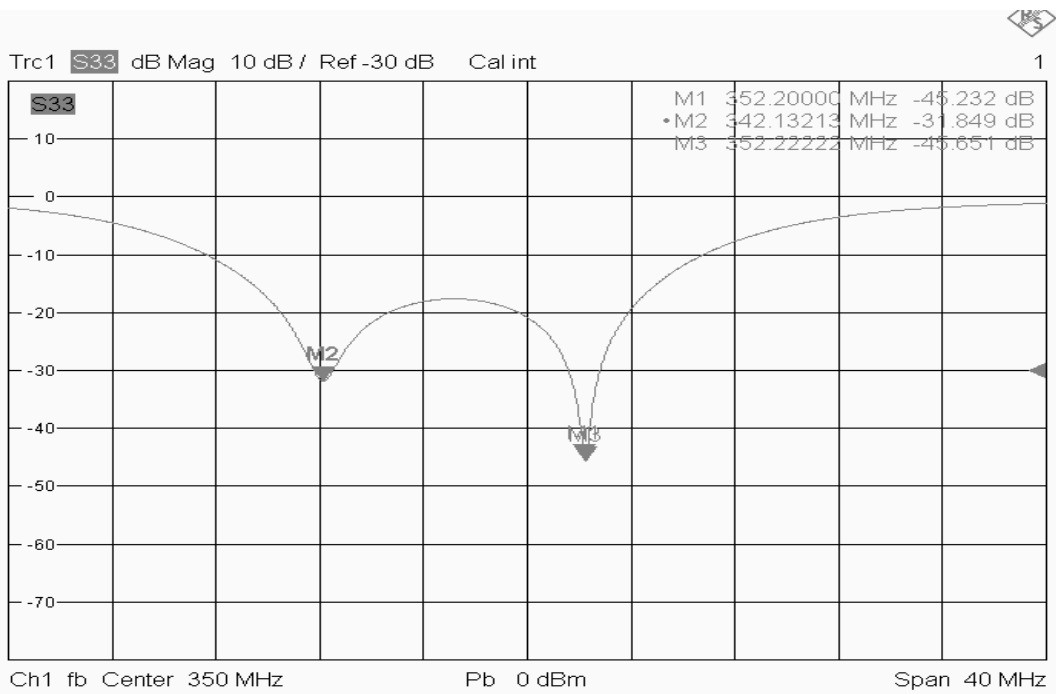
(b)

Fig. 4.32 Simulations and measurements for (a) effect of tuner ' Te_1 ' movement on first return loss minima frequency ' f_1 ' and (b) effect of tuner ' Te_1 ' movement on second return loss minima frequency ' f_2 '.

Though this shift in the dimensions during manufacturing is not desirable and should be restricted, the tuners can be applied to restore the return loss degradation at desired frequency of 352.2 MHz. We can see from measurement plots Fig. 4.33(a) that the return loss of manufactured structures degraded to -7.57 dB at 352.2 MHz. However, after applying the tuners, the return loss could be improved to -45.23 dB at the desired frequency of 352.2 MHz as shown in vector network analyzer plots of Fig. 4.32(b). The Table 4.13 shows the dimensional specified dimensional tolerances for the fabrication of couplers. The dimensions obtained after manufacturing are also shown. The calculations for dimensional changes because of thermo-structural effects show that simulations studies have covered a wide range. The simulations for specified dimensions and post fabrication dimensions is compared with RF measurement values for fabricated couplers along with optimized tuner positions. The results are summarized in Table 4.14. We can notice from Table 4.14 that the tuners can be effectively used to obtain the acceptable return loss at desired frequency. It can be noted that there is small difference in tuner depths used during simulation and measurements. This may be attributed to the fact that it is difficult to exactly measure the interior dimensions at all locations of the coupler after fabrication exactly. The couplers were aligned with the bolted joints without alignment pins. This can also lead to some misalignment between two couplers during measurements. However, the overall fabrication accuracies are found to be better than ± 100 microns for measurable coupler dimensions.



(a)



(b)

Fig. 4.33 Return loss plots obtained with VNA for (a) before tuning and (b) after tuning.

Table 4.14 Summary of simulated and measured values of frequency, return loss and tuner depth.

Parameter	Simulated value (for specified design)	Simulated value (for post fabrication dimensions)	Measured value
Frequency- 1 (before tuning)	343.34 MHz	344.7 MHz	345.1 MHz
Frequency- 2 (before tuning)	355.28 MHz	355.4 MHz	355.34 MHz
Return loss at 352.2 MHz (before tuning)	-17.36 dB	-18.1 dB	-7.57 dB
Return loss at 352.2 MHz (after tuning)	-41.0 dB	-25 dB	-45.23 dB
Tuner Te_1 depth	2 mm	4 mm	5 mm
Tuner Te_2 depth	0 mm	-4 mm	0 mm
Tuner Tm_1 depth	0 mm	0	0 mm
Tuner Tm_2 depth	0 mm	0	0 mm

4.7.3 Thermal aspects of coupler design

In-order to estimate the temperature rise on the ridge waveguide coupler, coupled RF-Thermal analysis is carried out using COMSOL Multi-physics, a FEM based solver [98]. For 250 kW RF input on end ridge waveguide, maximum temperature is 32 deg. C for ambient temperature of 20 deg. C. In this simulation, a convective heat transfer coefficient of 1000 W/m²K is assumed on external surfaces. The temperature display is shown in Fig. 4.34.

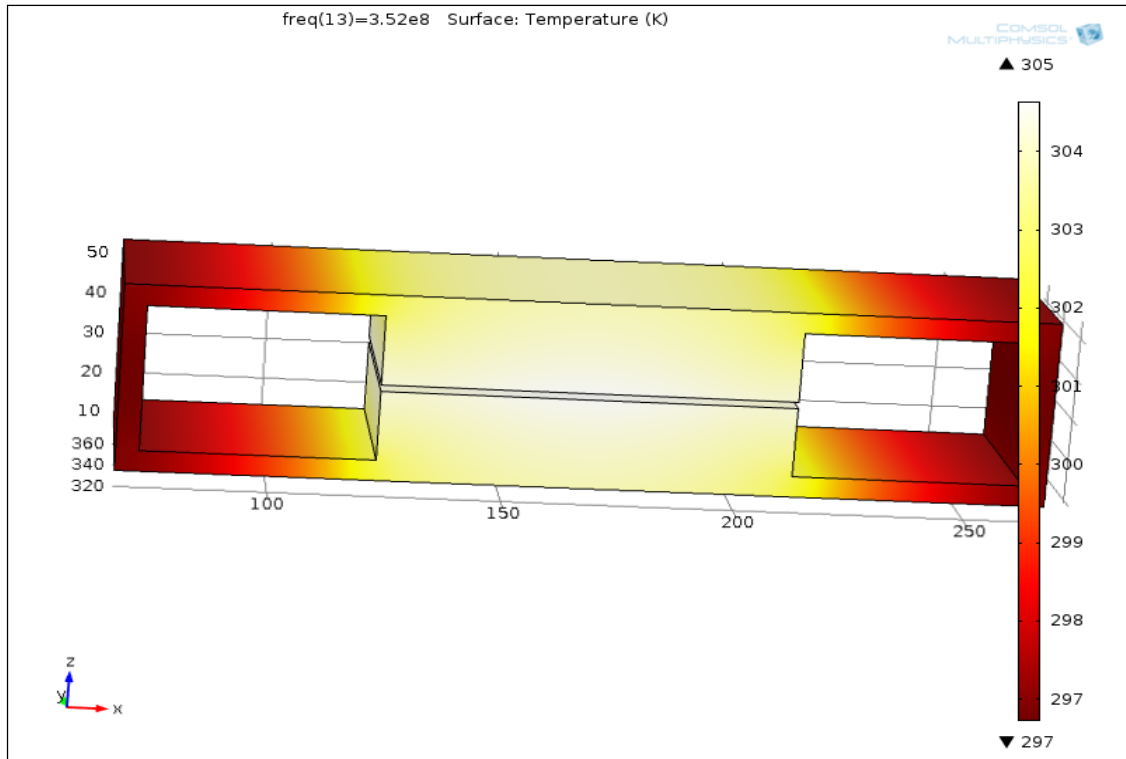


Fig. 4.34 Temperature distribution on end ridge waveguide with uniform cooling on outer surfaces.

The complete ridge waveguide assembly is also simulated to obtain an estimate of temperature rise. It is found that maximum temperature rise is below 50 deg. C. The temperature rise is high because higher thickness of end section. The copper conductivity ensures that overall temperature difference on coupler surfaces is less. Here, uniform cooling ($1000 \text{ W/m}^2 \text{ K}$) is assumed on all external surfaces. The temperature distribution is given in Fig. 4.35. It is important that the maximum coupler and iris surface temperature is kept below 50 deg. C with the water cooling arrangement.

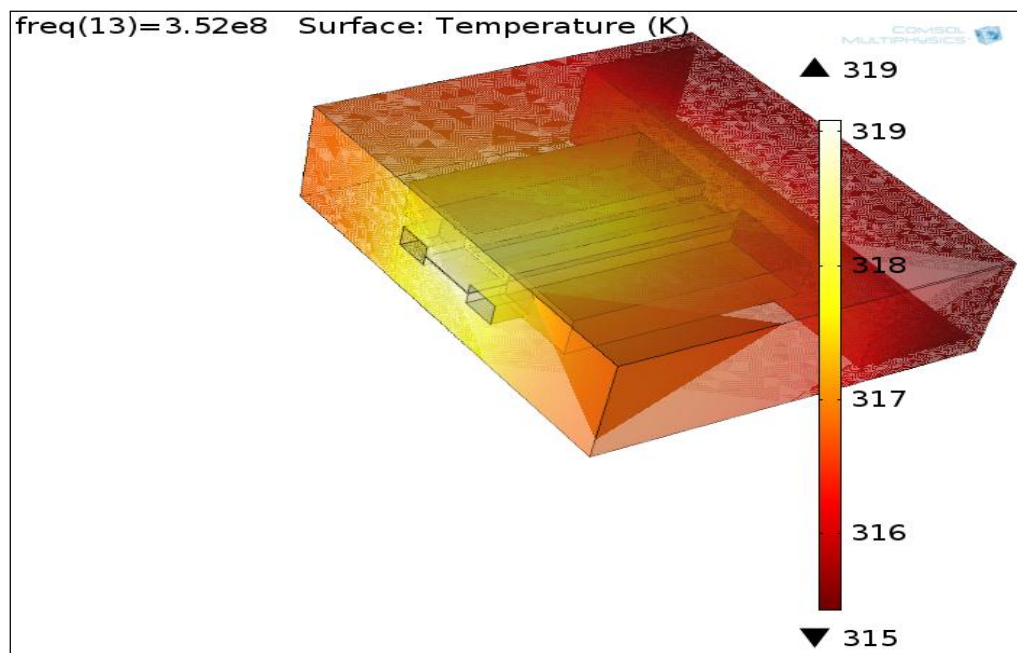


Fig. 4.35 Temperature distribution on complete coupler assembly

4.9 SUMMARY

A RF characterization procedure is described for ridge waveguide transitions without using a cavity or ridge waveguide matched load. These transitions are also simulated for EM field distributions and return loss characteristics for back to back connection. It is shown by simulations and measurements that tuners are effective in taking care of dimensional changes

during manufacturing. The proposed simulations and measurements will be useful in conditioning these coupler transitions at high power by connecting them back to back. In such scenario, the other output can be terminated in a waveguide matched load which is available in standard sizes.

CHAPTER 5

DEVELOPMENT OF COAXIAL RF POWER COUPLERS AND RF TEST BENCH

5.1 INTRODUCTION

Coaxial couplers are widely used in high power accelerator cavities because of their compact size and ease of coupling variation by loop rotation or probe movement. These assemblies also incorporate an air to vacuum barrier (which is called RF window) for separating the cavity vacuum from the air side of incoming transmission line. Several window designs are used depending upon the geometry and fabrication choices. They are generally of planar (disc) type or cylindrical type. The impedance is matched either by providing chokes on inner and outer conductors or by optimizing the conductor sizes near the window. Two coaxial loop couplers with different window designs have been developed for Radio Frequency Qudrupole (RFQ) cavity of 400 keV deuteron accelerator at BARC [105]. The power requirements of these loop type couplers are 50 kW at 350 MHz for different duty cycles. First one uses a simple alumina disc and under cuts on inner conductor for impedance matching. This coupler is made in standard 1 5/8" EIA size without any forced air or water cooling. The other design uses two alumina disc type windows placed symmetrically around a shorted stub. The shorted stub is also used to circulate water to inner conductors so that the coupler can be used at high CW powers. This also ensures that coupler can be rotated for coupling tuning in off line conditions without shifting the location of flange for incoming line.

5.2 COAXIAL COUPLER WITH UNDER-CUT TYPE WINDOW

As the port size on the RFQ cavity is only 50 mm, a rigid 50 Ohm co-axial line with 1 5/8" EIA standard size is used. A coaxial loop type coupler has been developed for testing of accelerator cavities for LEHIPA Project at BARC. This RF coupler is designed to handle up to 50 kW RF power around 350 MHz with maximum 1% duty cycle. A disc type alumina window with undercuts on inner conductor is integrated in the coupler assembly for impedance matching. This design is simpler than choke type or undercut – overcut type impedance matching schemes for coaxial RF windows. Full wave EM analysis of RF window is presented. The window fabrication, testing, RF characterization and high power conditioning results are also discussed.

5.2.1 Existing coaxial window designs

Several window designs have been used for RF couplers in accelerator cavities. The window design can be cylindrical or disc type (in waveguide type couplers) or it can be cylindrical disc type in coaxial couplers. Excellent review of couplers and their RF window implementations is given in [13].

The capacitive discontinuity introduced by the alumina disc in coaxial couplers is generally matched by a choke type design on inner and outer conductors. A small section of short circuited coaxial line is formed on the inner and outer conductors near the alumina disc. This provides the necessary inductance and can be made to resonate with alumina disc's capacitance at desired frequency. A schematic of this design is shown in Fig. 5.1.

The model includes cylindrical outer conductor, inner conductor, alumina disc and machined cuts on inner conductor.

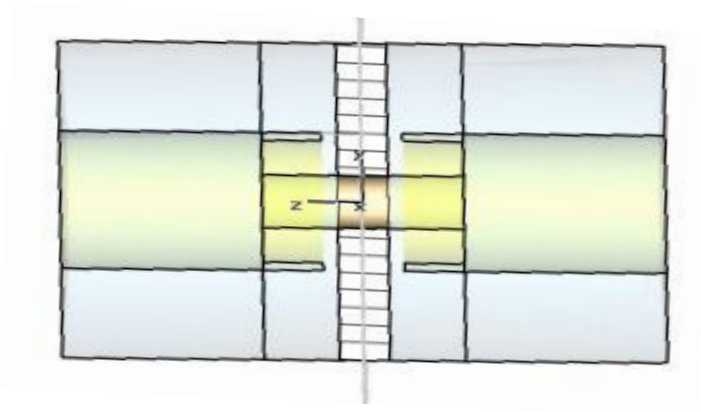


Fig. 5.1 Cut view of simulation model showing chokes on inner conductor.

This design is very useful as it is possible to tune the match frequency by varying the choke depth. However, it results in complex mechanical design and hence a simpler design is proposed in this work.

5.2.2 Proposed coaxial window design

The window is analyzed using full wave solver of CST MWS. Inner conductor diameter is decreased on both sides of the alumina disc. The small sections of transmission line on both side of capacitive disc provide the required inductance to compensate for additional capacitance of high purity alumina disc (99.5% purity with dielectric constant of 9.9).

5.2.2.1 Electromagnetic design of RF window

The cut view of the simulation model is shown in Fig. 5.2. The structure is optimized till the required match is obtained. The S parameter results with under-cuts matching is shown in Fig. 5.3.

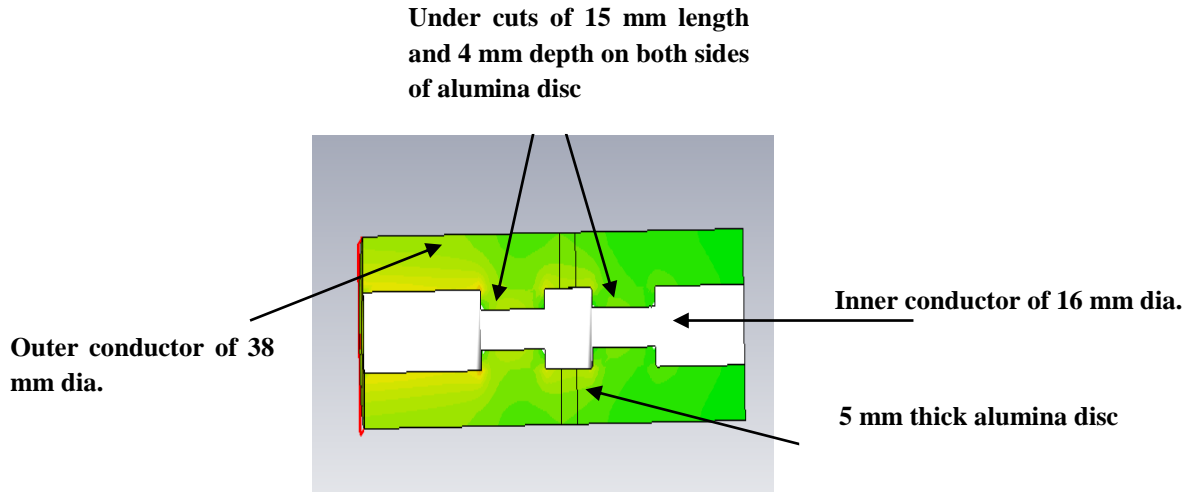


Fig. 5.2 Cut view of simulation model with cuts on inner conductor.

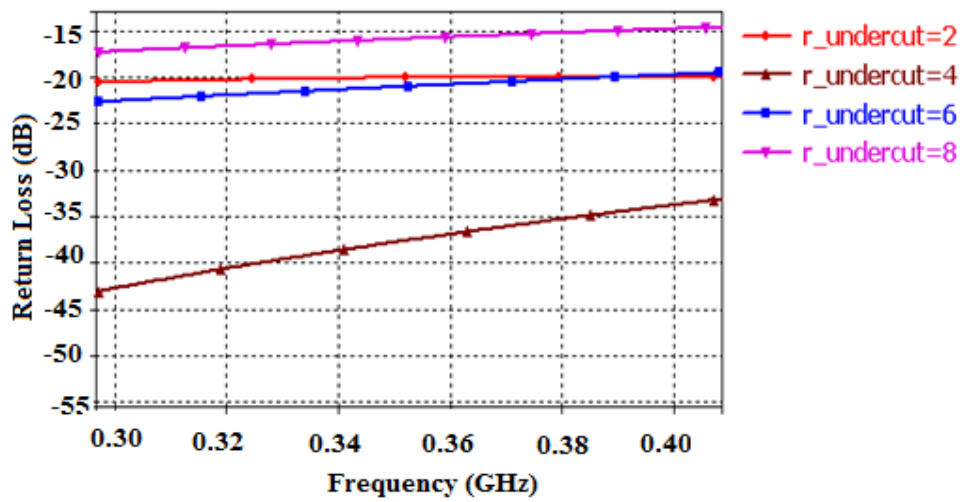


Fig. 5.3 S parameters of RF window for different radius at under-cut on inner conductor.

The radius of conductor at under-cut location is varied from 2 mm to 8 mm as shown in Fig. 5.3. It is observed that the optimum value of radius is 4 mm for minimum return loss. The return loss improves from -15 dB to better than -35 dB after matching with the under-cuts.

Dielectric loss in the high purity alumina window and RF loss on the copper inner and outer conductors results in temperature rise on the coupler. In order to simulate the heating effect, loss tangent of alumina disc is taken as .001 and dielectric constant as 9.8. The coupler with 1 5/8" standard copper conductors is simulated with COMSOL Multiphysics, a Finite Element Method (FEM) based EM solver [99]. This coupled EM-Thermal problem is simulated by applying 10 kW CW input RF power at input port and applying a matched boundary at port 2. Ambient temperature of 293K and natural cooling is assumed on the coupler. As can be seen from Fig. 5.4, maximum temperature rise of 74 deg. C is obtained on the inner conductor and inner region of alumina disc.

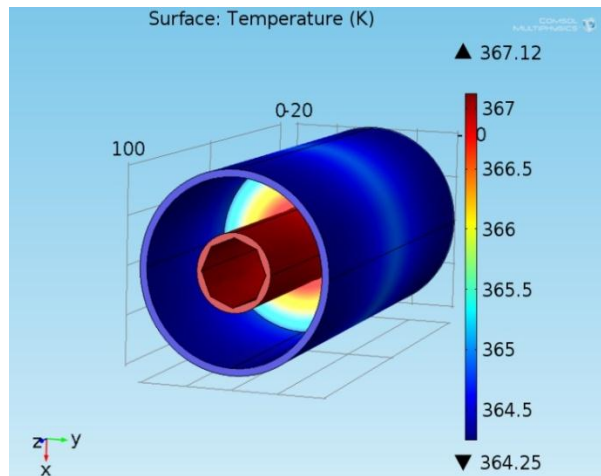


Fig. 5.4 Temperature profile on the coupler and alumina window for 10 kW input power.

As the coupler is not cooled, maximum CW power is kept below 500 W (50 kW Peak with 1 % duty cycle). This gives a temperature rise of less than 5 deg. C which has been verified with experiment.

As this window is a part of loop coupler assembly, the complete assembly is fabricated for testing at high powers. A typical view of simulation model of loop coupler on RFQ cavity is

given in Fig.5.5. The required loop area is optimized by external quality factor (Q_{ext}) simulations with Eigen Mode solver of CST- MWS. The simulations are performed to obtain the desired coupling for quadrupolar mode of RFQ cavity. A matched port is defined at the coaxial input. The loop area is optimized to obtain ' Q_{ext} ' of 4000 on RFQ cavity. From eqn. (3.16a), coupling coefficient of 1.5 is obtained for RFQ cavity with 6000 quality factor. The desired 'critical coupling' is obtained by rotating the loop. The loop is designed for over-coupling so that desired coupling can be obtained by rotating it.

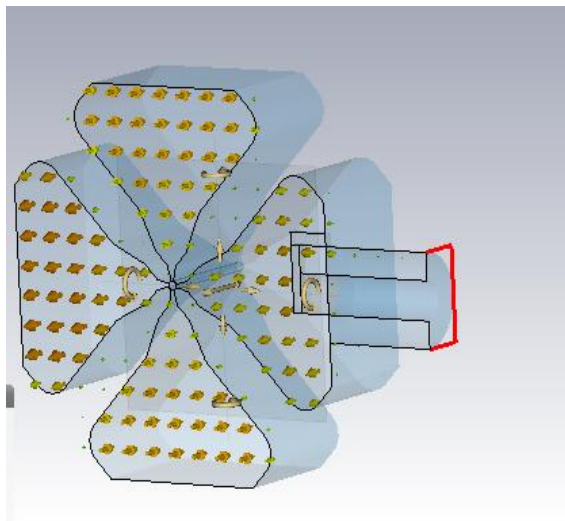


Fig. 5.5 Cut view of CST model for External Q simulation.

5.2.2.2 Fabrication and Vacuum Testing

Different coupler parts are made as per rigid coaxial 1 5/8" EIA standard. The inner conductor is made with ETP Cu in three parts so as to enable hydrogen furnace brazing of alumina disc. The loop and end flanges are brazed in second brazing cycle. The coupler view from input side is shown in Fig. 5.6(a). The white colored alumina window can be seen from input port. The loop is visible in Fig. 5.6(b).

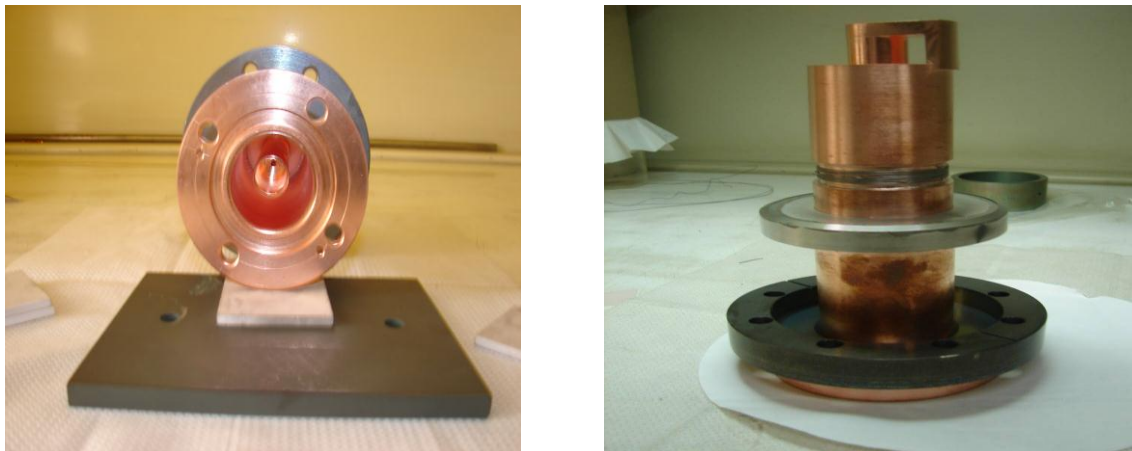


Fig. 5.6 View of (a) RF window and coupler from input side and (b) Loop coupler placed vertically.

After fabricating the coupler, window-coupler assembly is tested for any possible vacuum leaks. The assembly was mounted on a test fixture for vacuum leak tightness. A leak rate of better than 1×10^{-10} torr-liters/s is obtained. After the window is tested for vacuum leak rate, it is connected to a test cavity. Again, the whole system is tested for any possible leak rate as shown in Fig. 5.7.

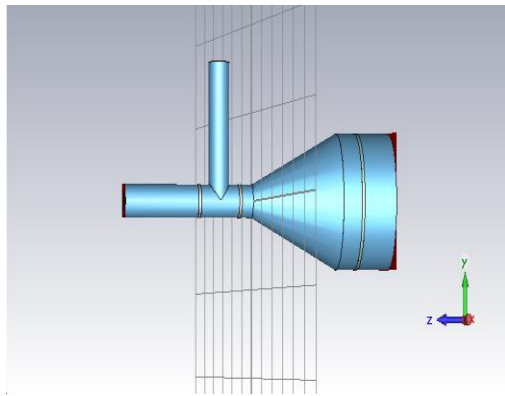


Fig. 5.7 RF window and coupler connected to test cavity for vacuum leak checking.

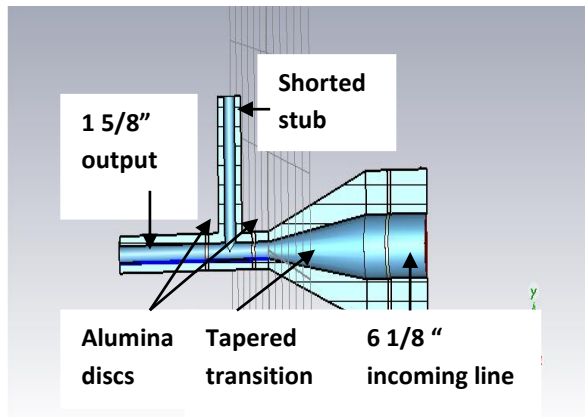
5.3 COAXIAL COUPLER WITH STUB LOADING

A coaxial loop coupler with EIA 6 1/8" input is designed for feeding RF power of 50 kW CW, 350 MHz. As the available port size on the RFQ cavity is only 50 mm, a tapered transition is used to change the 6 1/8" size to 1 5/8" size of coaxial line. The length of the taper is kept as 160 mm in-order to obtain return loss of better than -30 dB. Two high purity alumina discs of 5mm thickness are used on both sides of the shorted stub. The two discs provide a balanced support to the central conductor and provide double barrier in case one disc develops a vacuum leak. The length of the stub and distance of alumina discs from stub are optimized to obtain return loss of better than -30 dB. A CST-MWS simulation model of the coupler and its cut view are shown in Figs. 5.8(a) and (b) respectively. Return loss characteristics are given in Fig. 5.8(c). Bandwidth of ± 45 MHz is obtained for this coupler. The parametric studies for return loss with shorted stub length are given in Fig. 5.8(d). It is observed that return loss is better than -30 dB for ± 2 mm change in shorted stub length from optimized value of 157 mm.

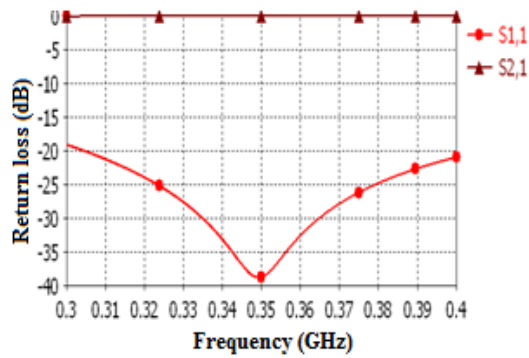
The coupler parts are brazed in several steps inside a brazing furnace. All coupler parts are made up of ETP copper except the vacuum flange. The vacuum flange with a conflate seal is made up of SS 304. The different brazed sub -assemblies of the couplers are shown in Fig. 5.9(a). The complete coupler assembly after brazing is shown in Fig. 5.9(b). The shorted stub is used to circulate water to a tube placed inside the inner conductor of assembly. The water flows to the channel and is collected back at the outlet. A water flow rate of 2 m/s will be sufficient to keep the maximum temperature rise to within 50 deg. C [100.]. Air inlet and outlet are also provided to cool the tapered part of coupler assembly. This coupler assembly has been also tested for any vacuum leaks.



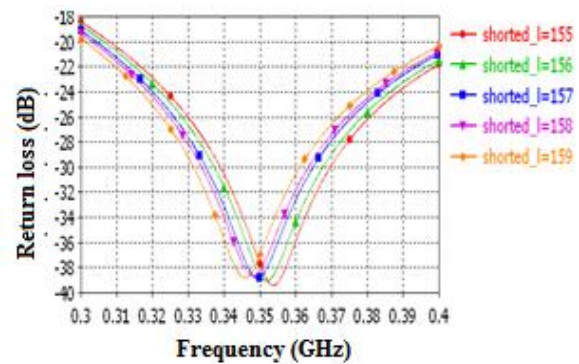
(a)



(b)



(c)



(d)

Fig. 5.8 CST Microwave Studio model of (a) coaxial stub loaded coupler; (b) cut view of the coupler assembly; (c) simulated return loss and transmission loss of the optimized coupler geometry and (d) variation of return loss with stub length.



(a)



(b)

Fig. 5.9 (a) Different coupler parts brazed separately and (b) complete coupler assembly after brazing.

5.4 TEST CAVITY DESIGN

Since the cavity is used as an intermediate medium to transfer power from coupler on port 1 to coupler on port 2, it should have minimum power loss while transferring power to output coupler. This will reduce the cavity cooling requirements. Also, output coupler will receive sizable amount of input power. Hence, both couplers can be conditioned together. The cavity should be tunable around 350 MHz preferably with ± 1 MHz tuning range. This can be achieved if the cavity is sufficiently over-coupled to the incoming inductive couplers.

5.4.1 Theory of over coupled couplers connected to a cavity

When a resonator is over coupled to two ports (input and output with same over-coupling), it can be used as a band pass filter. The return loss and insertion loss decreases as coupling increases. For a sufficiently over coupled cavity- coupler system, most of the input power entering the cavity travels to the output. Hence, the couplers under test can be connected to

port 1 and port2 of the cavity for their high power testing. A schematic of two loop couplers connected to the cavity is shown in Fig. 5.10. For two couplers of coupling coefficient β_1 and β_2 respectively, reflection coefficient Γ is given as [101].

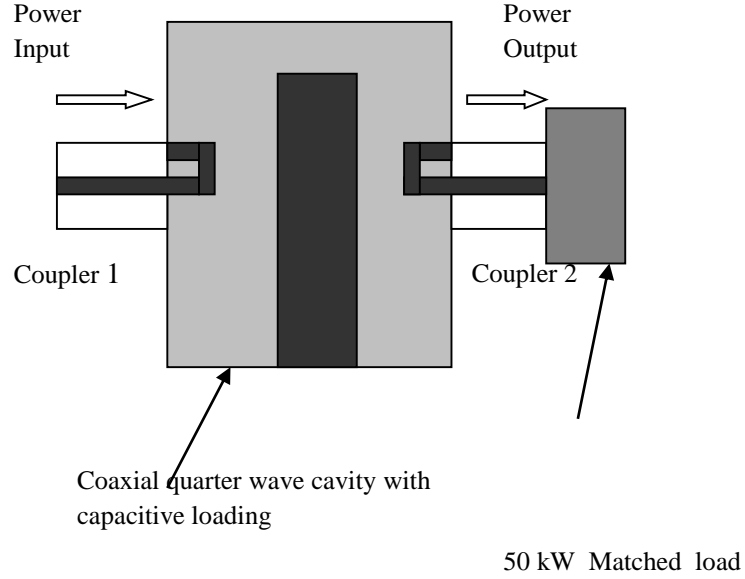


Fig. 5.10 Schematic of coupler test bench.

$$\Gamma_1 = \frac{\beta_1 - \beta_2 - 1}{1 + \beta_1 + \beta_2} \quad (5.1)$$

It can also be shown that [101]

$$\frac{P_{cavity}}{P_{coupler2}} = \frac{1}{\beta_2} \quad (5.2)$$

We can see from eqn. (5.1) that reflection coefficient becomes zero as β_1 is equal to $\beta_2 + 1$. We

can conclude from eqn. (5.2) that power deposited in the cavity is β_2 times less than outgoing power. Hence, it becomes very important to obtain sufficient over-coupling so that both couplers can be tested for transmitted power in the same set-up. Cavity acts as an intermediate power transformer from input to output coupler. As the external Q of loops is decided by RFQ cavity, the design goals for test cavity were good quality factor with maximum coupling.

5.4.2 Electromagnetic design of cavity

The cavity is analyzed using Eigen Mode solver of CST MWS. The cut view of the simulation model is shown in Fig. 5.11. The model includes cylindrical outer conductor, inner conductor, two diametrically placed ports, vacuum port and two tuner ports on end flange. The outer conductor diameter of 155 mm and inner conductor diameter of 67 mm is chosen. The end gap between the inner conductor and the shorting end plate is varied during successive runs of modal solver to obtain the desired frequency of 350 MHz. The change in the frequency with every 1 mm shift in the gap is found to be around 5 MHz. Hence, the cavity is fabricated with smaller gap (hence lower frequency) so that it can be tuned to the desired frequency after post fabrication machining. Moreover each tuner is inserted up to 15 mm inside during simulations.

The external quality factor is analyzed using the Modal solver of CST MWS by defining a matched boundary at the coupler port. The intrinsic quality factor is calculated by post-processing calculator of CST MWS. The cavity material is chosen as Stain less Steel during these calculations. The coupling coefficient (β) can be calculated as $\beta = Q_o/Q_{\text{ext}} = 3544/1212 = 2.92$. For a copper cavity, the quality factor will be higher and coupling coefficient of more than 5 is expected. The higher coupling coefficient is important as power shared between cavity and output coupler will be in the ratio of 1: β . Hence, for a 50 kW input power, cavity will dissipate

10 kW and remaining 40 kW will flow through the output coupler and finally dissipate in the matched load.

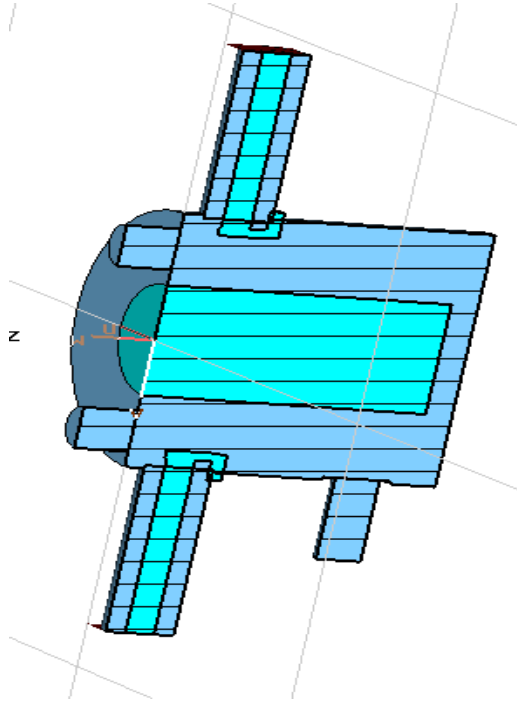


Fig. 5.11 Cut view of simulation model showing inner conductor and loop couplers.

Two tuner ports are provided in the magnetic field region for tuning the cavity frequency. As the electric field concentration is high in the capacitive gap, the sharp corners are rounded to 1 mm radius. A vacuum port is also included in the simulations.

Table 5.1 shows the values of the optimized parameters for required frequency, coupling and external quality factor.

Table 5.1 Dimensions of quarter wave test cavity.

Parameter	Value
Resonant frequency	350.0 MHz
Quality factor (Q_o)	3544
External Q (Q_{ext})	1212
Cavity length	203 mm
Outer conductor diameter	155 mm
Inner Conductor diameter	67 mm
End gap	16 mm
Port 1 diameter	50 mm
Port 2 diameter	50 mm
Tuner port diameter	25 mm
Tuner rod length (variable)	15 mm
Vacuum port diameter	25 mm

A typical peak electric field arrow plot of the cavity is shown in Fig. 5.12. The plot is obtained from the Modal solver of CST-MWS for 1 J energy stored in the cavity. Maximum electric field occurs in the capacitive gap.

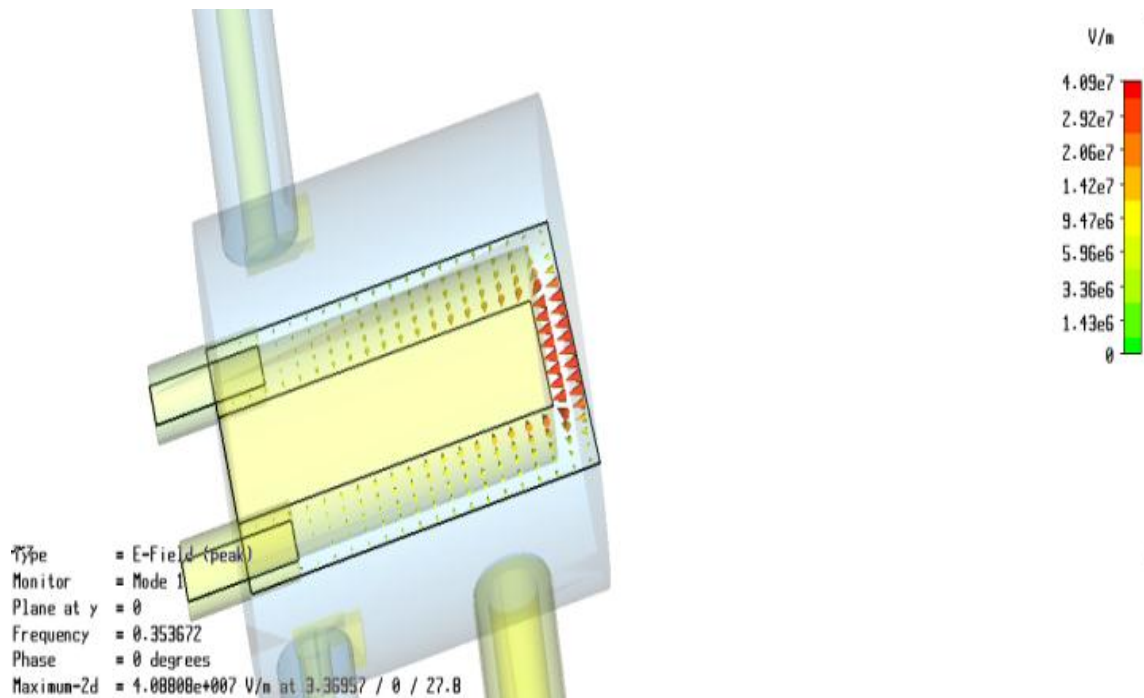


Fig. 5.12 Electric field plot on a cut section of the cavity.

5.4.3 RF measurements on fabricated cavity

5.4.3.1 Measurements with 15 mm end gap

The low power prototype is fabricated using SS to verify the simulations. Fig. 5.13 shows the fabricated cavity connected to VNA. The S_{21} parameters were measured by exciting the cavity with very small loops on coupling port.

The resonance frequency for 15 mm gap is measured to be 344.5 MHz whereas as the simulated value is 346.7 MHz. The difference (0.63%) can be due to the dimensional in- accuracies during manufacturing. The gap is kept smaller in the beginning so that required frequency can be obtained by machining the gap. Required frequency is obtained by machining the gap to 16 mm.

The measurements were performed with small loops on N Type connectors. The N type connectors were mounted on a hollow cylindrical port blocked with a plate, whereas simulations were performed with actual prototype couplers of 50 ohm, 1 5/8" rigid coaxial type.



Fig. 5.13 Fabricated quarter wave resonator connected to VNA for RF measurements.

The tuning results with end gap are summarized in Table 5.2. The desired frequency of 350 MHz is obtained by introducing the end tuners. The frequency tuning with end tuners is explained in next section.

Table 5.2 Measured and simulated results for different end gaps of quarter wave test cavity.

End Gap (mm)	Resonant frequency		
	CST Simulation	Measured	Error (%)
15	346.70	344.50	0.63
16	351.69	350.77	0.26

5.4.3.2 Tuning of the cavity with end tuners

Two tuner port ports are provided at the shorted end to do the final adjustments to resonance frequency. The rod type tuner is successively taken out in steps of 5 mm and corresponding frequency is measured. The measured values are compared with simulated values as shown in Fig. 5.14. A difference of approximately 0.5% is obtained between simulations and measurements. The difference can be due to small gap between couplers and port's inner diameter which is not considered in simulations. Also, there is a strong dependence on end gap as 100 microns can shift the frequency by 0.5 MHz. Considering all these facts, a good agreement has been found between measured and simulated values. As the high power coaxial couplers are equipped with a RF window for vacuum isolation, it will require vacuum leak free welds on the cavity. The prototype SS cavity was tested for vacuum leak tightness with helium leak detector. A leak rate of better than 1×10^{-10} std torr litres/sec was obtained during these tests which is within the acceptable limit.

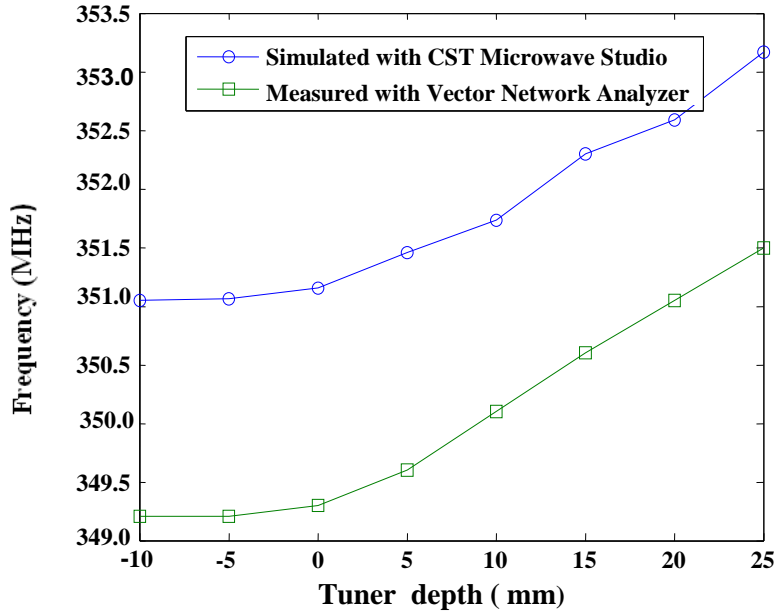


Fig. 5.14 Simulated and measured values of resonance frequency with tuner outward movement.

5.5 HIGH POWER CONDITIONING OF COUPLERS

High power conditioning of couplers is done generally on dedicated test benches [102, 103]. Hence, the quarter wave resonator described in previous section is used to test the window-coupler assembly at high power levels. The fabricated window and coupler assembly is coupled to the test cavity and vacuum level of better than 1×10^{-6} torr is obtained. The measured S_{11} parameter is shown in Fig. 5.15. The return loss of better than -30 dB is obtained at cavity's resonant frequency of 350.2667 MHz. It is important to note that coupling to the cavity depends on loop size and its orientation. The desired critical coupling could be obtained by rotating the loop. As the cavity quality factor is measured to be around 1200, the coupler is tested by rotating the loop to obtain critical coupling. The coupler is tested in transmitted power mode.

Following are the general guidelines followed for high power conditioning of couplers.

1. Start with 0.1 ms RF pulse width at 1 Hz.
2. Increase the power level in steps of 0.5 kW and wait till occasional spikes in reflected power disappear.
3. If the reflected power increases to more than 20% or vacuum level degrades to 5×10^{-6} torr, decrease the power level by 0.5 kW and wait for few minutes. Repeat Step 2 till the desired power level is reached.
4. Increase the pulse width and repeat the complete procedure starting from Step 1.
5. If coupler temperature increases beyond 30 deg. C, decrease the power level to safer value.

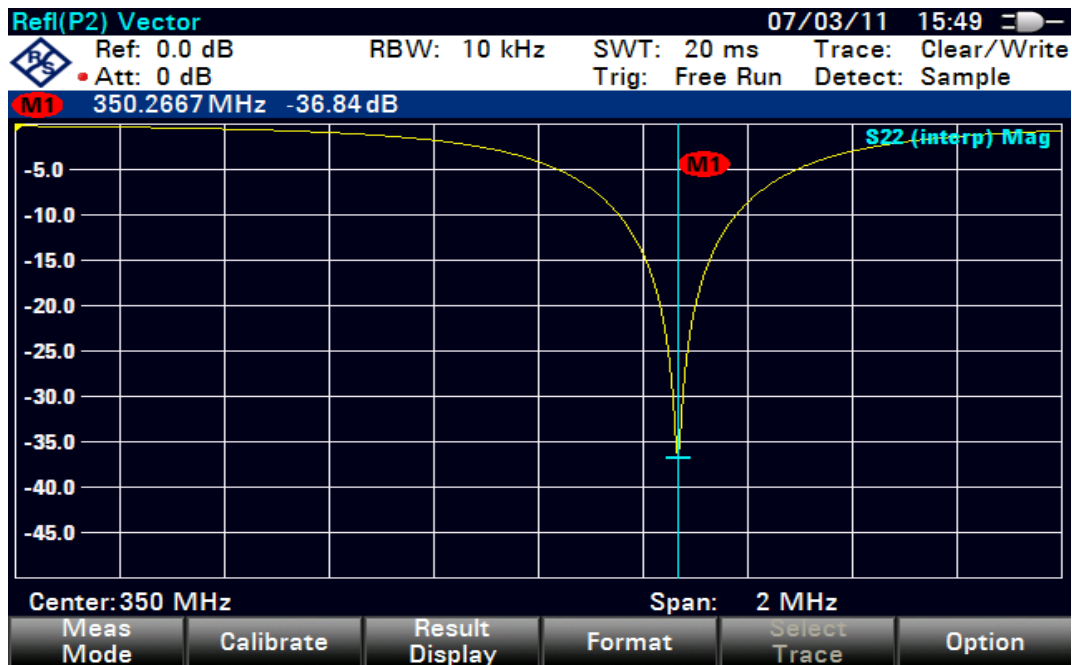


Fig. 5.15 Return loss measurements on coupler connected to the cavity.

In order to test the window-coupler assembly at high powers the input side of coupler port is connected to 50 kW Tetrode based amplifier through a 6 15/8" to 15/8" adapter. The complete system is tested by applying low CW power level of few watts. Return loss of better than -30 dB shows that impedance matching is good after the whole RF system is assembled. However, considerable power reflection is observed as the power level approaches approximately 5 Watts. Deterioration of cavity vacuum is also observed with increase in reflected power. The output probe signal from the cavity is also fed to a CRO and Low Level RF Controller for diagnostics and control purpose. The increase in reflected power at low input power of 5 W is attributed to multipacting in test cavity. After few weeks of conditioning (for approx. 5-6 Hrs every week), the cavity could be conditioned to 100 W CW. Several multipacting barriers were observed up-to 100 W. However, cavity power could be raised smoothly after that. As the cavity temperature went up to 40 deg. C with CW power of 100 watts, the operation mode was shifted to pulsed mode. In pulsed mode, cavity could be conditioned up to 5 kW with varying pulse lengths from 50 microseconds to 1 ms and pulse rates of 1 Hz to 10 Hz. The cavity test system is shown in Fig. 5.16 and 5.17. The set-up shown in Fig. 5.16 is used up to 3.5 kW. The diagnostic elements like vacuum gauge, RTD (Resistance Temperature detector) display etc. can be seen in Fig. 5.17 which is used for high power testing up to 50 kW with 1% duty cycle.

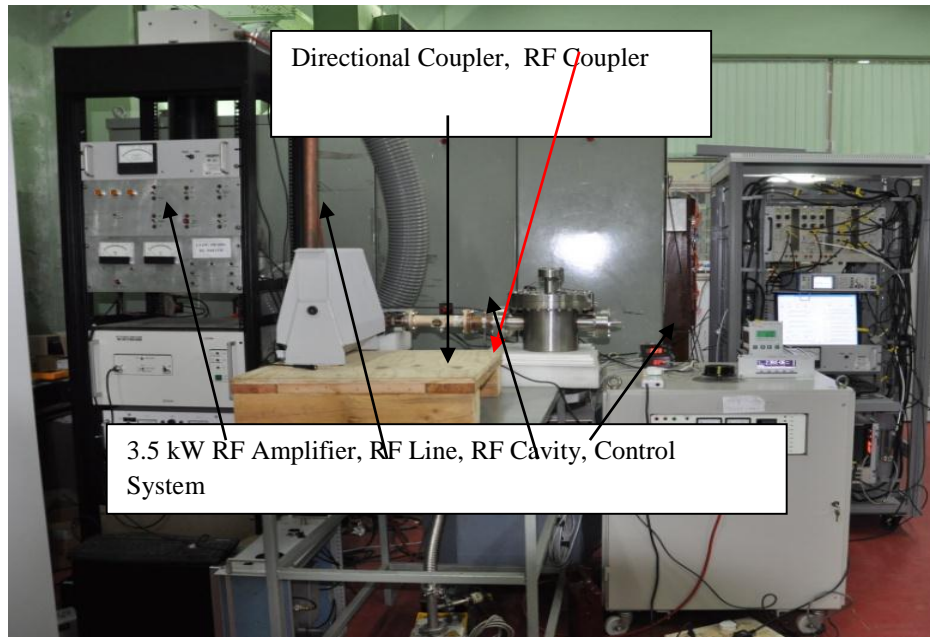


Fig. 5.16 RF Coupler and window assembly being tested up to 3.5 kW power.

The coupler shown in Fig. 5.6 is also tested in standing wave (SW) mode. For testing in SW mode, the loop is rotated in such a way so that power coupling to the cavity is minimum and hence most of the power is reflected. The reflected power test is useful in conditioning the coupler as it creates higher fields at lower incoming RF power. The power was raised to 50 kW at 350 MHz in steps so that cavity vacuum didn't deteriorate beyond 5×10^{-6} torr from the existing vacuum of about 1×10^{-6} torr. The temperature sensors shown in Fig. 5.17 are monitored during conditioning for any abnormal rise and power is decreased if coupler temperature increases to 30 deg. C. The vacuum gauge signal as shown in Fig. 5.17 is also monitored during the conditioning process.

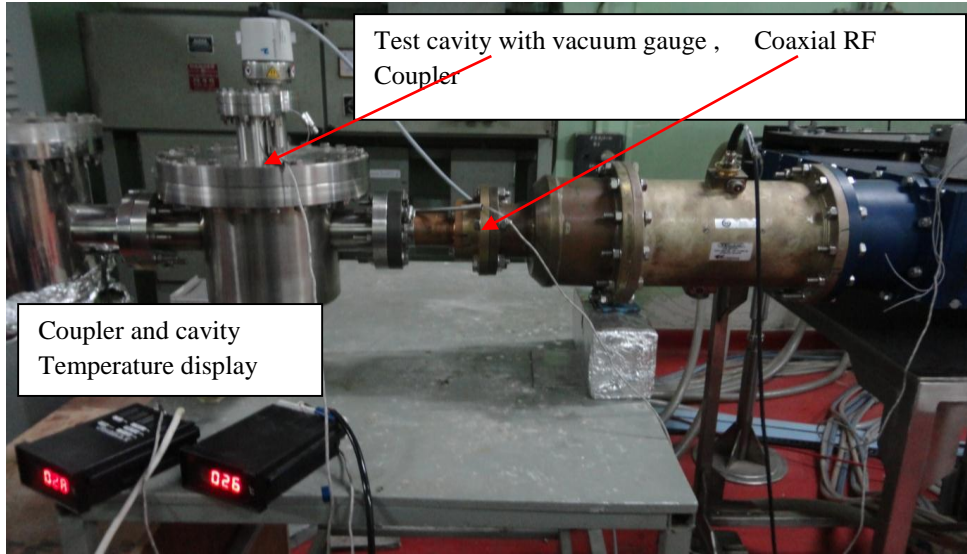


Fig. 5.17 RF conditioning of couplers at 50 kW peak power at 1% duty cycle

During this testing, the pulse width was kept at 1 ms with a repetition rate of 1 Hz. No spark or vacuum degradation beyond 3×10^{-6} torr was noticed during this process. At certain power levels, more vacuum deterioration was noticed as compared to other but vacuum recovered in less than few minutes to original value at such power levels. These levels may correspond to surface degassing, discharges or coupler multipacting levels. As the coupler was fully decoupled, the loop provided a short i.e. reflection coefficient ' $\Gamma = -1$ ' for the electric fields. The window starts at about 55 mm from the shorted end which is about 0.065 of wavelength at 350 MHz.

Though, some of the coupler parts (quarter wavelength away from the short) are tested for field levels equivalent to four times the incoming power i.e. $P_{TW} \sim 4 P_{SW}$, the maximum field level inside the vacuum part of the coupler in SW corresponds to 63% of incoming power. Hence, the coupler could be conditioned to equivalent traveling power of 31.5 kW. This is a useful way of conditioning the coupler as in SW mode, the test cavity is completely decoupled.

A RFQ cavity has been designed and developed at BARC for proton accelerator [104]. After conditioning the coupler in SW mode on test cavity, it was mounted on the RFQ cavity. The coupling was adjusted to ‘critical coupling’ and a return loss of better than -30 dB was measured with VNA. The base vacuum in the RFQ cavity was better than 8×10^{-7} torr during this conditioning process. In the beginning of RFQ conditioning, more than 50% reflection was observed with 1 ms, 1 Hz repetition rate at 349.27 MHz. After decreasing the pulse duration to 100 micro seconds, the power could be raised to 10 kW in about 10 hours of conditioning. The power level was slowly raised in steps of 0.5 kW. A constant power level was maintained for about half an hour at every step so that occasional spikes in the reflection could completely vanish. By following this conditioning procedure, the power could be smoothly raised to 20 kW. From 10 to 20 kW, the power could be raised in less than an hour. This suggests that there were no strong multipacting levels in this coupler-cavity operation range. Prolonged multipacting behavior was observed above 20 kW and required several days for conditioning. The coupler parts and window are not coated with TiN presently and it may be the reason of slow conditioning. The proton beam was extracted from the RFQ cavity at peak power level of 15 kW, 0.5% duty cycle. The coupler was further conditioned to 58 kW at 0.3% duty cycle and is being used for H_2^+ experiments [105]. Fig. 5.18 shows a view of RFQ cavity being powered by RF coupler and incoming RF line. Vacuum system (SS pipes) and bending magnet (in blue color) are also visible.

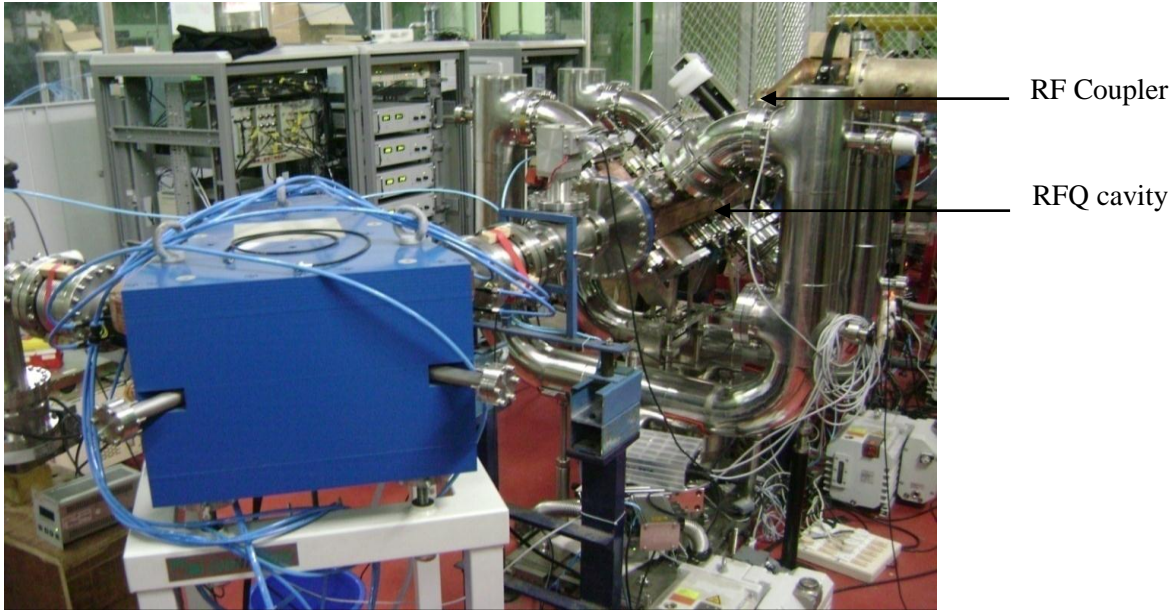


Fig. 5.18 RF Coupler connected to the RFQ cavity for beam experiments.

5.6 SUMMARY

Two high power coaxial couplers with novel window designs have been developed. The un-cooled coupler with under-cut type of window design was integrated to the incoming coaxial line by a coaxial transition. The coaxial cavity was analyzed with CST MWS and fabricated with stainless steel material to verify the electromagnetic design. The cavity frequency error with respect to the simulation results and measurements were found to be less than 0.65%. Also, sufficient tuning range could be obtained with tuners. A close agreement is found between simulated and measured values of resonance frequency. The coupler assembly with under-cut type window is tested for 50 kW at 350 MHz on a test cavity. It is also used to feed up to 58 kW at 350 MHz peak power to a RFQ cavity for conditioning and beam experiments. The water cooled coaxial coupler design is based upon two alumina disc windows and shorted stub loading. The coupler is cooled with water at 2 m/s and designed to dissipate the RF loss of about 1 kW on its surface.

6. CONCLUSIONS AND FUTURE DIRECTIONS

6.1 CONCLUSION

Concept of rotatable iris couplers is proposed and studied in detail. Analytical expressions are also derived for the proposed rotatable coupler. An S band cavity along with a rotatable coupler is designed and fabricated. A close agreement is observed between simulated, analytically calculated and measured coupling values at different iris angles. The problem of low coupling values with rectangular rotatable iris has been studied and solutions based upon iris with lower attenuation coefficient are proposed to obtain required coupling range. Coupling coefficient, RF losses in iris cylinder, EM field enhancements and shift in cavity resonance were studied in detail. These studies indicate that rotatable iris couplers can provide an alternative for tunable coupling which is superior to conventional post fabrication iris machining.

A tuning approach based upon cylindrical tuners is proposed and studied in detail on a straight ridge waveguide coupler and shown to be useful in relaxing the strict dimensional tolerance requirements on ridge waveguide couplers. It is also demonstrated that same tuners can be used for coupling coefficient adjustments. This study also shows that a coupled cavity system is more tolerant to coupler fabrication errors. Cylindrical tuners will provide an effective way to relax the manufacturing tolerances by an order of magnitude and provide coupling coefficient adjustments as well.

The tapered ridge transition is compared with the straight ridge transition for power couplers of accelerator cavities. The EM analysis results for the return loss and the frequency variation are

reported for tapered coupler and compared with the straight ridge coupler. The insertion losses, sensitivity of transmission phase shift with dimensions and frequency, return loss bandwidth, local field enhancements and multipacting comparison are also reported. The tapered coupler has several desirable characteristics like lower RF losses, higher return loss bandwidth, lower variation in phase and lower fields in the central region. The reported studies will help the RF power coupler designers in choosing the desired ridge waveguide based coupling structures for accelerator cavities.

Two ridge waveguide transitions are fabricated and RF measurements are carried out by connecting them back to back. These transitions are also simulated for EM field distributions and return loss characteristics for back to back connection. It is shown by simulations and measurements that tuners are effective in taking care of dimensional errors during manufacturing. The proposed characterization procedure using simulations and measurements will be useful in conditioning these coupler transitions at high power by connecting them back to back. In such scenario, the other output can be terminated in a waveguide matched load, which is available in standard sizes.

Two high power coaxial couplers with novel windows are designed and developed. The un-cooled coupler with under-cut type window design is integrated to the incoming coaxial line by a coaxial transition. A test cavity is also developed for testing and conditioning of these couplers. The coupler assembly is tested for 50 kW at 350 MHz RF Power with 0.1 % duty cycle in standing wave (SW) on a test cavity. It is also used to feed up to 58 kW at 350 MHz peak power to a RFQ cavity for conditioning and particle acceleration. The water cooled coaxial coupler design is based upon two alumina disc windows and shorted stub loading. This coupler has been tested for any vacuum leaks and is being conditioned for higher powers.

6.2 FUTURE DIRECTIONS

The rotatable couplers can be useful for applications in high power accelerator cavities like DTL. Rotatable couplers can be implemented in room temperature applications for offline tuning of coupling. However, it may be difficult to implement rotatable coupling under dynamic conditions because rotatable vacuum and RF seals will make their design complex. It will be useful to develop a coupling algorithm to estimate their depths. An equivalent circuit analysis will also be useful in providing a better understanding of coupler's tunability for various load conditions.

In future, the high power tests on straight ridge couplers along with tuners will provide useful data on their multipacting behavior and tunability aspects in dynamic conditions. It will be interesting to fabricate tapered ridge couplers and compare their high power behavior with straight ridge couplers.

The high power CW conditioning results of coaxial couplers will be important in establishing their reliability. The multipacting and thermal behavior of the RF window in coaxial couplers is crucial and needs to be studied in detail on a dedicated test bench. It will be useful to simulate and correlate the multipacting barriers with measurements.

REFERENCES

- [1] L.M. Young, D. E. Rees, L. J. Rybarcyk and K. A. Cummings, “High power RF conditioning of the LEDA RFQ,” in *Proceedings of the Particle Accelerator Conference*, 1999, NewYork, USA, pp. 881-883.
- [2] Isidoro E. Campisi, “Status of SNS”, presented at 12th SRF workshop, Cornell, July 2005.
- [3] Yong-Sub Cho et al., “The KOMAC Accelerator facility”, in *Proceedings of IPAC*, 2013, pp. 2052-2054.
- [4] D.Barni et al., “Status of the high current proton accelerator for the Trasco program”, *Proceedings of EPAC 2012*, pp. 251-253.
- [5] P-Y. Beauvais, “Recent evolutions in the design of the French high Intensity proton injector (IPHI)”, in *Proceedings of EPAC 2004*, Lucerne, Switzerland.
- [6] Stephen D. Holmes, “Project X: a multi-MW proton source at Fermilab”, in *Proceedings of IPAC 2010*, Japan, pp. 1299-1293.
- [7] L. Arnaudon et al., Editors F. Gerigk, M. Vretenar, “Linac4 Technical Design Report”, CARE-Note-2006-022-HIPPI, 2006.
- [8] P. Singh et al., “Accelerator development in India for ADS program”, *Pramana journal of physics* , vol. 68, p. 331, 2007.
- [9] D. S. Peggs, “The European Spallation Source”, in *Proceedings of PAC 2011*, New York, USA, pp. 2549-2551.
- [10] J. Wei et al. , “China spallation neutron source design”, in *Proceedings of APAC*, Indore, India, pp. 310-314.

- [11] J. Gao, “Analytical formula for the coupling coefficient β of a cavity-waveguide coupled system”, *Nuclear instruments and methods*, vol. A 309, pp. 5-10, 1991.
- [12] J. Gao, “Analytical determination of the coupling coefficient of waveguide cavity coupling”, *Nuclear instruments and methods*, vol. A 481, pp. 36-42, 1991.
- [13] Davide Alesini, “Power Coupling”, in *CERN Accelerator school*, Elbeltoft, Denmark, 2010.
- [14] Hasan Padamsee, *RF superconductivity for Accelerators*, 2nd ed. Wiley-VCHD, 2008.
- [15] D.M Pozar, *Microwave Engineering*, 3rd. ed. John Wiley, 2003, p. 292.
- [16] Han-Sung Kim, Hyeok-Jung Kwon and Yong-Sub Cho, Yong-Seok Hwang “RF Power Coupling for the PEPF Drift Tube”, *Journal of the Korean Physical Society*, vol. 48, no. 4 , pp. 732-735, 2006.
- [17] Y. Kang, S.Kim, M. Doleans, I.E. Campisi, M. Stirbet, P.Kneisel, G. Ciovati, G.Wu, P.Yla-Oijala , “ Electromagnetic simulations and properties of the fundamental power couplers for the SNS superconducting cavities”, in *Proceedings of Particle Accelerator Conference*, 2001, pp. 1122-1124.
- [18] Hiroyasu Ego, “RF input coupler with a coupling tuner for an RF acceleration cavity”, *Nuclear Instruments and Methods in Physics Research*, vol. A 564, pp. 74–80, 2006.
- [19] Haipeng Wang, “Analytical design of a waveguide iris/stub tuning coupler to an overcoupled superconducting cavity”, in *Proceedings of the Particle Accelerator Conference*, 2003, pp. 1101-14.
- [20] Mark S. Champion , “RF input couplers and windows: Performances, limitations, and recent developments”, in *Proceedings of workshop on RF Superconductivity*, 1995, Gif-sur-Yvette, France, pp. 195-221.

- [21] S. Maebara, M. Ichikawa, A. Palmieri, “Coupling factor evaluation of the RF input coupler”, in *Proceedings of IPAC*, 2012, New Orleans, Louisiana, USA.
- [22] Dae-Il Kim et al., “RF Power Coupler for the 100-MeV Drift Tube Linac”, *Journal of the Korean Physical Society*, vol. 54, no. 5, pp. 2005-2008, 2008.
- [23] T. Garvey, W-D Moller, “The RF power coupler development programme at LAL- Orsay and DESY- Hamburg for TESLA and European X-FEL ”, LAL/RT 05-02, June 2005.
- [24] E. Fagotti et al., “High power tests of TRASCO RFQ couplers”, *Proceedings of LINAC 2012*, Tel-Aviv, Israel, pp. 681-683.
- [25] Y. Kang, M. Crofford, T. Hardek, S. Kim, J. Mammoser, R. Peglow, C. Phibbs, A. Vassioutchenko, “High Power RF Processing of Couplers/Windows and Cavities for SNS Linac”, in *6th CW and High Average Power RF Workshop ALBA*, Barcelona, Spain, May 4-7, 2010.
- [26] S. Belomestnykh, “Review of high power CW couplers for superconducting cavities”, presented at the Workshop on High-Power Couplers for Superconducting Accelerators, Jefferson Lab, 2002.
- [27] Isidoro E. Campisi, “ State of the art power couplers for superconducting RF cavities”, in *Proceedings of the European Particle Accelerator Conference 2002*, Paris, France, pp. 144-148, 2002.
- [28] C. Arnaudon, et al., “Status Report on Superconducting Nb Cavities for LEP,” in *Proceedings of 4th Workshop on RF Superconductivity*, August 1989, KEK, Tsukuba, Japan, vol. 1, pp. 19-35.

- [29] H.P. Kindermann et al., “Status of RF Power Couplers for Superconducting Cavities at CERN,” in *Proceedings of the 5th European Particle Accelerator Conference*, 1996, Sitges, Barcelona, Spain, pp. 2091-2093.
- [30] H.P. Kindermann, M. Stirbet, “RF Power Tests of LEP2 Main Couplers on a Single Cell Superconducting Cavity,” in *Proceedings of the 8th Workshop on RF Superconductivity*, October 1997, Abano Terme (Padova), Italy, vol. 3, pp. 732-739.
- [31] H.P. Kindermann, M. Stirbet, “The Variable Power Coupler for the LHC Superconducting Cavity,” in *Proceedings of the 9th Workshop on RF Superconductivity*, 1999, Santa Fe, NM, pp. 566-569.
- [32] M. Neubauer, K. Fant, J. Hodgson, J. Judkins, H. Schwarz, “High-power RF window and coupler development for the PEP B-II factory”, SLAC-PUB-95-6897 - LBL-37250, 1995.
- [33] B. Dwersteg, Qiao Yufang, “High Power Input Coupler Development at DESY,” in *Proceedings of the 4th Workshop on RF Superconductivity*, August 1989, KEK, Tsukuba, Japan, vol. 2, pp. 605- 614.
- [34] B. Dwersteg, “High Power Couplers,” in *Proceedings of the 4th Workshop on RF Superconductivity*, August 1989, KEK, Tsukuba, Japan, vol. 1, pp. 351- 376.
- [35] D. Metzger, et al., “Tests Results and Design Considerations for a 500 MHz, 500 kW Vacuum Window for CESR-B,” in *Proceedings of the Particle Accelerator Conference*, 1993, Washington, USA, p.p 1399-1401.
- [36] H. Padamsee, et al., “Beam Test of a Superconducting Cavity for the CESR Luminosity Upgrade,” in *Proceedings of the Particle Accelerator Conference*, 1995, Dallas, USA, pp.1515-1517.

- [37] S. Belomestnykh and H. Padamsee, “Performance of the CESR Superconducting RF System and Future Plans,” in *Proceedings of the 10th Workshop on RF Superconductivity*, Tsukuba, Japan, September 2001.
- [38] S. Noguchi, et al., “Couplers – Experience at KEK,” in *Proceedings of the 4th Workshop on RF Superconductivity*, August 1989, KEK, Tsukuba, Japan, vol. 1, pp. 397-412.
- [39] S. Mitsunobu, et al., “High Power Input Coupler for KEKB SC Cavity,” in *Proceedings of the 9th Workshop on RF Superconductivity*, Santa Fe, NM, November 1999.
- [40] Y. Kijima et al., “Input Coupler of Superconducting Cavity for KEKB,” in *Proceedings of the 7th European Particle Accelerator Conference*, 2000, Vienna, Austria, pp. 2040-2042.
- [41] E. N. Schmierer et al., “Results of the APT RF Power Coupler Development for Superconducting Linacs,” in *Proceedings of the 10th Workshop on RF Superconductivity*, Tsukuba, Japan, September 2001.
- [42] V. Nguyen et al., “Development of a 50 kW CW L-Band Rectangular Window for Jefferson Lab FEL Cryomodule,” in *Proceedings of the Particle Accelerator Conference*, 1999, New York, USA, vol. 2, pp. 1459-1461.
- [43] V. Veshcherevich, S. Belomestnykh, P. Quigley, J. Reilly, J. Sears, “High power tests of first input couplers for Cornell ERL injector cavities”, in *Proceedings of the Particle Accelerator Conference*, 2007, New Mexico, USA, pp. 2355-2357.
- [44] Wencan Xu, “Design, simulations, and conditioning of 500 kW fundamental power couplers for a superconducting RF gun”, *Physical review special topics - accelerators and beams*, vol. 15, 2012.

- [45] L.M. Young, D. E. Rees, L. J. Rybarczyk and K. A. Cummings, “High power RF conditioning of the LEDA RFQ,” in *Proceedings of the Particle Accelerator Conference*, 1999, New York, USA, pp. 881-883.
- [46] J. Jang, Y. Cho, B. Choi, J. Kim, K. Kim, J. Park, “ The Korean Proton Engineering Frontier Project” in *Proceedings of the 42nd ICFA Advanced beam dynamics workshop on high intensity, high brightness hadron beams*, ORNL-SNS, August 2008.
- [47] Dae-II Kim, Hyeok- Jung K Won, Han-Sung Kim and Yong-Sub Cho, “RF Power Coupler for the 100-MeV Drift Tube Linac”, *Journal of the Korean Physical Society*, vol. 54, no. 5, pp. 2005- 2008, 2009.
- [48] P-Y. Beauvais, “Recent evolutions in the design of the French High Intensity Proton Injector (IPHI),” in *Proceedings of the European Particle Accelerator Conference* ,2004, pp. 1273-1275.
- [49] Ref. [7], pp. 12-13.
- [50] Ref. [7], pp. 24-25.
- [51] A. Palmieri, M. Comunian, J. Esposito, A. Pisent, “ Study and design for TRASCO RFQ high power coupler, ” in *Proceedings of the LINAC*, 2002, pp. 722-724.
- [52] Yoon Kang, Alexandre Vassioutchenko,Robert Peglow,Thomas Hardek, “Design, “Conditioning, and Operation of Upgrade RFQ Coupling System”, in *Fifth CW and High Average Power RF Workshop*, March 25-28, 2008.
- [53] Sung-Woo Lee, Yoon W. Kang, Ki R. Shin, A. Vassioutchenko, “ Computer simulations of waveguide window and coupler iris for precision matching”, in *Proceedings of PAC*, 2011, New York, pp. 832-834.

- [54] Y. Kang, M. Crofford, T. Hardek, S. Kim, J. Mammosser, R. Peglow, C. Phibbs, A. Vassioutchenko, "High Power RF Processing of Couplers/Windows and Cavities for SNS Linac", in *Sixth CW and High Average Power RF Workshop*, Spain, Italy, May 4-7, 2008.
- [55] Computer Simulation Technologies (CST) Microwave Studio, CST AG, Darmstadt, Germany, website: www.cst.com.
- [56] Norman M. Kroll, "Computer determination of the External Q and resonant frequency of waveguide loaded cavities", SLAC-PUB-5171, January 1990.
- [57] P. Balleyguier, "A straightforward method for cavity external Q computation", *Particle Accelerators*, 1997, vol. 57 (1997), pp. 113-127.
- [58] S.V. LS Rao, Rajesh Kumar et al., "Preliminary studies on External Q calculations on RFQ cavity", Internal report, LEHIPA Project, 2006, BARC.
- [59] Ref. [15], p. 299.
- [60] Rajesh Kumar, IADD internal report on Fermilab deputation, 2012.
- [61] A.J. Hatch, H.B. Williams, "Multipacting modes of high frequency breakdown", *Phys. Rev.*, vol. 112, 1958.
- [62] E. Somersalo, P. Yl'a-Oijala, D. Proch, "Analysis of multipacting in coaxial lines", in *Proceedings of PAC*, 1995, Dallas, USA, pp. 1500–1503.
- [63] R. L. Geng, H. Padamsee, V. Shemelin, "Multipacting in rectangular waveguides," in *Proceedings of PAC*, 2001, Chicago, USA, pp. 1228–1230.

- [64] Daniel González-Iglesias, Pablo Soto, Sergio Anza, Benito Gimeno, Vicente E. Boria, Carlos Vicente, and Jordi Gil, “ Multipactor susceptibility charts for ridge and multiridge waveguides”, *IEEE Transactions on electron devices*, vol. 50 , pp. 3601-3607, 2012.
- [65] Y.W Kang, R.L Kustom, “Variable input coupler design for storage ring cavities”, Light Source Notes-LS-248 Aug. 18, 1995.
- [66] Rajesh Kumar, S.V.L.S Rao, P.Singh, “RF Design of high Power Couplers for ADS”, in Proceedings of InPac 2006, Mumbai, India.
- [67] J.M. Han, H.H Lee, Y.S.Cho, B.H. Choi, “RF Coupler Design for the KTF RFQ Linac”, in *Proceedings of PAC*, 2001,Chicago,USA, pp. 1210-1212.
- [68] Han-Sung Kim, Hayeok-Jung Kwon and Yong-Sub Cho, “RF Power Coupling for the PEPF Drift Tube Linac”, *Korean Phys. Soc.*, 2006, vol. 48, no. 4, pp. 732-736.
- [69] P.Balleyguier, M.Painchault, “Design of RF Power input ports for IPHI RFQ”, in *Proceedings of EPAC* , 2002, Paris, France, pp. 2124-2126.
- [70] A. Bethe, “Theory of diffraction by small holes,” *Physical Review*, vol. 66, pp.163–182, 1944.
- [71] C.J. Bouwkamp,“On Bethe’s Theory of diffraction by small holes,” *Phillips Rep.*5, 401,1950.
- [72] S.B. Cohn, “Determination of aperture parameters by electrolytic- tank measurements”, in *Proceedings of the I.R.E*, vol. 66, pp. 1416–1421, 1951.

- [73] P. Balleyguier, "External Q studies for APT cavity couplers," in *Proc. Linear Accelerator Conf. LINAC*, 1998, Chicago, USA, pp. 133-135.
- [74] O. Kamigaito, "Circuit model representation of external-Q calculation," *Phys. Rev. ST Accel. beams*, vol. 9, 2006.
- [75] Sembiam.R.Rengarajan, "Analysis of a centered-inclined waveguide slot coupler," *IEEE Trans. Microwave Theory Tech.*, vol. 37, no. 5, pp. 884-889, 1989.
- [76] Sembiam.R.Rengarajan, "Characteristics of a longitudinal/ transverse coupling slot in crossed rectangular waveguides," *IEEE Trans. Microwave Theory Tech.*, vol. 37, no. 8, pp. 1171-1177, 1989.
- [77] M. V. Nesterenko, V. A. Katrich, Y. M. Penkin, and S. L. Berdnik, "Analytical methods in theory of slot-hole coupling of electrodynamic volumes," *Progress In Electromagnetics Research-PIER*, vol. 70, pp. 79-174, 2007.
- [78] Luciano Accatino, Giorgio Bertin and Mauro Mongiardo, "A four pole dual mode elliptic filter realized in circular cavity," *IEEE Trans. Microwave Theory Tech.*, vol. 44, no. 12, pp. 2680-2687, 1996.
- [79] Zulfigar Ali Khan, Charles F. Bunting, Manohar D. Deshpande, "Shielding effectiveness of metallic enclosures at oblique and arbitrary polarizations," *IEEE Trans. Electromagnetic compatibility*, Vol. 47 No. 1 (2005), p. 112-122, February 2005.
- [80] Saito Y, Filipovic D.S, "Analysis and design of monolithic rectangular coaxial lines for minimum coupling," *IEEE Trans. Microwave Theory Tech.*, Vol. 55, No. 12, pp. 2521-2530, 2007.
- [81] R.E Collins, *Field Theory of guided waves*, 2nd ed. IEEE Press, 1991.

- [82] R.K Mongia and R.K Arora, "Equivalent circuit parameters of an aperture coupled open resonator cavity," *IEEE Trans. Microwave Theory Tech.*, vol. 41, no. 8, p. 1245-1250, 1993.
- [83] Rajat Roy and O. Shanker, "Calculation of inter cavity coupling coefficient for side coupled standing wave linear accelerator ," *IEEE Trans. Microwave Theory Tech.*, vol. 41, no. 6, pp. 1233-1235, 1993.
- [84] Noel A. McDONALD, "Polynomial approximations for the electric polarizabilities of some small apertures," *IEEE Trans. Microwave Theory Tech.*, vol. 33, no. 11, pp. 1146-1149, 1993.
- [85] Noel A. McDONALD, " Simple approximations for the longitudinal magnetic polarizabilities of some small apertures," *IEEE Trans. Microwave Theory Tech.*, vol. 36, no. 7, pp. 1141-1144, 1988.
- [86] Noel A. McDONALD, "Polynomial approximations for the transverse magnetic polarizabilities of some small apertures," *IEEE Trans. Microwave Theory Tech.*, vol. 35, no. 1, pp. 20-23, 1987.
- [87] Noel A. McDONALD, "Electric and magnetic coupling through small apertures in shield walls of any thickness," *IEEE Trans. Microwave Theory Tech.*, vol. 20, pp. 689-685, 1972.
- [88] Ref. [15], p. 110.
- [89] Girish Kumar and K.P Ray, "*Broadband Microstrip Antennas*", 3rd. ed. Artech House, 2003, pp. 223-225.
- [90] M.S Ansari, S.V.G Ravindranath, M.S Bhatia, B. Singh, C.P Navathe, "Electromagnetic coupling through apertures and shielding effectiveness of a metallic enclosure housing

- electro-optic pockels cell in a high power laser system”, *International Journal of Applied Electromagnetics and Mechanics*, vol. 42, no. 2, pp. 191-199, 2013.
- [91] Mark S. Champion, in *1995 workshop on RF Superconductivity*, Gif-sur-Yvette, France, pp. 195-221.
 - [92] Mircea Stirbet, in *High Power Couplers workshop*, Oct 30-Nov 2002, Jefferson Lab, New port News, Virginia, USA.
 - [93] Sami Tantawi, Chris Nantista and Valery Dolgashev, in *High Power Couplers workshop*, Oct 30-Nov 2002, Jefferson Lab, New port News, Virginia.
 - [94] T. Garve, LAL/RT 06-03 April 2006.
 - [95] R.Valdiviez, P. Roybal,B. Clark, F. Martinez, D. Caillas, G.Gonzales, J.Tafoya, “The Mechanical design and fabrication of a ridge-loaded waveguide for an RFQ”, in *Proceedings of LINAC*, 1998, pp. 597-599.
 - [96] M.S.de Jong, F.P. Adams, R.J Burton, R.M Hutcheon, T. Tran-Ngoc, “Design of a Tuner and Adjustable RF coupler for a CW 2856 MHz RF cavity”, in *Proceedings of PAC*, 1993, pp. 830-831.
 - [97] Olivier Piquet, Michel Desmons, Alain France, DAPNIA/SACM/IPHI, 7 February 2005.
 - [98] H. Safa, “Multiple coupling and beam loading of a RF cavity”, in *Proceedings of LINAC*, 1998, Chicago, USA.
 - [99] COMSOL AB, Stockholm, Sweden, website: www.comsol.se
 - [100] P. Jain et al., “Thermo-structural analysis of 400 keV deuteron RFQ components”, in *Proceedings of APAC*, 2007, Indore.
 - [101] Thomas P Wangler, RF Linear Accelerators, Wiley-vch verlag, 2nd ed., 2008, p. 145.

- [102] J. Gioia et al., “A room temperature test bed for evaluating 700 MHz RF windows and power couplers for super conducting portion of APT Accelerator”, in *Proceedings of PAC*, 1999, New York, USA.
- [103] H. Buttig et al., “Tests of air cooled 1.3 GHz Waveguide windows using a RF Coupler Test Bench based on a Resonant ring”, in *Proceedings of SRF*, 2007, Peking univ. Beijing, China.
- [104] S.V.L.S Rao, P. Singh, “Design studies of a high-current radiofrequency quadrupole for accelerator-driven systems programme”, *Pramana Journal of physics*, vol. 74, no. 2, pp. 247-259, 2010.
- [105] S.V.L.S Rao et al., “Design, development and acceleration trials of radio-frequency quadrupole”, *Review of Scientific instruments*, vol. 85, no. 4, 2014.

